Fluoride-ion batteries with liquid electrolytes



Giulia Galatolo

Mansfield College
University of Oxford

A thesis submitted for the degree of

Doctor of Philosophy in Materials

Trinity 2023

Abstract

A crucial avenue to curb greenhouse emissions is electrifying transportation. To do so, novel battery technologies are needed. These should have higher energy densities than what is achievable with current technologies, while also avoiding the critical minerals found in lithium-ion batteries (LIBs). Among the possible alternatives, fluoride-ion batteries (FIBs) are a promising chemistry to satisfy both requirements. Within the different types of FIBs, conversion-type FIBs with liquid electrolytes show the most potential in terms both of theoretical energy density and cost.

However, liquid electrolyte FIBs have not achieved satisfactory performance yet due to several outstanding issues. First, no suitable liquid electrolyte has been found, due to the many difficulties in designing one. The main one being that F-ions are highly reactive, easily causing chemical degradation and the formation of the corrosive HF. Additionally, fluoride salts are insoluble in the organic aprotic solvents commonly used in batteries. Lastly, the absence of a suitable counter-reference electrode and other inactive components, has prevented the establishment of an accurate and reliable testing set-up, such as coin or pouch cells.

In this work, first I enable the use of coin cells for FIBs by identifying hydrophilic PTFE as a suitable separator, as well as by manufacturing a reliable counter-reference electrode using Pb-PbF_2, with PTFE as a chemically stable binder. The use of coin cells allows for the accurate measurement of the cycling performance of the two novel electrolytes presented subsequently.

The first liquid electrolyte reported exploits a design strategy novel to the FIBs field. The use of a diluent (propionitrile) to reduce the viscosity of a highly concentrated solution (tetramethylammonium fluoride in methanol). The diluted electrolyte achieves a one order of magnitude increase in the diffusion coefficient of F-ions, while retaining the wide electrochemical stability window of the highly concentrated electrolyte. When cycling Pb-PbF_2 symmetric cells the diluted electrolyte also exhibits a substantially higher capacity retention, compared to the highly concentrated electrolyte. The diluted electrolyte and the coin cell set-up achieve the best cycling performance of Pb-PbF_2 and BiF_3 electrodes in the field to date.

The second novel liquid electrolyte employs a different strategy and aims to enable F-ion solvation while retaining chemical stability. By using 0.3 m TMAF in an imidazolium-based ionic liquid (1,3-dimethyimidazolium bis(trifluoromethanesulfonyl)imide) I report the first chemically stable liquid electrolyte for FIBs. The electrolyte displays a wide electrochemical stability window and good ionic conductivity. It also highlights an important factor in the success of liquid electrolytes for FIBs: the presence of a proton in the solvent which is acidic enough to enable F-ion solvation, while not being so acidic that HF is formed.

Overall, the findings presented in this work not only raise the level of performance of liquid electrolyte FIBs, but also introduce promising novel strategies to make FIBs a competitive technology.

Publication List

1. Galatolo, G., Alshangiti, O., Di Mino, C., Matthews, G., Xiao, A. W., Rees, G., Schart, M., Chart, Y., Pasta, M., *Advancing fluoride-ion batteries with a Pb-PbF_2 counter electrode and a diluted liquid electrolyte*. Under review in ACS Energy Lett.

2. Xiao, A. W. [*], Galatolo, G.[*], Pasta, M., *The case for fluoride-ion batteries*, Joule (2021), 5, 11, 2823-2844.

   [*] These authors contributed equally

3. Alshangiti, O., Galatolo, G., Rees, G., Guo, H., Quirk, J. A., Dawson, J. A., Pasta, M., *Solvent-in-Salt Electrolytes for Fluoride Ion Batteries*, ACS Energy Lett. (2023), 8, 6, 2668-2673.

Acknowledgements

I want to extend my gratitude to my PhD supervisor, Prof. Mauro Pasta, for offering me the opportunity to pursue a PhD within his research group. These four years have been a tremendous learning experience for which I am thankful.

I would like to thank my collaborators, Omar Alshangiti, Dr Camilla Di Mino, Dr Gregory Rees, Dr Guillaume Matthews, Maximilian Schart and Yvonne Chart for their invaluable help and contributions to this work. Additionally, I thank Dr Albert Xiao, who generously devoted his time to train me at the beginning of my PhD journey.

I would also like to thank my friends and colleagues Max, Shobhan, Brigita, Mu and Marco, for their constant support during the challenging times and for the wonderful memories that will stay with me forever. A special thanks to Max for always being there when I needed it most and for being my adventure partner throughout these four years, especially during the long months of lockdown.

I would like to thank my housemates, Angela, Eliana, and Francis, as well as my tennis partner, Viviane, for making my time in Oxford incredibly enjoyable.

Lastly, I want to express my deepest gratitude to my family for their love and support, particularly my parents, Patrizia and Luciano, who have always been there for me and without whom I would not have had such incredible opportunities. And to my partner Andrés who has been by my side for all the highs and lows, supporting me in every possible way. I cannot wait to see what the next chapter holds for us.

Table of Contents

Chapter 1 – Introduction 1

1.1 The Case for Post-Lithium-Ion Technologies 2

1.2 Operating Principle and Advantages of Fluoride-Ion Batteries 6

1.3 How FIBs Compare to LIBs 9

1.4 Critical Research Fronts of Fluoride-Ion Batteries 12

1.5 Inactive Components and Testing Set-up 14

1.6 Electrolytes for FIBs 17

1.6.1 Solid versus liquid electrolytes 19

1.6.2 Solid electrolytes 21

1.6.3 Liquid electrolytes 22

1.7 Summary and Thesis Aim 30

Chapter 2 – Methods 32

2.1 Introduction 33

2.2 Manufacturing Procedures 34

2.2.1 Reduction in particle size 34

2.2.2 Manufacturing process for electrodes with PIB binder 34

2.2.3 Extra details for dry casting of Pb-PbF_2 electrodes 35

2.2.4 Coin cells assembly 35

2.2.5 Drying of commercial tetramethylammonium fluoride 36

2.2.6 Synthesis of tetramethylammonium fluoride 37

2.2.7 Washing procedures for 1,3-dimethylimidazolium bis(trifluoromethanesulfonyl)imide 38

2.3 Materials Characterisation 39

2.3.1 Nuclear magnetic resonance 39

2.3.2 Pulsed field gradient nuclear magnetic resonance 41

2.3.3 Dynamic light scattering 42

2.3.4 Karl Fischer coulometric titration 43

2.3.5 X-ray diffraction 44

2.3.6 Fourier-transform infrared spectroscopy 45

2.3.7 Inductively coupled plasma optical emission spectroscopy 46

2.4 Microscopy Techniques 47

2.4.1 Scanning electron microscopy 47

2.4.2 Plasma focused ion beam 48

2.5 Electrochemical Characterisation 49

2.5.1 Galvanostatic cycling 49

2.5.2 Potentiostatic electrochemical impedance spectroscopy 50

2.5.3 Linear scanning voltammetry 54

2.6 Monte Carlo Simulations 55

Chapter 3 – Inactive Components and Testing Set-Up 57

3.1 Introduction 58

3.2 Results and Discussion 60

3.2.1 Active material selection and processing for counter-reference electrodes 60
3.2.2 Choice of a suitable binder 63
3.2.3 Manufacturing process for Pb-PbF_2 counter-reference electrodes 68
3.2.4 Choice of separator 71
3.2.5 Cycling of Pb-PbF_2 counter-reference electrodes in 2-electrode coin cells 76

3.3 Conclusion and Future Work 78

Chapter 4 – A Diluted Liquid Electrolyte with Improved Cyclability 81

4.1 Introduction 82

4.2 Results and Discussion 84

4.2.1 Selection and synthesis of fluoride salt 84
4.2.2 Selection of solvents 89
4.2.3 Characterization of solvation structure 90
4.2.4 HF formation 95
4.2.5 Characterization of electrolyte properties 96
4.2.6 Cycling of Pb-PbF_2 electrodes in the diluted electrolyte 97
4.2.7 Cycling of BiF_3 vs Pb-PbF_2 in the diluted electrolyte 102
4.2.8 Cycling of CuF_2 vs Pb-PbF_2 in the diluted electrolyte 106

4.3 Conclusion and Future Work 107

Chapter 5 – A Chemically Stable Ionic Liquid-Based Electrolyte 110

5.1 Introduction 111

5.2 Results and Discussion 112

5.2.1 Selection process for the ionic liquid 112
5.2.2 Solvation of F^- in the two ionic liquids 114
5.2.3 Chemical stability of the two electrolytes 117
5.2.4 Transport and electrochemical properties 124
5.2.5 Cycling of 0.3 m TMAF-DMIM TFSI with Pb-PbF_2 electrodes 128
5.2.6 Purification of DMIM TFSI 131

5.3 Conclusion and Future Work 134

Chapter 6 – Conclusion and Future Work 136

6.1 Conclusion 137

6.2 Future Work 139

References 142

Chapter 1

Introduction

Table of Contents

1.1 The Case for Post-Lithium-Ion Technologies 2
1.2 Operating Principle and Advantages of Fluoride-Ion Batteries 6
1.3 How FIBs Compare to LIBs 9
1.4 Critical Research Fronts of Fluoride-Ion Batteries 12
1.5 Inactive Components and Testing Set-up 14
1.6 Electrolytes for FIBs 17
1.6.1 Solid versus liquid electrolytes 19
1.6.2 Solid electrolytes 21
1.6.3 Liquid electrolytes 22
1.7 Summary and Thesis Objectives 30

1.1 The Case for Post-Lithium-Ion Technologies

Human activity is responsible for the ongoing rise in global average temperature, which began in the mid-20th century. By 2012, the average surface temperature had increased by approximately 1°C compared to pre-industrial levels. This temperature increase has resulted in more frequent and intense extreme weather events, such as droughts and floods, as well as contributing to sea level rise and loss of biodiversity.[1]

To avert both a natural and social catastrophe countries have pledged to limit the global temperature increase by mid-century to below 2°C compared to pre-industrial levels (Paris agreement). To meet this goal, a dramatic cut in global greenhouse gas emissions is necessary. Burning of fossil fuels in energy production, transportation, and industry is the primary source of greenhouse gas emissions, making it imperative to transition to more sustainable alternatives.[2]

Electrochemical cells, in particular batteries, can play a crucial role in reducing our dependence on fossil fuels. They are essential for smoothing out the fluctuations in energy output from renewable sources and advancing the shift towards more environmentally friendly transportation.

Lithium-ion batteries (LIBs), firstly developed by Goodenough, Whittingham and Yoshino in the 1970s-1980s and commercialised by SONY in 1991, have already initiated the green transport revolution by enabling the commercialisation of electric vehicles (EVs).

LIBs comprise of two electrodes—cathode and anode—and an ionically conductive electrolyte separating the two. The anode is made of graphite, the electrolyte consists of a Li salt dissolved in a mix of organic solvents, whereas the cathode composition depends on the application. The cathode of many EVs batteries is composed of nickel, cobalt, and manganese (NMC). Among the two electrodes, the cathode has the largest impact on battery cost. This is primarily due to its lower energy density compared to graphite, which necessitates a larger amount of material per unit cell, and the largest cost per atom of Ni, Mn and Co compared to C.[3]

After steadily declining for over seven years, the price of LIBs has instead started to increase and stabilise at around USD 150 per kWh, jeopardizing the affordability of the energy transition (Fig. 1.1).[4] This surge in prices can be attributed to a significant rise in the cost of the key minerals of LIBs, specifically those found in the cathode. Particularly, the lithium price increased more than sevenfold in 2022, whereas the price of cobalt and nickel more than doubled (Fig. 1.1). The surge in prices has been fuelled by a combination of factors, including rising battery demand, increasing pressure on supply chains and concerns around tightening supply.[3]

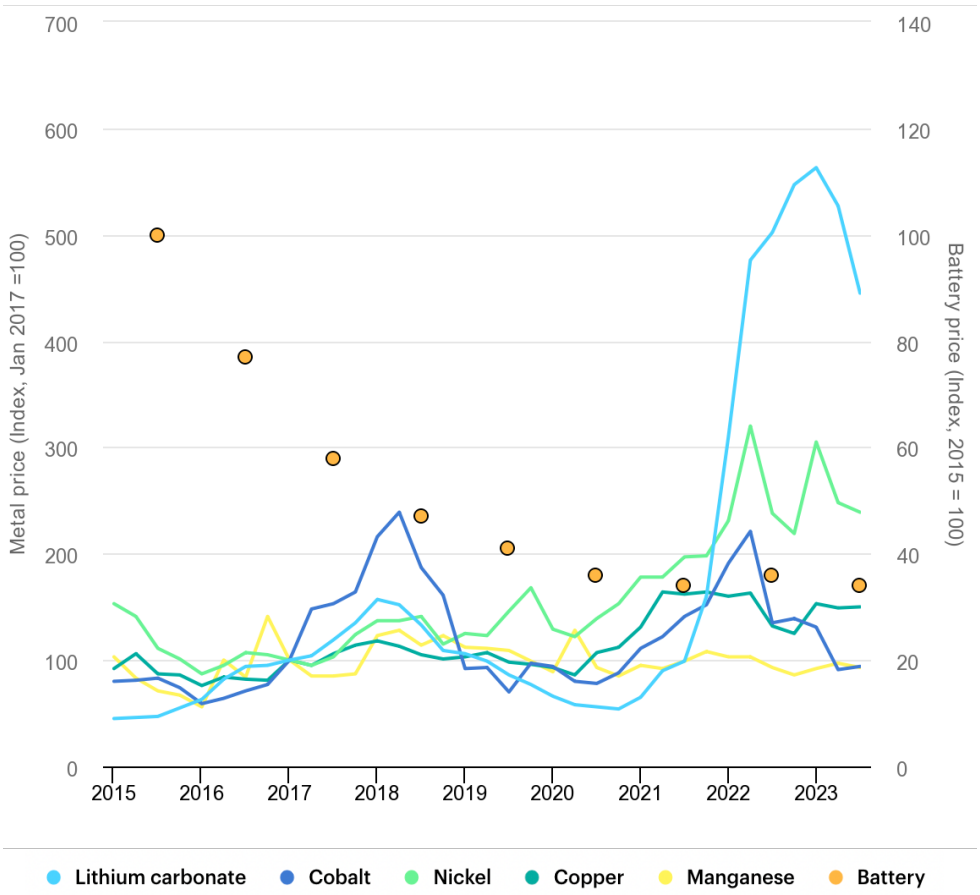


Figure 1.1: Battery price and cost of lithium, cobalt, nickel, and manganese between 2015 and 2023.[4] 2022 saw a surge in the battery cost for the first time, fuelled by a surge in the cost of lithium carbonate and nickel.

To avoid a slowdown in the adoption of EVs due to rising costs, car manufacturers are turning to alternative chemistries. Lithium iron phosphate (LFP) typically has only 65-75% of the energy density of Ni-rich NMC (NMC 811), nonetheless it is becoming increasingly popular, particularly in China, because of its lower cost, its lower risk of catching fire and its longer cycle life. Na-ion cells have about half of the energy density of leading NMC chemistries and therefore cannot be employed alone in high energy density applications. However, the high abundancy and low cost of the minerals make Na-ion an attractive technology for grid-scale storage, for urban EVs, as well as for standard EVs if in conjunction with LIBs. With already more than 30 Na-ion battery manufacturing plants either operational, under construction or

planned in 2023, Na-ion powered electric vehicles are predicted to become available for sale between 2023-2024.[4]

However, these alternative chemistries alone are not sufficient to meet the long-term net-zero greenhouse gas emission objectives. Higher energy density batteries which are not reliant on lithium are required to expedite the electrification of transportation. The cost of LIBs is anticipated to escalate even further, primarily due to the future ban on the sale of new internal combustion engine cars in favour of EVs This will require significantly larger quantities of raw materials, placing additional pressure on the supply chain. Predictions suggest that the demand for lithium, nickel and cobalt required to reach net zero emissions will outstrip supply, most likely fuelling a surge in cost. In particular, the demand for lithium is expected to outstrip supply already from 2028 (Fig. 1.2).[3,5]

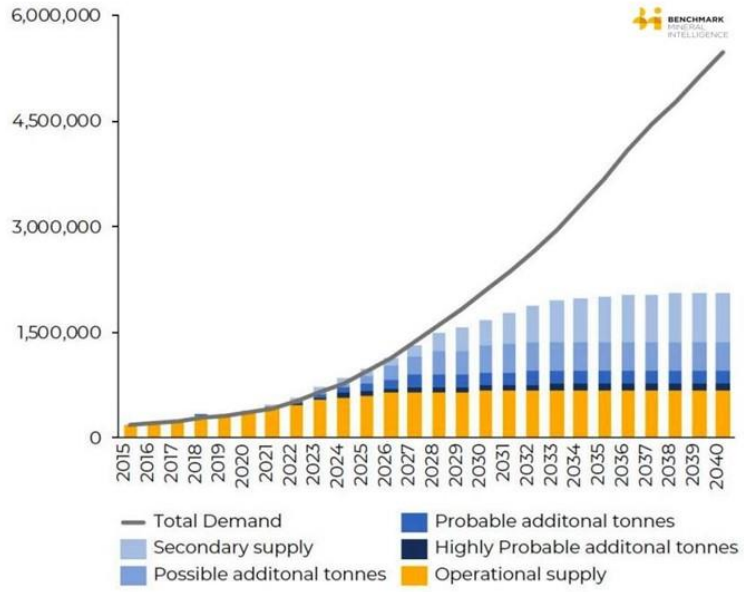


Figure 1.2: Prediction of total Li demand in tonnes until 2040. The demand will outstrip the available supply from 2028.[5]

One strategy to meet the requirements of the energy transition is to develop high energy density battery technologies beyond Li-ion. While sodium and potassium ion batteries are being investigated as low energy density alternatives to LIBs, several other chemistries are

being explored as higher energy density possibilities. Multivalent charge carriers such as Mg^{2+} and Ca^{2+} are one of these chemistries. However, the larger charge density associated with these ions leads to worse transport properties through the electrolyte, and an overall inferior rate capability compared to LIBs.[6]

Anionic batteries are another alternative which have become increasingly popular over the past years. In anionic batteries an anion rather than a cation, as in LIBs, is the main charge carrier. OH^- is the most well-known species, which is found in the nickel-metal hydride or alkaline batteries system. Alternatively, O^{2-}, F^-, Cl^-, Br^-, I^- have all been investigated as the main charge carrier in anionic batteries.[7]

Among anionic batteries, rechargeable fluoride-ion batteries (FIBs), which use F^- as the charge carrier, have been attracting a growing interest since their first demonstration in 2011 by Reddy and Fichtner. The very high electronegativity of fluorine of 4.0 and its light weight could result in high energy densities and voltages.[8] A large interest in FIBs is strongly present in Japan, where most of the field's research is taking place, sponsored by Toyota, Nissan, Panasonic, and Honda, among others. FIBs are showing great potential; however, several challenges have prevented them from reaching satisfactory performance.

1.2 Operating Principle and Advantages of Fluoride-Ion Batteries

Fluoride-ion batteries comprise a positive electrode known as cathode and a negative electrode known as anode. The potential difference between the two spatially separated electrodes causes a spontaneous electrochemical reaction leading to the reduction of the cathode and the oxidation of the anode. The consequence of this reaction is the release of electrons to the external circuit ready to do work. The electrolyte enables charge neutrality by allowing the shuttling of ions between the cathode and the anode. The two electrodes are

stacked on top of each other and separated by an electrically insulating membrane (separator), which prevents short-circuiting while allowing ion transfer. Additionally, the electrode materials are used in powder form, and a polymeric matrix (binder), is used to hold the particles together and in good contact with the current collector. A carbon additive is also included in the electrode mix to improve electronic conductivity. Secondary (i.e., rechargeable) FIBs, as LIBs, can also undergo the inverse process to get recharged once an electrical current is applied to them.

Although some work on primary—non-rechargeable—FIBs was done in the '70s and '80s, the first rechargeable FIB was only demonstrated in 2011 by Fichtner and Reddy.[9–13] They tested CuF_2, BiF_3, SnF_2 and $KBiF_4$ as cathodes, Ce as the anode, and $La_{(1-x)}Ba_{(x)}F_{(3-x)}$ ($0 \leq x \leq 0.15$) as the solid electrolyte. These batteries only worked at high temperatures (~150°C) due to the poor ionic conductivity of the solid electrolyte at room temperature. Since then, many other metal fluorides have been investigated as conversion electrode materials, and liquid electrolytes have been researched in addition to solid electrolytes.[13]

Most of FIBs—as the one demonstrated by Fichtner and Reddy—employ conversion-type electrodes that undergo the following reactions during cycling.

At the cathode side: $$x e^- + MF_x \leftrightarrow M^0 + xF^-$$

At the anode side: $$yF^- + M^{0'} \leftrightarrow M'F_y + ye^-$$

During discharge, the metal fluoride at the cathode gets reduced to its metal, whilst at the anode the metal gets oxidised to its metal fluoride. And upon recharge, the opposite process occurs.

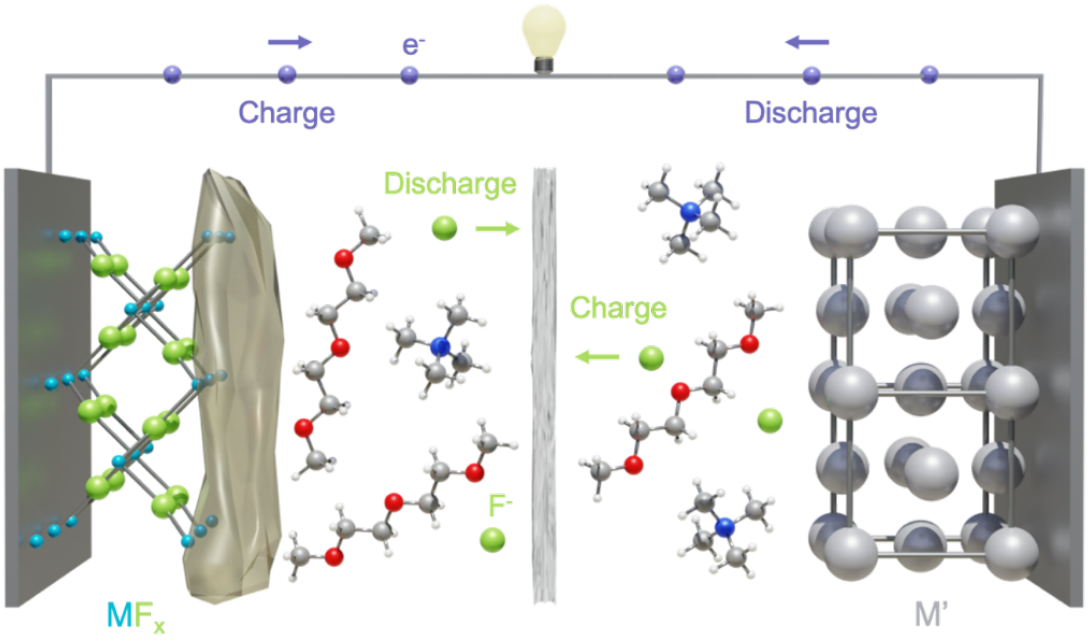


Figure 1.3: Schematic of a fluoride-ion battery in its charged state. During discharge the metal fluoride (cathode) reduces, releasing F-ions into the electrolyte, whereas the metal (anode) oxidises, liberating electrons into the external circuit.

FIBs have several advantages, some of which are shared with LIBs. The large voltages of LIBs are due to the large reductive stability of Li-ions which allows for high-voltage redox pairs to be used. Similarly, F is the most electronegative element in the periodic table and F-ions are extremely stable against oxidation. As a result, FIBs—alike to LIBs—can employ higher-voltage redox pairs, displaying large voltages and high energy densities. In FIBs, high energy densities may also arise from the multiple-electron redox reactions at the electrodes.[6] Furthermore, fluorine—like lithium—is the smallest and lightest element within its group allowing for faster ionic transport compared to similar anionic chemistries (Cl^-). Finally, fluorine is the 13th most abundant element in the Earth's crust, present as fluorspar (CaF_2). The global annual production of fluorspar is over 3.5 million tons, surpassing the production of lithium by approximately two orders of magnitude.[6,14,15] FIBs can therefore be proposed as a low-cost, high-energy density technology with the potential of contributing towards the green transport revolution.

1.3 How FIBs Compare to LIBs

Despite the numerous theoretical advantages of F-ions and FIBs mentioned previously, it is important to establish how they translate into battery performance and how this compares to other promising chemistries. In the literature energy densities of up to 5000 Wh L^{-1} have been quoted for FIBs. As appealing as these would be, these are far from realistic because they do not consider constraints imposed by cell design and refer to unpractical materials. To obtain a more accurate understanding of the appeal of FIBs, as part of our perspective article my co-author (A. W. Xiao) developed a techno-economic analysis to compare the energy density and cost of the most promising FIB chemistries to two of the best-performing LIB chemistries.[6] In addition to energy density and cost, safety was also included as a criterion for comparison.

In this analysis, realistic assumptions in terms of electrode thickness and porosity, active material loading, and electrolyte content were used. Promising FIBs chemistries were compared to a Li-ion battery having NMC622 as the cathode and graphite as the anode and a high energy density near-future Li-metal battery with NMC811 as the cathode. Three conversion-type FIBs as well as two intercalation-type cells were modelled to reflect different possible scenarios.

All the conversion FIBs exhibit higher gravimetric and volumetric energy densities compared to the two Li configurations (Fig. 1.4-a), with Cu|CaF_2 displaying the highest energy densities of almost 600 Wh kg^{-1} and 1400 Wh L^{-1}. These higher energy densities also come at a much lower cost. The projected cost of a Cu|CaF_2 cell is around USD 20 per kWh which is around half of the cost of the two Li chemistries.

The intercalation chemistries (e.g., $LaSrMnO_4$ vs $Sr_2TiO_3F_2$), on the other hand, exhibit considerably lower energy densities and higher costs. For the time being intercalation

FIBs are, therefore, not suitable for high-energy density applications, as well as non-competitive in term of cost with Na-ion or K-ion in the lower energy density scenarios.

Besides conversion chemistries showing an advantage over intercalation ones, liquid electrolytes show an advantage over solid ones. All the FIBs configurations displayed in Fig. 1.4 were modelled with a hypothetical F-ion conducting liquid electrolyte. If the liquid electrolyte was instead replaced by a CaF_2 solid electrolyte the higher gravimetric mass would reduce the gravimetric energy density to around 400 Wh kg^{-1}. In reality, CaF_2 cannot be used, since its ionic conductivity is too low to enable cycling at RT. Whereas the solid electrolytes that do cycle at room temperature contain minerals considerably heavier than CaF_2, which will further lower the gravimetric energy density.[16,17] Overall, the techno-economic analysis shows that for FIBs to be competitive and have an advantage in terms of energy density over LIBs, conversion-type electrodes with liquid electrolytes should be used.

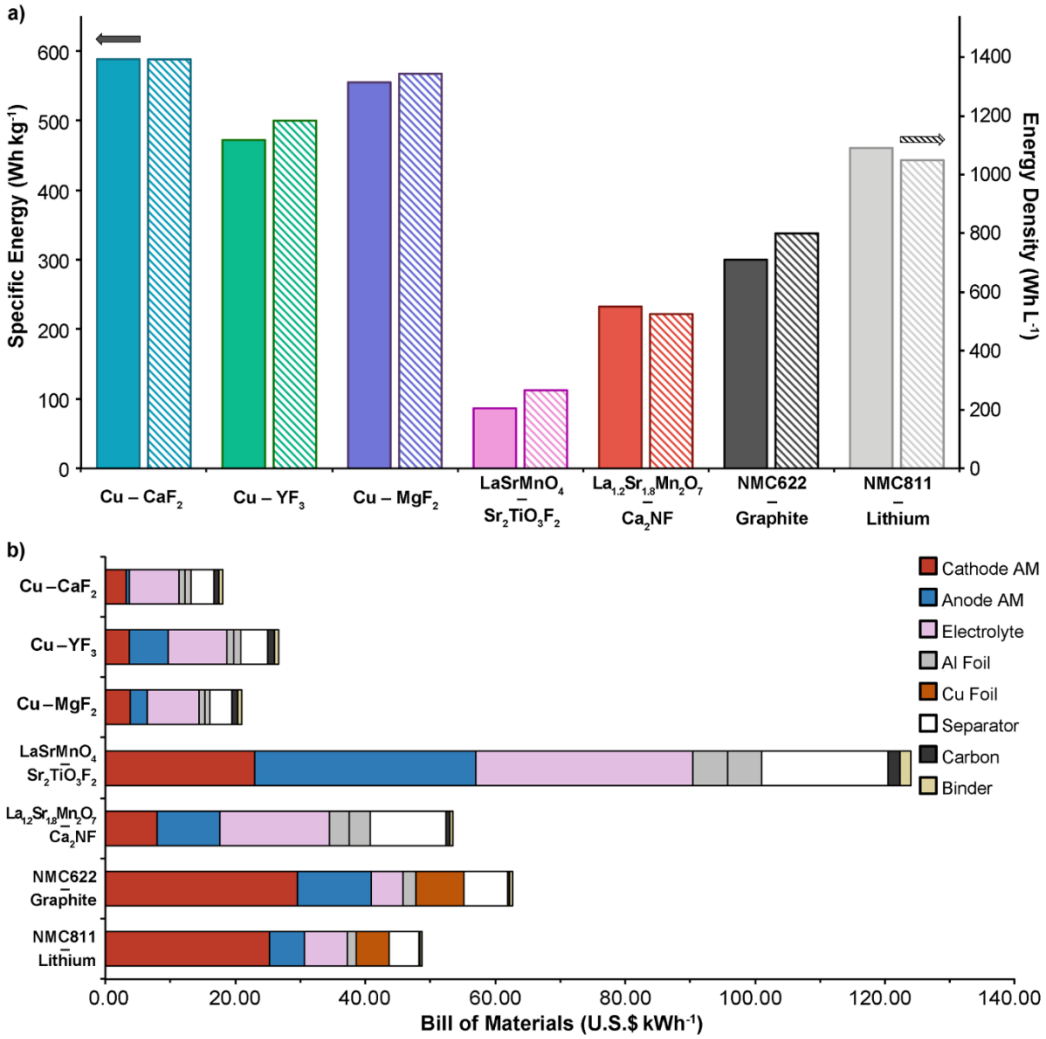


Figure 1.4: Techno-economic analysis. **(a)** Bar chart showing the projected stack-level energy densities of various FIB and LIB chemistries. Solid bars correspond to specific energy values displayed on the left axis, whereas hollow bars correspond to volumetric energy density values shown on the right axis. **(b)** Chart showing the corresponding materials cost for the battery stacks shown in (a), normalized by their respective specific energies.[6]

From a safety perspective, FIBs do not pose the same challenges as Li-ion or Li-metal batteries (Fig. 1.5). The electrodes of conversion FIBs do not contain oxygen eliminating the risk of O_2 evolution and thermal runaway. Fluorine evolution occurs at a much higher potential than oxygen—3 V vs PbF_2/Pb (5.9 V vs Li^+/Li) compared to 1.4 V vs PbF_2/Pb (4.3 V vs Li^+/Li)—making it unlikely to occur.[6] Additionally, the absence of metal plating at the anode side excludes the possibility of dendrite formation avoiding the risk of short circuiting. As a

result, fluoride-ion batteries eliminate the main safety shortfalls of LIBs, despite posing a set of new challenges. The possibility of forming the corrosive and toxic hydrogen fluoride in FIBs is the most serious safety concern that needs to be addressed.

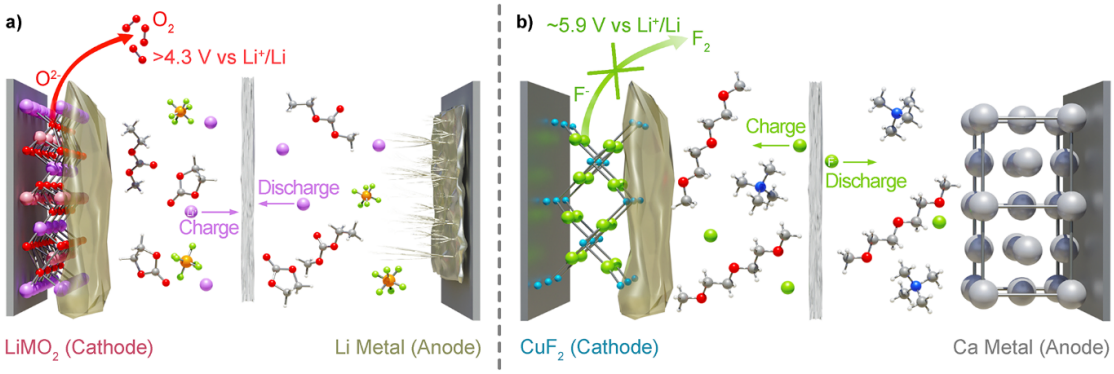


Figure 1.5: Lithium-ion batteries versus fluoride-ion batteries. **(a)** Schematic of a layered metal oxide-lithium-metal cell with a conventional carbonate-based electrolyte. Dendrites can grow from the Li-metal anode, leading to capacity loss and potential short circuits. Oxygen evolution occurs from the oxide cathode in the charged state (>4.3 V vs Li^+/Li) and can result in exothermic decomposition of the electrolyte. **(b)** Schematic of a hypothetical conversion-type fluoride-ion battery with a CuF_2 cathode, a Ca anode, and a liquid fluoride electrolyte. The higher redox potential of $2F^- \rightarrow F_2 + 2e^-$ (5.9 V vs Li^+/Li) results in greater oxidative stability for the cathode. Dendrites are not expected at the anode, as no plating of metal occurs.[6]

1.4 Critical Research Fronts of Fluoride-Ion Batteries

FIBs have numerous advantages over other technologies and have the potential to play a decisive role in the decarbonisation of transports and the reduction of our demand for Li, Ni and Co. However, many issues must be resolved before FIBs can become a viable technology. There are three major research fronts that are critical to the success of this technology: (1) selection of inactive components and testing set-up, (2) electrolyte design and (3) investigation of conversion mechanism.[6] This thesis will focus on the first two (Fig. 1.6).

(1) Extensive research should be carried out on the inactive components of the battery, including binder and separator. Most of the standard materials used in LIBs are incompatible with F-ions and alternatives should be sought. This research front is particularly important as unstable components raise safety concerns as they may produce the corrosive HF and other

harmful substances. Additionally, reliable and reproducible testing conditions should be established so that performance across different studies can be compared.

(2) The design of a suitable electrolyte for FIBs would provide the greatest advancement of the field. Particular focus should be paid to chemical stability, a wide electrochemical stability window to ensure high energy densities and the formation of a stable solid electrolyte interphase (SEI) to avoid active material dissolution.

(3) Finally, the last critical research front is the understanding of the charge/discharge mechanism of conversion-type fluoride electrodes. The uncovering of the structural orientation relationships and lattice matching at the metal-metal fluoride interface would be invaluable to expose inherent limitations of some materials, as well as reveal the possible advantages of others in terms, for example, of cycling stability.

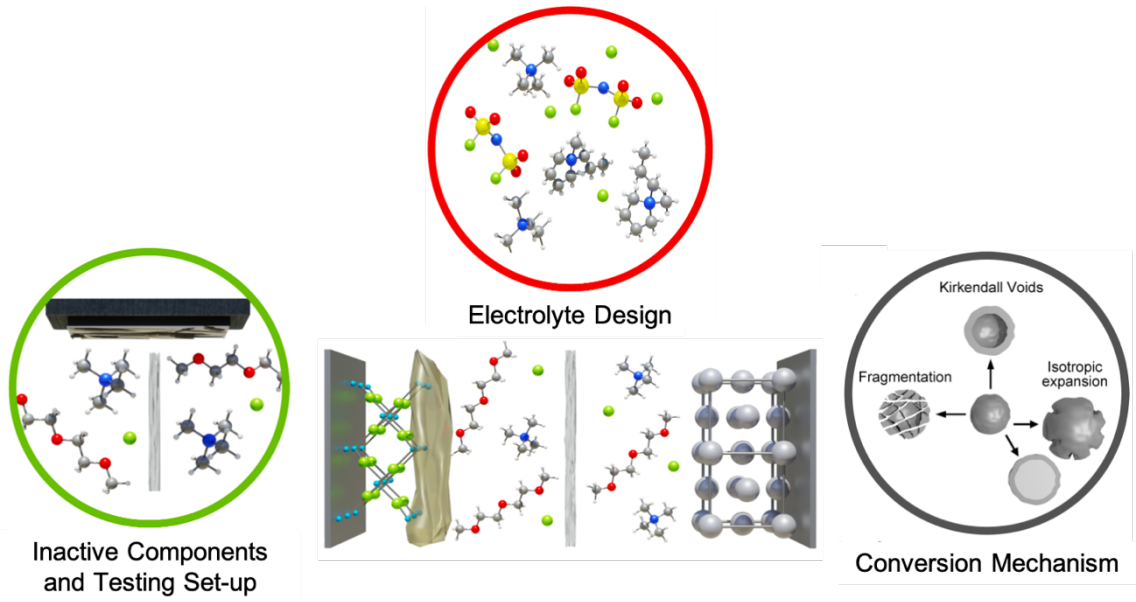


Figure 1.6: Critical research fronts. This work focuses on the selection of inactive components and testing set-up for liquid electrolyte FIBs, and on the design of novel liquid electrolytes.

In the remaining part of this introductory chapter, I will discuss the progress that has been made so far in the literature on the two critical research fronts that I have tackled in this thesis: 1) selection of inactive components and testing set-up, and 2) electrolyte design. In

particular, I will highlight the problems that still need to be solved in these two areas and what strategies I have selected to address them.

1.5 Inactive Components and Testing Set-up

The level of development of the inactive components in FIBs is very different to that in LIBs. In LIBs, extensive efforts have been made over the years to optimise the inactive components and maximise performance. Numerous binders and separators have been thoroughly investigated and their performance and chemical stability monitored over time. In contrast, FIBs are still in the early stages of development and very little work has been done on developing their inactive components. Generally, the materials developed for LIBs have simply been used in FIBs without any consideration of their compatibility. This is not as much of a problem in all-solid-state cells (ASSCs), since a separator is not required, and a binder is not always necessary. Liquid cells, on the other hand, cannot function without either a separator or a binder.

Polyvinylidene fluoride (PVDF) is the most common binder in LIBs and the standard in FIBs too. This is the case despite its well-known chemical degradation in the presence of F-ions.[18] Moreover, not a single study has focused on investigating possible alternatives. Yamamoto et al. were the only ones to introduce a different binder—polytetrafluoroethylene (PTFE)—instead of PVDF in their two studies on ionic liquids for FIBs. However, the decision to use PTFE was not justified in any way and only mentioned in the methods section.[19,20] This could explain why no one else has adopted PTFE as a binder, except for one study by Yaokawa et al. three years later.[21]

As for the separator, almost all FIBs studies have avoided its presence by using flooded or beaker cells. The studies that included a separator did not investigate its feasibility, or only did so in a rather limited way.[21] Flooded cells maintain the electrodes spatially separated

ensuring no electrical contact. Despite being far from practically viable, this configuration has been preferred because it accommodates a large electrolyte excess which compensates for electrolyte degradation. Only one study by Gschwind et al. has looked into the effect of different separators in FIBs. [22] A polyurethane sponge and two different types of cellulose were tested, whilst silicate fibres were discarded due to possible side-reactions resulting in HF and H_2SiF_6. The cells with the polyurethane sponge and the thick intercrossed cellulose membrane displayed the highest discharging capacities, with the latter exhibiting the smoothest profile. The thin cellulose paper, on the other hand, exhibited almost no discharge capacity. Unfortunately, this was the extent of the investigation, and no test on their chemical stability and wetting properties was done, making it hard to draw a definite conclusion from these results. Two other studies included separators in their FIBs cell configuration: Yamamoto et al. used a PTFE membrane as the separator, in addition to the PTFE binder already mentioned, whereas Yaokawa et al. used a polyethylene (PE) membrane.[19,21] However, in both cases, no investigation on the feasibility of either of the two separators was reported, especially regarding their wettability, given the non-polar nature of both polymers, particularly PTFE.

Another challenge of FIBs is the lack of a reliable and chemically stable counter-reference electrode for 2-electrode cells. Even when the objective is to study the performance of only one of the two electrodes—working electrode (WE)—the presence of the other electrode—counter-reference electrode—is required for the electrochemical reaction to take place. It is crucial that the counter-reference electrode exhibits stable cycling with a well-defined redox potential, as this enables the successful investigation of the WE. In such a case the cycling behaviour observed in a 2-electrode cell, including capacity, capacity retention, voltage hysteresis, is not limited by the counter-reference electrode and can be entirely ascribed to the WE. In LIBs Li metal is often used as the counter-reference electrode in a 2-electrode

cell. The reason being that it exhibits a stable redox potential during cycling in non-aqueous electrolytes, and it provides a virtually infinite and kinetically fast source of Li-ions. Unfortunately, the analogue to Li metal does not exist in FIBs, as F_2 is a gas and is therefore not suitable as an electrode. This lack of a counter-reference electrode has driven the use of flooded cells, which allow the use of an unstable counter electrode thanks to the presence of an additional electrode (the reference electrode). However, flooded cells do not provide a realistic measure of performance given the large excess of electrolyte and the absence of a separator. Additionally, in many cases Pt is used as the counter electrode. Since Pt does not take part in the electrochemical conversion, it will inevitably decompose the electrolyte during cycling.[21,23]

Very few studies have tried to develop a stable counter-reference electrode, and none have succeeded. Nowroozi et al. proposed the use of intercalation compounds, particularly La_2CoO_4, as counter-reference electrodes.[24] The justification being that lower volume-changes during cycling may provide better capacity retention compared to conversion-type electrodes. However, in addition to the presence of an unknown decomposition reaction in the first cycle, the synthesis procedure of La_2CoO_4 is not straightforward, making it an impractical candidate. Furthermore, the elevated cycling temperature (170°C) due to the low ionic conductivity at RT of the solid electrolyte used, and the lack of symmetric $La_2CoO_4|La_{0.9}Ba_{0.1}F_{2.9}|La_2CoO_4$ cycling data available cast doubt over its good cyclability at RT and its suitability as a stable counter-reference electrode. In general, the complex synthesis procedure and the absence of performance improvement compared to conversion-type electrodes make intercalation electrodes unappealing solutions as routine counter-reference electrodes.[24–26] As for conversion-type counter-reference electrodes, Pb-PbF_2 has been the most commonly used material due to its better cyclability and lower hysteresis when compared to other fluorides. However, no study has either investigated its suitability as a stable counter-reference electrode

nor reported a reliable and systematic procedure for its fabrication. For instance, in some studies a Pb rod or plate is used, in others the Pb rod is electrochemically fluorinated, and in other cases Pb or PbF_2 powders are mixed with PVDF in order to make the electrode.[27–29] This lack of consistency makes it difficult to compare results across different studies.

Hence, the investigation into a suitable separator, binder, and counter-reference electrode will allow the use of more realistic form-factors (such as coin or pouch cells). This is a necessary step to improve the performance of FIBs.

1.6 Electrolytes for FIBs

As previously mentioned, the second critical research front is the design of a suitable electrolyte for FIBs. The electrolyte is the liquid or solid component of the battery that conducts ions between the electrodes but is insulating towards electrons to avoid short circuiting. A good electrolyte should be chemically stable (does not degrade over time), have a wide electrochemical stability window (does not get reduced or oxidised within the working potential of the battery), have a high ionic conductivity at RT, have good transport properties, and finally have low volatility (in the case of liquids). To date, an electrolyte that satisfies all these requirements has not been reported for FIBs. Achieving a wide electrochemical stability window has proved one of the most difficult criteria to meet, with most electrolytes being stable at high potentials but not at low ones.

To fulfil the primary objective of FIBs, which is achieving elevated energy densities without relying on critical battery materials, electrode pairs with significant voltage differences should be used. This, in turn, necessitates a wide electrochemical stability window (ESW). The theoretical energy density of a battery is a function of the redox potential between the electrodes, their molecular weight and the number of electrons transferred (eq. 1.1, 1.2).

$$\text{Energy Density} = E^\circ\, Q \tag{1.1}$$

$$Q = \frac{z\,F}{M} \tag{1.2}$$

Where E° is the cell voltage (V), Q is the specific capacity (mAh g^{-1}), z is the number of electrons transferred, F is Faraday's constant (C mol^{-1}), and M is the molecular weight of the active material (g mol^{-1}).

To design a suitable electrolyte, it is important to understand which electrode pairs are the most promising in terms of energy density and what electrochemical stability window they require to cycle. Some of the binary metal fluorides that exhibit the lowest and highest redox potentials are shown in Fig. 1.7-a, with their redox potential referenced to PbF_2/Pb. The most promising combinations of these metal fluorides are shown in Fig. 1.7-b with their theoretical energy density and voltage difference. CuF_2|Mg is the redox couple exhibiting the highest theoretical energy density of almost 1400 Wh kg^{-1} and a voltage difference of ~3.2 V. Another promising redox couple is CuF_2|Ca which displays an even larger voltage difference of 3.4 V. The ideal electrolyte should therefore exhibit an ESW of nearly 4 V if the reaction overpotentials are considered.

It is worth noticing that the size of the electrochemical stability window is not the only important factor, as the upper and lower limits are equally important. For example, an ESW of 4 V which has a lower limit close to the potential of PbF_2/Pb is of no use, since the redox potential of any promising anodes would lay well outside of the ESW. Both limits of the ESW should therefore be close to the redox potential of the most promising cathodes and anodes. There is room for some flexibility when taking into account the formation of passivating cathode/solid electrolyte interphases, which protect the electrolyte from being oxidised or reduced and would allow to cycle electrodes whose redox potential is outside the ESW.[30,31] However, this strategy only accommodates small mismatches between the limits of the electrochemical stability window and the redox potential of the electrodes. During the design

of a novel electrolyte, it is therefore important to bear in mind that an ESW that satisfies the most promising electrode pairs must have a width of 3.5 to 4 V and anodic and cathodic limits close to the redox potential of CuF_2/Cu and CaF_2/Ca or MgF_2/Mg, respectively.

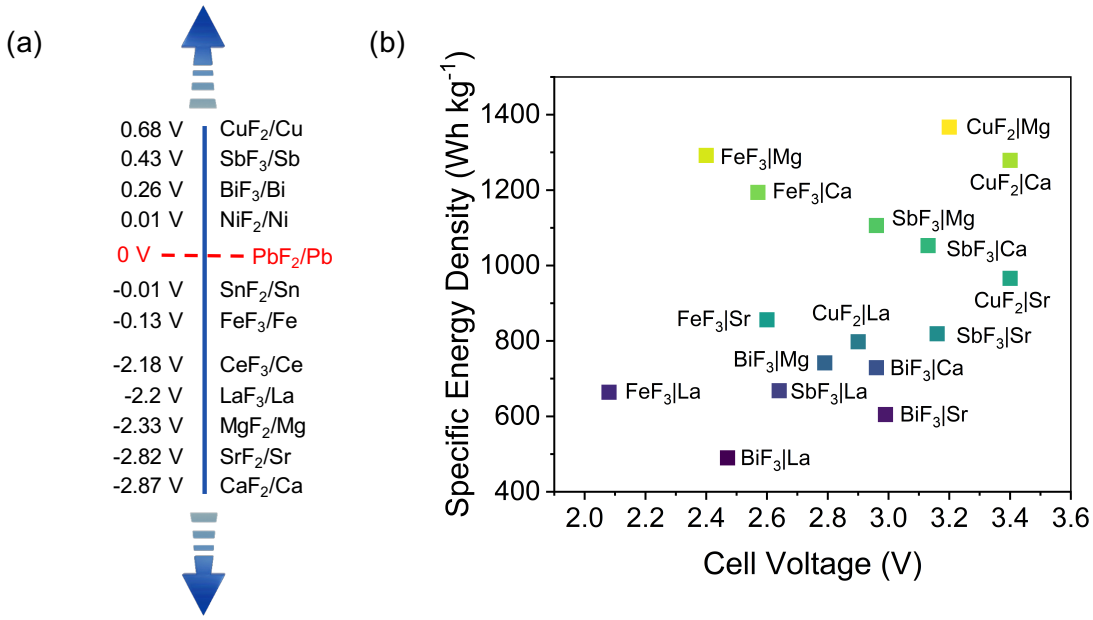


Figure 1.7: **(a)** Electrochemical series showing a selection of binary fluorides with their redox potentials displayed versus PbF_2/Pb; **(b)** Comparison of specific energy density versus cell voltage for a number of binary fluorides. The three materials with the highest redox potentials, CuF_2, SbF_3 and BiF_3, and four of the materials having among the lowest redox potentials, Ca, Mg, Sr and La, were selected for the comparison. FeF_3 was also included in the graph because of its high energy density, despite the lower redox potential. The energy densities displayed are purely theoretical and their sole purpose is to compare different materials together. CuF_2|Mg exhibits the highest specific energy density, whereas CuF_2|Ca the largest cell voltage.

1.6.1 Solid versus liquid electrolytes

While designing an electrolyte, the first decision to make is whether to select a solid or a liquid electrolyte. Both types have been investigated for FIBs and each exhibit several advantages as well as a number of challenges (Fig. 1.8).

Solid electrolytes are less chemically reactive, tend to have a wider electrochemical stability window and are less expensive compared to liquids.[6] However, most solids have impractically low ionic conductivities at room temperature, and the ones having higher conductivities exhibit narrower ESWs. Furthermore, the higher density of solids results in

much lower gravimetric energy densities. Solids are also incapable of accommodating the large volume changes occurring at the electrodes during cycling, leading to interfacial contact losses and capacity fading. Additionally, solid electrolytes are incompatible with standard manufacturing techniques, and on a large scale it is hard to achieve good interfacial contact between the solid electrolyte and the electrode material. [6]

Moreover, the reasons that have justified the study of solid electrolytes in LIBs, particularly non-flammability and prevention of dendrite propagation, do not apply to FIBs. Although solid electrolytes may still offer improved safety in case of battery puncture or short-circuit, the chance of a spontaneous exothermic reaction with FIBs electrolytes is significantly diminished if oxygen-free cathodes are used. Additionally, due to the absence of metal plating during cycling, dendrites do not form in FIBs.[6]

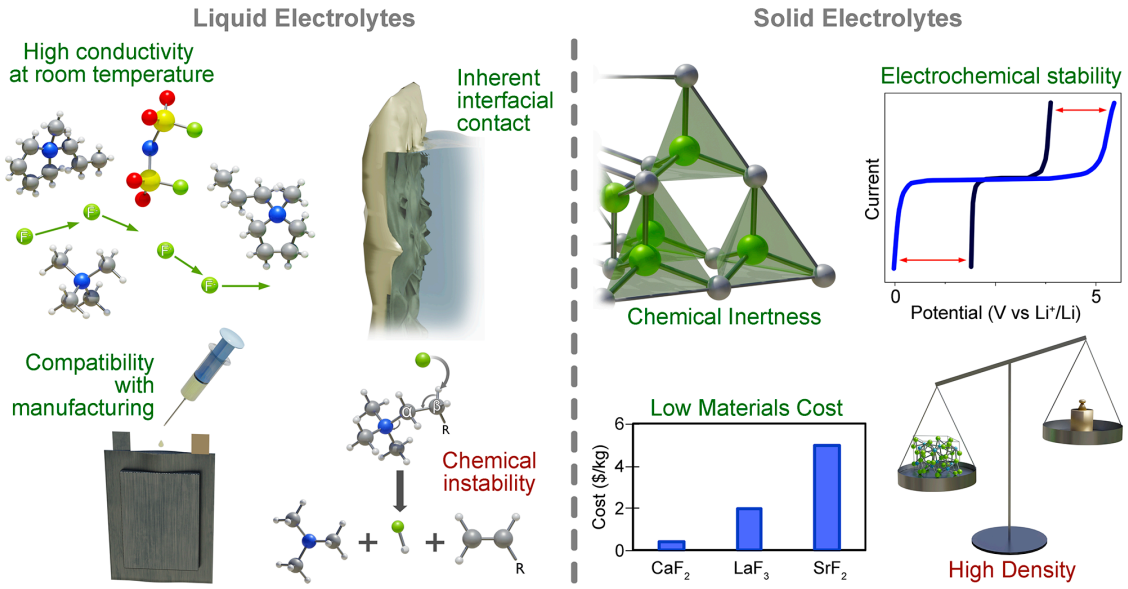


Figure 1.8: Comparison between liquid and solid electrolytes for FIBs. The advantages (in green) and the disadvantages (in red) are shown for both liquid and solid electrolytes. [6]

Liquid electrolytes, on the other hand, have superior transport properties, can accommodate the volume changes occurring at the electrodes, and are compatible with current manufacturing techniques. Additionally, they can achieve much higher gravimetric energy

densities thanks to their lower density. Developing liquid electrolytes for FIBs, however, is not trivial as fluoride salts have extremely poor solubility in aprotic organic solvents—which are the common solvents used in batteries. Additionally, chemically stable electrolytes are difficult to synthesise because of the high reactivity of the F-ion in aprotic solvents, which arises from its high basicity and nucleophilicity. The nucleophilic nature of the F-ion is partly a consequence of its small ionic radius, which allows it to form strong ionic bonds.

In the remaining part of this chapter, I will provide an overview of the electrolytes that have been reported in the literature with their advantages and shortfalls. I will mention solid electrolytes briefly and discuss more in detail liquid electrolytes, since my work in this thesis focused on this type.

1.6.2 Solid electrolytes

The solid electrolytes reported in the literature, except for a few exceptions, can be broadly divided into two classes: tysonite-type (LaF_3 prototype) and fluorite-type (CaF_2 prototype) structures. Since the ionic conductivity of both types of structure is not sufficient at RT, several approaches have been explored in the literature to increase their ionic conductivity, including doping and different manufacturing methods.[32] Unfortunately, in most solid electrolytes a higher ionic conductivity at RT is accompanied by a narrower electrochemical stability window, making the electrolytes unsuitable for high-energy density applications. An example is the fluorite-type $BaSnF_4$ solid electrolyte, which exhibits a decent ionic conductivity of 10^{-4} S cm^{-1} at RT, however the presence of Sn limits the ESW, and therefore the electrode choice.[33] To combine a high ionic conductivity and a wide ESW, Mohammad et al. designed an interlayer electrolyte.[34] A 90 μm thin layer of $La_{0.9}B_{0.1}F_{2.9}$ was placed in contact with the Ce anode to exploit its wide electrochemical stability window. Whereas the bulk of the solid electrolyte was made from $BaSnF_4$ to achieve a higher ionic conductivity at RT.

Unfortunately, the cycling performance turned out to be very poor, with the maximum discharge capacity not exceeding 25 mAh g^{-1}.

The best performance of any solid electrolytes reported to date was displayed by $CsPb_{0.9}K_{0.1}F_{2.9}$, which has a perovskite crystal structure. This material exhibits superionic conductivity at room temperature, comparable to liquid electrolytes (>10^{-3} S cm^{-1}). Wang and Ma demonstrated the reversible cycling of a Ag|$CsPb_{0.9}K_{0.1}F_{2.9}$|Pb-PbF_2 cell which exhibited the best performance ever reported for a FIB.[16,35] In fact, the cell displayed reversible cycling for 100 cycles with 80% capacity retention (152.5 mAh g^{-1}) at RT. The impressive performance of $CsPb_{0.9}K_{0.1}F_{2.9}$ is, however, coupled with high density (leading to low gravimetric energy density) and the toxicity of Pb. These results show how the solid electrolytes that exhibit the most promising performance are also the ones containing the most impractical elements. The high density of solid electrolytes therefore does not satisfy one of the two requirements for the success of FIBs: achieving high gravimetric energy density. For this reason, my work in this thesis has focused on liquid electrolytes.

1.6.3 Liquid electrolytes

Two main strategies have been adopted in the literature to create liquid electrolytes for FIBs. The first one involves dissolving a fluoride salt into an ionic liquid, whereas the second one uses anion acceptors, or compounds with similar function, to increase the solubility of inorganic fluoride salts in aprotic organic solvents.

Ionic liquid electrolytes

Ionic liquids are salts that are molten at room temperature. The advantage of using ionic liquids as solvents for liquid electrolytes is that they can dissolve a wide variety of compounds, are stable over a broad range of temperatures, have wide electrochemical stability windows,

and are non-volatile and non-flammable. The main disadvantages of using ionic liquids, however, are worse transport properties due to their high viscosity, and high cost.

The use of ionic liquids in FIBs carries an additional problem. Most cations of ionic liquids contain β-hydrogens. A β-hydrogen is defined as a hydrogen attached to the second carbon—the β-carbon—in a functional group. This hydrogen is susceptible to Hofmann elimination if the environment is sufficiently acidic. In this degradation mechanism, the F-ion extracts the β-hydrogen, resulting in the formation of the corrosive HF (Fig. 1.9).

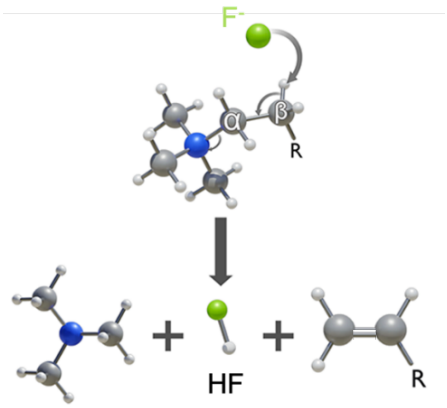


Figure 1.9: Hofmann elimination. A β-hydrogen is extracted by F^- (strong base), resulting in the formation of HF, an amine, and an alkene.

All the ionic liquid electrolytes found in the FIBs literature contain β-hydrogens, and no mention of their long-term stability is ever made. An example is the electrolyte made by dissolving an organic salt, 1-methyl-1-propylpiperidinium fluoride, in N,N,N-trimethyl-N-propylammonium bis(trilfuoromethanesulfonyl)amide. Despite its reasonably good ionic conductivity of 2.5 mS cm^{-1} at RT coming from the ability to dissolve the salt up to 0.35 M, the presence of β-hydrogens and the inevitable formation of HF make this electrolyte impractical.[36] A fluorohydrogenate ionic liquid—[1-ethyl-3-methylimidazolium][(FH)2.3F]—has also been investigated because of its exceptional ionic conductivity (~100 mS cm^{-1} at 25°C), due to the weak ionic interactions arising from fast HF exchange between $[(FH)nF]^-$

anions.[37] Additionally, using the ionic liquid anion (HF_2^-) as the main charge carrier removes the need for a fluoride salt dissolved in the electrolyte, which improves the transport properties. In this case, a chemical degradation causing HF does not occur, but the presence of $[(FH)nF]^-$ anions still raises safety concerns. An investigation on the corrosivity and safety of this electrolyte should be carried out before this class of ionic liquids could even be considered as a viable option. Despite this major drawback and the narrow ESW of 0.7 V, it is worth noticing that this is the only case in which CuF_2 has been cycled reversibly (in a liquid electrolyte) with a capacity close to the theoretical value.[20,38]

Ionic liquids are a promising strategy to produce liquid electrolytes for FIBs since some of them are capable of dissolving fluoride salts without any additive. However, their success will rely on the absence of β-hydrogens and other molecules similar to HF. Achieving chemical stability with ionic liquids is one of the objectives of this thesis.

Electrolytes containing anion acceptors or similar compounds

The second approach, as mentioned earlier, exploits anion acceptors (AA) to help dissolve a fluoride salt in an organic solvent by binding to F^- via Lewis acid-base interactions. For AAs to provide a satisfactory performance they must have a moderately strong affinity for F-ions. Too weak an affinity causes insufficient dissolution of the fluoride salt into the electrolyte. Whereas an excessively strong affinity impedes discharge by preventing the release of the F-ions from the AA to the electrode.[39] The majority of liquid electrolytes for FIBs exploit this strategy, and it is therefore pertinent to discuss in detail the several configurations tested. Different chemistries and ratios of AAs have been investigated to attempt addressing the problem of limited solubility of the fluoride salt (leading to low ionic conductivity), as well as the issues with active material dissolution and narrow electrochemical stability window.

The first electrolyte prepared using this approach was 0.45 M cesium fluoride (CsF) in tetraglyme (G4), with the addition of 0.5 mol L^{-1} of a boron-based anionic acceptor (fluorobis (2,4,6-trimethylphenyl) borane: FBTMPhB). [40] The AA increases the solubility of CsF in tetraglyme by reducing the cation-anion interaction between Cs^+ and F^-. The electrochemical stability window was measured using cyclic voltammetry (CV) and found to be 1.9 V wide—between -1.2 V and 0.7 V vs PbF_2/Pb. This ESW allows cycling some of the most promising cathodes such as BiF_3 and CuF_2, but it does not reach to the low potentials of the most appealing anodes—CaF_2, MgF_2. Using this electrolyte, the cycling performance of BiF_3 in a half cell was investigated. Despite reaching almost the theoretical capacity on the first discharge, extremely large capacity fading occurred in the subsequent cycles, reaching 50 mAh g^{-1} on the third discharge. This was attributed to the dissolution of the active material into the electrolyte as well as the consequent electrolyte degradation. It was later discovered that by increasing the ratio of CsF/FBTMPhB in the electrolyte, the dissolution of the active material could be

mitigated, improving capacity retention.[41] Similar results were also obtained by cycling PbF_2 instead of BiF_3.[42]

In later studies, two other boron-containing AAs were investigated—triphenylboroxine (TPhBX) and triphenylborane (TPhB).[28,29,43,44] Despite dissolving a higher concentration of CsF in G4 compared to FBTMPhB, significant active material dissolution was still observed for both BiF_3 and PbF_2, leading to poor cycling.

Later, lithium bis(oxalato)borate (LiBOB) attracted interest because of its ability in LIBs to inhibit the dissolution of the active material by forming a stable cathode electrolyte interphase (CEI). LiBOB is not an anion acceptor but it could be tested in FIBs because of its ability to dissolve CsF in G4, thanks to the interaction of BOB^- with Cs^+ via ion-exchange.[23] However, the maximum solubility of CsF in LiBOB/G4 was found to be 4.4×10^{-3} mol dm^3, which is lower than the amount dissolved by AAs.[39] The ESW appeared to be slightly larger (2.3 V) in the case of LiBOB compared to FBTMPhB. However, side reactions and electrolyte degradation were observed, especially at low (1 wt%) and high concentrations (9 wt%) of LiBOB, which resulted in very poor cycling performance.[23]

Other two different boron-based AAs with different acidic strengths—(4-(4,4,5,5-tetramethyl-1,3,2-dioxaborolan-2-yl)pyridine; DiOB-Py) and (N,N-diethyl-4-(4,4,5,5-tetramethyl-1,3,2-dioxaborolan-2-yl)aniline; DiOB-An)—were investigated by Celik Kucuk and Abe.[39] Both DiOB-Py and DiOB-An were used at 0.5 M concentrations to dissolve saturated CsF in G4. Although the solubility of CsF in DiOB-Py/G4 was 1.8 times higher than in DiOB-An/G4, concentrations higher than 0.03 M could not be achieved, leading to ionic conductivities in the order of 10^{-5}-10^{-6} S cm^{-1}. The higher solubility of CsF in DiOB-Py/G4 was not surprising as the borate has higher acidity in DiOB-Py compared to DiOB-An. Despite the low ionic conductivity, CsF/DiOB-Py/G4 exhibited a larger ESW (2.6 V) compared to the

previously discussed electrolytes, and more importantly improved cycling. Full conversion of BiF_3 to Bi was achieved on the first discharge at C/40, although the capacity being higher than the theoretical value indicates some ongoing electrolyte decomposition. On recharge Bi could not be fully converted back to BiF_3 but a capacity of 260 mAh g^{-1} was achieved, which is higher than what had been reported with other AAs. Additionally, the 2nd and 3rd cycles displayed stable cycling and very little capacity fading, due to the lack of active material dissolution into the electrolyte (≤ 0.1 ppm). However, no data was shown after the 3rd cycle, making it impossible to establish the long-term cycling stability. Improved cycling performance was also observed with the CsF|DiOB-Py|G4 electrolyte at higher (dis)-charge rates, despite being worse than C/40. Among the different anionic acceptors, DiOB-Py appears to provide the best cycling performance for BiF_3 by suppressing active material dissolution.

In order to reduce the cost of the electrolyte, less expensive metal fluorides—NaF and KF—were tested instead of CsF in DiOB-Py|G4.[45] However, only 25 ppm of NaF could be dissolved in the electrolyte, making the salt practically insoluble. KF, instead, could be dissolved up to 245 ppm, which was still five times lower than the maximum concentration of CsF. Due to the low solubility, the ionic conductivity was found to be extremely low at 1.02 x 10^{-5} S cm^{-1}. In any case, KF|DiOB-Py|G4 was capable of cycling BiF_3 reversibly for up to 30 cycles at C/40 and up to 10 cycles at C/10, despite exhibiting large capacity fading. The capacity fading was attributed to the nature of the conversion mechanism which involves large crystal reorganisation rather than active material dissolution, as no Bi was detected in the electrolyte after full discharge or charge. However, a mechanistic study of the conversion mechanism of BiF_3/Bi is needed to prove this claim.

As the previously mentioned results show, significant improvements have been achieved during the optimisation process of AA electrolytes. These include a fairly wide ESW,

reducing active material dissolution and improving capacity retention during cycling. Nonetheless, performance is still far from satisfactory due to several unresolved issues. Capacity retention during cycling is still very poor, even in flooded cells which are known to overestimate performance due to the large electrolyte excess that masks any possible electrolyte degradation. Additionally, anion acceptors are still not capable of dissolving an amount of salt equivalent to what is commonplace in LIBs, which leads to low ionic conductivities. Also, even the widest electrochemical stability windows achieved with these electrolytes have low reductive stability, which prevents the cycling of the most promising anodes. Finally, the chemical stability for any of these electrolytes has never been reported, making it unclear whether degradation reactions are occurring.

The strategy of using anion acceptors is a sensible way to dissolve fluoride salts in solvents which would otherwise not solvate F-ions. However, this is not the only strategy available to achieve the same goal. Since anion acceptors have been thoroughly researched, it therefore seems worthwhile to investigate alternative strategies to see whether superior performance can be achieved. In effect, this is another of the objectives of my thesis work.

Other organic electrolytes

Besides ionic liquid- and anion acceptor-based electrolytes, other liquid electrolytes for FIBs have been reported. However, as in the case of ionic liquids, they also suffer from the presence of HF. An example is tetraethylammonium fluoride (TEAC) in polypropylene carbonate (PC), which contains β-hydrogens in both the cation of the fluoride salt and the solvent and will therefore inevitably form HF.[21] Another example is lactone-based electrolytes

which display clear degradation and HF_2^- formation.[46] Both of these electrolytes degrade over time because no effort was made during the design process to avoid HF formation.

The only study in this category of electrolytes that did attempt to avoid HF formation is the work done by Davis and co-authors, who designed an electrolyte without β-Hs.[47] In this study, neopentyl-substituted alkylammonium salts were dissolved in a partially fluorinated ether—bis(2,2,2-trifluoroethyl) ether (BTFE). The resulting electrolyte exhibited an exceptionally wide ESW of 4.1 V, which stretched from a cathodic limit of -2.2 V vs PbF_2/Pb to an anodic limit of 1.9 V vs PbF_2/Pb. Good transport properties were also reported with an ionic conductivity of ~3 mS cm^{-1} and transference number for F^- greater than 0.5. Bi and Pb could be cycled reversibly up to 10 cycles, although full conversion was never achieved. Cu, on the other hand, failed to cycle due to its dissolution into the electrolyte. As for the anode, Ce and Ca were tested with not much success, because they lay at the edge and outside of the cathodic limit of the ESW, respectively,

Despite the efforts of Davis et al. to avoid the presence of β-Hs, HF_2^- was detected in the electrolyte, and its amount continued growing over time while the concentration of F^- decreased. This was attributed to the presence of unknown protic impurities.[47] However, this explanation seems unlikely given how large the concentration of protic impurities in the electrolyte would have had to be to result in such a high concentration of HF_2^- (more than 10% of F^- had converted to HF_2^- after 100 days and kept increasing). Additionally, it seems incongruent that after 100 days the impurities had still not been depleted. The presence of HF in this electrolyte, which as just argued is most likely not caused by impurities, highlights the

difficulty in achieving the goal of chemical stability, which as previously mentioned is one of the objectives of my thesis work.

In the literature, different strategies have been tried to dissolve fluoride salts (ionic liquids and anion acceptors) and achieve chemical stability (organic salts and solvent without β-hydrogens). However, an electrolyte that satisfies all the necessary requirements and achieves satisfactory performance has not yet been reported.

Designing the ideal liquid electrolyte requires finding a chemistry that displays high salt solubility (to allow for good transport properties), has a wide electrochemical stability window, lacks β-Hs, and prevents active material dissolution.

1.7 Summary and Thesis Aim

Fluoride-ion batteries are a promising next-generation technology owing to their absence of critical minerals and high energy densities. From a theoretical standpoint, liquid FIBs that use conversion-type electrodes appear to be particularly promising in terms of both energy density and cost-effectiveness.

Currently, solid electrolytes outperform liquid electrolytes because they do not degrade over time and do not cause any active material dissolution. Nevertheless, the limited ESW, the presence of toxic and heavy components and the high temperatures required during manufacturing make even the most promising solid electrolytes unsuitable for practical applications.

Over the long term, liquid electrolytes could potentially deliver superior cycling performance in contrast to solids, due to their ability to accommodate significant volume changes at the electrodes. However, this improved performance is dependent on addressing the current issues that affect liquid electrolytes. Among them, chemical degradation over time and active material dissolution are the most problematic. Additionally, the lack of reliable testing

conditions for liquid electrolyte FIBs, and particularly the use of flooded cells, make it complicated to compare different studies.

This thesis aims at establishing a consistent and reliable testing methodology for liquid electrolyte FIBs, as well as introducing new design strategies for the development of liquid electrolytes. These new strategies could open up the path to reach satisfactory levels of performance for FIBs.

In **Chapter 3**, I propose a solution to the issues that have prevented coin cells from being used to cycle liquid electrolyte FIBs. In particular, I introduce a reliable counter-reference electrode, manufactured with a chemically stable binder, and a suitable separator. The combination of these components in a coin cell set-up allows for the accurate testing of the cycling performance of the novel liquid electrolytes reported in the following chapters.

In **Chapter 4**, I present a liquid electrolyte which uses a design strategy new to the field, consisting of a highly concentrated electrolyte with the addition of a diluent. This strategy addresses the problem of low solubility of fluoride salts in organic solvents. This electrolyte does not contain β-hydrogens and exhibits good transport properties. Additionally, it allows the cycling of metal fluorides with superior capacity retention.

In **Chapter 5**, I employ a different strategy to develop another novel liquid electrolyte for FIBs, which addresses the problem of chemical instability in liquid electrolytes. The ionic liquid-based electrolyte displays chemical stability over time, with no HF formation, for the first time in FIBs.

Chapter 2

Methods

Table of Contents

2.1 Introduction 33
2.2 Manufacturing Procedures 34
2.3 Materials Characterisation 39
2.4 Microscopy Techniques 47
2.5 Electrochemical Characterisation 49
2.6 Monte Carlo Simulations 55

2.1 Introduction

The first part of this chapter provides a detailed account of the manufacturing processes involved in electrode preparation, electrolyte synthesis, and cell assembly. The steps of each procedure are reported in detail to enable the reproducibility of the experiments. The second part of the chapter offers an overview of the analytical techniques used, this includes a brief account of the underlying theory, as well as a description of the parameters and sample preparation methods employed. Given the broad nature of the project, which spans from electrode manufacturing to electrolyte synthesis and cell cycling, many techniques were used. These techniques can, however, be broadly categorized under material characterisation, microscopy, or electrochemical techniques. Materials characterisation techniques include most of the methods used to verify the success of the manufacturing procedures, by analysing features such as particle size (DLS), crystal structure (XRD), purity (NMR for liquids and XRD, FT-IR for solids) and water content (KF titration). This section also includes some of the techniques employed to test the performance of the electrolytes in terms of chemical stability (NMR), transport properties (PFG-NMR for diffusion coefficient) and extent of active material dissolution (ICP). Microscopy techniques (SEM, p-FIB) were used to evaluate the success of the dry casting electrode manufacturing procedure by investigating the morphology

and homogeneity of particle distribution. Finally, different electrochemical techniques were used to characterise some electrolyte properties (LSV for electrochemical stability window and PEIS for ionic conductivity) and cell performance (GCPL). At the end of the chapter, the parameters for the Monte Carlo simulations, which were used to determine the solvation structure of the electrolyte in Chapter 4, are reported.

2.2 Manufacturing Procedures

2.2.1 Reduction in particle size

In Chapter 3, PbF_2 powder was ball milled inside an Ar-filled glovebox according to the following procedure. PbF_2 was wet ball-milled with octadecene and oleic acid for 12 hours at 700 rpm using seven-minute-long pauses every ten minutes. Oleic acid was added as a surfactant to stabilise the particles during milling. After ball milling the powder was washed with ethanol to remove the surfactant and hexane and dried at 100°C overnight under vacuum.

In Chapter 4, BiF_3 and CuF_2 powders were also ball milled prior to use with the same procedure used for PbF_2.

2.2.2 Manufacturing process for electrodes with PIB binder

In Chapter 3, polyisobutylene (PIB) was tested as a binder for FIBs. The slurry casting procedure used to manufacture the electrodes was the following. A 50 mg mL^{-1} solution of PIB in 1,2-dichlorobenzene was made and used at least 24 hours after mixing to ensure the complete dissolution of the polymer. 70 wt% active material, 20 wt% carbon black and 10 wt% PIB were then mixed and cast onto an aluminium foil with a doctor blade (opening 150 μm) in a Ar-filled glovebox. The casting was then allowed to dry inside the glovebox for a couple hours until it looked visibly dry. It was then further dried under vacuum at 80°C overnight to ensure the complete evaporation of the solvent. 10-mm diameter electrodes were punched out from

the casting. The same manufacturing procedure was used when carbon-coated aluminium foil was tested.

2.2.3 Extra details for dry casting of Pb-PbF_2 electrodes

Carbon nanofibres (CNFs) and polytetrafluoroethylene (PTFE) powder (675 μm particle size) were purchased from Sigma Aldrich and Goodfellow, respectively, and dried under vacuum at 100°C overnight. Electrodes manufactured via dry casting have similar composition to standard electrodes made via slurry casting, except for the lower content of binder. In the case of Pb-PbF_2 electrodes, 96 wt% of active material, 3 wt% of carbon and 1 wt% of PTFE were used. The 96 wt% of active material was further divided between Pb and β-PbF_2. The ratio between the two was tuned according to the electrodes used. To test the performance of Pb-PbF_2 electrodes, a symmetric cell configuration was used (Pb-PbF_2 as both the WE and CE). For convenience, the electrodes were manufactured in a 50% state of charge (SOC), meaning that the 96 wt% of active material was equally divided between Pb (discharged state) and PbF_2 (charged state). 50% SOC allowed to obtain both the WE and the CE from the same casting, speeding up the process optimisation. Pb-PbF_2 counter-reference electrodes for non-symmetric cells were manufactured using a different ratio. A higher Pb content was used to ensure that enough Pb atoms are present in the CE to accommodate the full reduction of the WE during discharge.

2.2.4 Coin cells assembly

CR2032 coin cells (20 mm diameter, 3.2 mm thickness) with stainless steel spacers (15.5 mm diameter, 0.5 mm thickness) (PI-KEM) were used. Omnipore hydrophilic PTFE membranes (30 μm thick, 0.1 μm pore size, 80% porosity) were employed as the separators.

First a 1-mm thick stainless-steel spacer was positioned in the centre of the coin cell bottom with the WE located on top. The WE was then wet with five drops of electrolyte and

covered with two 18-mm diameter hydrophilic PTFE separators. The surface of the second separator was then wet with additional five drops of electrolyte and the CE was located on top of it. The CE was then covered with a 0.5-mm thick SS spacer and a wavy spring. Additional electrolyte was added around the spacer to provide electrolyte excess. The coin cell case was then positioned on top, and the cell was crimped. Less than 150 µl of electrolyte was left inside the coin cell after crimping.

The coin cells used to measure the electrochemical stability of the separator in Chapter 3 were assembled in the same way. The only difference is the lack of the electrodes and the use of the stainless-steel spacers as the blocking electrodes.

2.2.5 Drying of commercial tetramethylammonium fluoride

The following is a novel multi-step drying procedure to lower the water content of commercial TMAF. Tetrahydrate TMAF was chosen instead of the non-hydrate form because of its lower cost, and because its higher water content does not have any adverse impact on the drying procedure. The method developed involves the following steps:

1. Tetrahydrate TMAF was heated at 150°C under vacuum for 24 hours to lower the water content to ~1.5%.
2. The dried TMAF was dissolved into anhydrous isopropanol ($H_2O \leq 15$ ppm) to release the crystallographic water into the solution. IPA was chosen because of its ability to dissolve TMAF up to high concentrations (~3 m) and its chemical stability in contact with F-ions. An excess of dried 3 Å molecular sieves was added to the solution to trap the water molecules. The molecular sieves were changed every 8 hours for a total of 24 hours of drying via molecular sieves.

3. The solution was then filtered using 0.1 μm dry PTFE filters to remove any residues left by the molecular sieves and the IPA was evaporated under vacuum using a Rotovap.
4. The TMAF was further dried under vacuum at 90°C for 48 hours to remove any traces of IPA.

The TMAF and IPA solutions were never exposed to air and any container was dried prior to use.

2.2.6 Synthesis of tetramethylammonium fluoride

The precursors TMATFB and KF were dried at 200°C in a dynamic vacuum overnight. This temperature is well below the melting point of both compounds (418°C for TMATFB and 858°C for KF). Anhydrous methanol was purchased and further dried in 3 Å molecular sieves until the water content was below 10 ppm. Only dried plastic containers were used to avoid possible side reactions with glass. All the synthesis steps were carried out in an inert atmosphere and the containers were sealed when they had to be taken out of the glovebox (to avoid any exposure to air and the consequent water adsorption).

1. 0.1 mmol of TMATFB (16.1 g) were added to a stirring solution of 0.12 mmol (7.0 g) of KF in 70 ml of methanol. The solution was left stirring for 3 hours. During this time, KBF_4 formed and precipitated out while the TMAF remained dissolved in the methanol.
2. The solution, including the precipitate, was transferred to a dry centrifuge tube and centrifuged at 7000 rpm for 5 minutes. The supernatant consisting of TMAF dissolved in MeOH was then extracted and filtered using 0.1 μm PTFE syringe filters to remove any residues of KBF_4. About a third of the methanol volume was evaporated on a Schlenk line under vacuum.

3. 60 ml of anhydrous diethyl ether ($H_2O \leq 15$ ppm) were then added, and the solution was stirred for another hour, in order to precipitate out any traces left of KBF_4. The solution was filtered again, and the solvents were evaporated under vacuum to leave behind a white low-melting solid consisting of $Me_4N^+F^- \bullet$ nMeOH.
4. The solid was pulverized and dried in a dynamic vacuum at 90°C for 6 days.

2.2.7 Washing procedures for 1,3-dimethylimidazolium bis(trifluoromethanesulfonyl)imide

In Chapter 5, DMIM TFSI was washed to remove an acidic impurity. Different procedures were trialled in an attempt to completely eliminate this impurity.

(1) DMIM TFSI was mixed with an equal volume of 1% aqueous solution of Na_2CO_3 and vigorously stirred for 4 hours. Thanks to the immiscibility of water and DMIM TFSI, the ionic liquid was separated and dried under vacuum at 80°C.

(2) A more aggressive washing procedure was used to reduce the impurity further. The concentration of Na_2CO_3 was increased to 3% and an ultra-sonication probe was used to stir energetically the aqueous solution with the ionic liquid forcing the two phases to make contact with each other. The ionic liquid was then separated and mixed again with a fresh solution of Na_2CO_3. The process was repeated three times. The outcome of this washing procedure is discussed at the end of Chapter 5.

(3) With the aim of reducing the impurity even further, a third washing procedure using a column was tested. The rationale behind choosing a column was that the fast flowing of the ionic liquid through the Na_2CO_3 would prevent the impurity from reaching a chemical equilibrium with the base. However, no improvement was observed with respect to the ultra-sonication procedure.

2.3 Materials Characterisation

2.3.1 Nuclear magnetic resonance

Nuclear magnetic resonance (NMR) is a spectroscopic technique used to detect the local magnetic fields around atomic nuclei. NMR allows to determine the content and purity of a sample, as well as its molecular structure among other things.

When an electric charge rotates, it generates a magnetic field with a magnetic moment (μ) that is proportional to its spin. In the absence of an external magnetic field, the spin direction is random. However, once an external magnetic field (B_0) is applied, it causes the spin to become aligned with it and orient itself either parallel or antiparallel to the external magnetic field. By applying an electromagnetic radiation at the appropriate frequency, the nuclei can absorb this energy, causing the aligned spins parallel to B_0 to flip and become antiparallel, resulting in a higher energy state. This phenomenon is known as resonance, where the nuclei are in resonance with the magnetic field. The energy difference between these two states is directly related to the strength of the external magnetic field and is zero in the absence of any magnetic field. As the strength of B_0 increases, the energy difference between the two states also increases, as described by eq. (2.1).

$$\Delta E = \frac{h \mu B_x}{2\pi I} \tag{2.1}$$

Where h is Plank's constant, μ is the magnetic moment of the nucleus in the field, B_x is the applied magnetic field and I is the nuclei spin.

The reason why NMR can differentiate between different elements and isotopes is that each one absorbs energy at a very specific frequency. Additionally, each type of nuclei will have some variation in the frequency absorbed depending on its surrounding environment.

Neighbouring electrons produce an additional magnetic field which affects the one experienced by the nuclei. This is called nuclear shielding and in most cases its effect is lowering the magnetic field at the nucleus. The difference in the environment (and magnetic field) of the same nucleus is called chemical shift and allows to distinguish between different structures.[48]

Chemical shift is not the only valuable information encoded in an NMR spectrum. Magnetic interaction between nuclei, known as spin-spin coupling or J-coupling, also offers important information. Nuclear spin-spin coupling causes NMR lines to split into multiple peaks with characteristic intensities and spacings. The origin of this phenomenon is the local magnetic field of nuclei that affect the energy of neighbouring nuclei.[48]

In an NMR experiment, the sample is placed in an NMR probe and located in the centre of the magnetic field where the field is at its strongest and the most homogenous. The NMR probe is fitted with radiofrequency coils used to excite the sample. The frequency of the excited nucleus spins can be measured from the electric current that they induce in the coil. Fourier transform converts the signal from time to frequency domain, generating the NMR spectrum.[48]

In this work, an Oxford Instrument X-Pulse benchtop NMR spectrometer in an Ar-filled glovebox was used for routine NMR measurements. A 2-channel Bruker AVIIIHD 400 Nanobay instrument featuring a 5 mm z-gradient BBFO probe (multinuclear with ^{19}F) and a 16-position SampleExpress Lite robotic sample changer was used instead when high resolution was required (e.g., to quantify the amount of HF_2^- in Chapter 5).

In Chapter 4 and 5, NMR was used to measure the solubility of the fluoride salt in the different solvents and assess the chemical stability of the electrolytes.

The maximum concentration of fluoride salt was calculated using ^{1}H NMR, as follows. Oversaturated salt was added to the solvent and left stirring for several hours. The electrolyte was then filtered to remove the undissolved salt and transferred to NMR tubes. From the integration of the peaks and the known number of protons responsible for those peaks, it was possible to calculate the maximum concentration of salt in a given solvent. The maximum concentration is always measured as ~24°C. Fluorinated ethylene propylene (FEP) NMR liners were always used to prevent the electrolytes to make contact with the glass of the NMR tubes.

2.3.2 Pulsed field gradient nuclear magnetic resonance

Pulsed field gradient (PFG) NMR is a non-invasive technique used to study molecular motion. In (PFG) NMR, a pulse gradient is applied creating a phase shift, which depends on the spatial position of the spins. To cancel the effect of this phase shift, an opposite gradient pulse having the same signal intensity and duration is applied to return all the spins in-phase. However, this only happens if the spins spatial position has not changed in the time between the two gradient pulses. When molecules diffuse between the two pulses a partial phase shift will remain, decreasing the intensity of the NMR signal. This loss in NMR signal depends on the intensity and duration of the gradient pulse. The intensity of the NMR signal is given by Stejskal-Tanner equation.

$$S = S_0 e^{-(\gamma g \delta)^2 \Delta D} \tag{2.2}$$

where Δ is the diffusion time, D is the diffusion coefficient, g and δ determine the gradient pulse area, γ is the magnetogyric ratio. Since Δ, g and δ are fixed and S and S_0 are measured, the diffusion coefficient can be calculated. To do so, the intensity of the pulsed field gradient is varied in discrete steps so that the experimental data is fitted according to eq. (2.2).[49]

In Chapter 4 and 5, PFG NMR was used to measure the diffusion coefficient of the different ions in the electrolyte. These experiments were carried out by Dr Gregory Rees and the following parameters were used.

The diffusion coefficients were measured at 30°C using pulsed field gradient (PFG) NMR, with measurements completed at 9.45 T (υ_0 (^{19}F) = 376.51) on Bruker Avance III HD spectrometer using a 5 mm single-axis diffusion probe with exchangeable ceramic heads. A stimulated echo pulse sequence was utilized for all PFG experiments with effective gradient pulse durations (δ) ranging between 1 to 1.5 ms, and a diffusion time (Δ) of 10-30 ms, with the gradient amplitude varying between 0.1 and 24 T/m in 36 steps. All samples were sealed in a J-Young air-tight NMR tube, temperature stabilized to 303.1 K, and a 1-second recycle delay was used throughout. All data was fitted to the Stejskal-Tanner equation (eq. 2.2). An R^2 value of 0.999, errors of < 1% and normal distribution of the residuals (> 0.5 Shapiro Wilko score) were observed for all experiments.

2.3.3 Dynamic light scattering

Dynamic light scattering (DLS) is a non-invasive technique used to measure the size and size distribution of sub-micron particles dispersed in a solvent.

In DLS, a monochromatic laser hits the sample and gets scattered due to the Brownian motion of the particles. The scattered light is then recorded for a certain period of time to monitor the movement of the particles. The intensity of the scattered light fluctuates over time, with smaller particles showing more rapid fluctuations whereas larger particles exhibiting fluctuations with larger amplitudes. By analysing these fluctuations, it is possible to obtain the velocity of the Brownian motion and the particles size thanks to the Stokes-Einstein equation which links the two.

$$D = \frac{k_B T}{6\pi\eta R_H} \quad (2.3)$$

Where D is the translational diffusion coefficient ($m^2\ s^{-1}$) (speed of particles), k_B is Boltzmann constant, T is temperature, η is the viscosity and R_H is the hydrodynamic radius of the particles.

The upper limit in particle size measurable by DLS is determined by the onset of particle sedimentation, as to obtain accurate and meaningful results the particles must be moving purely due to Brownian motion. The lower limit in particle size is determined by the signal-to-noise ratio, as small particles do not scatter enough to be detected by the instrument.[50]

In this work a Partica LA-960V2 Horiba DLS analyser was used. The DLS samples were prepared by dispersing 10 mg of powder in 10 ml of ethanol. The dispersion was stirred right before the measurement with an ultra-sonication probe for 2.5 minutes to break the aggregates. The dispersion was then added to the main tank of the DLS where the analysis takes place.

In Chapter 3, DLS is used to measure the particle size of PbF_2 and Pb at different stages during the manufacturing procedure.

In chapter 5, DLS is used to measure the particle size of BiF_3 powders after ball milling.

2.3.4 Karl Fischer coulometric titration

Karl Fisher (KF) coulometric titration is one of the most accurate methods to measure water content. It is based on a modified Bunsen Reaction between iodine and an excess of sulphur dioxide in a non-aqueous medium. An alcohol is used as the main solvent and a base as the buffering agent. Originally, methanol and pyridine were used but they have both been replaced with less toxic compounds. Glycol monoethyl ether and imidazole are frequently used.

The alcohol (ROH) reacts with the sulphur dioxide and base (R'N) to form an intermediate alkylsulfite salt, which is then oxidised by iodine to form an alkylsulfate salt.

$$ROH + SO_2 + R'N \rightarrow [R'NH]SO_3R + H_2O + I_2 + 2R'N \rightarrow 2[R'NH]I + [R'NH]SO_4R \quad (2.4)$$

The oxidation reaction consumes water and iodine in a ratio 1:1. When all the water has been consumed, the excess of iodine is detected and triggers the end of the reaction.

The instrument used in this work was a Mettler Toledo C30S Coulometric Karl Fisher Titrator placed in an Ar-filled glovebox.

In Chapter 4 and 5, KF was used to measure the water content of TMAF as well as the solvents used to produce the electrolytes. To measure the water content of TMAF powder, it was dissolved at a known concentration in anhydrous isopropanol. The water content of the pure isopropanol was then subtracted from the water content obtained for the TMAF-IPA solution.

2.3.5 X-ray diffraction

X-ray diffraction (XRD) is a technique used to analyse the crystal structure of materials. It works by shining a coherent X-ray radiation onto the sample. After interacting with the atoms, the scattered radiation can conserve its initial energy through elastic scattering. Depending on the scattering angle the radiation can interact in a constructive or destructive manner. The constructive interference is described by Bragg's law (eq. 2.5).

$$n\lambda = 2\,d\sin(\theta) \quad (2.5)$$

Where n is an integer number (generally 1), λ is the wavelength of the radiation comparable to the atomic spacing, d is the distance between two lattice planes and θ is the glancing angle between the incident radiation and the lattice plane. The effect of constructive and destructive interference intensifies due to the cumulative effect of successive crystallographic planes of

the lattice. By varying the glancing angle, it is possible to obtain a diffractogram that illustrates the intensity of the diffracted radiation with respect of the angle (stated as 2θ). Peaks are visible at the angle where Bragg's relationship is satisfied, and planes separated by a distance d exist. The crystal structure of crystalline materials is therefore possible to be determined using XRD.[51]

In this work, a Rigaku Miniflex 600 with a monochromatic Cu Kα radiation source inside a N_2-filled glovebox was used. Low background Si sample holders were used. Samples were transferred to the XRD glovebox in sealed vials and were never exposed to air.

In Chapter 3, XRD was used to verify the success of the Pb and PbF_2 synthesis.

In Chapter 4, XRD was used to check the purity of the synthesised TMAF.

In Chapter 4 and 5, XRD was used to confirm the conversion of the electrodes cycled in the new electrolytes proposed.

2.3.6 Fourier-transform infrared spectroscopy

Fourier transform infrared spectroscopy (FTIR) is a spectroscopy technique used to identify the chemical composition of materials. Infrared radiation is absorbed by molecules causing them to vibrate. Different chemical bonds vibrate at specific frequencies which can be detected and analysed using FTIR.

At the core of a FTIR spectrometer lays a Michelson interferometer, which splits the incoming infrared beam into two optical beams. One is directed to a fixed mirror, while the other to a movable mirror. Once reflected back to the beam splitter in the interferometer, the two beams are recombined, causing interference, and directed to the sample. The use of a Michelson interferometer allows to acquire spectral information at all wavelengths simultaneously, leading to fast acquisition times. After the beam is transmitted through the sample into the detector, a signal of light intensity versus mirror position is produced. The use

of a Fourier-transform allows to convert the mirror position into wavenumber. The subtraction of a background spectrum (recorder without a sample) from the sample spectrum allows to obtain the FTIR spectrum of transmission as a function of wavelength.[52]

In Chapter 3, a Thermo-Fischer Nicolet iS50 situated in a nitrogen-filled glovebox was used to establish the purity of the synthesised TMAF powder. Transmission mode was used. This experiment was run by Maximilian Schart.

2.3.7 Inductively coupled plasma optical emission spectroscopy

Inductively coupled plasma optical emission spectroscopy (ICP-OES) is an analytical technique used to measure trace amounts of chemical elements in solution.

ICP-OES operates by detecting the wavelength of light emitted by the ions in a plasma. To do so, the liquid sample is drawn into the instrument by a peristatic pump which feeds it into the nebuliser. In here, the liquid is converted into a fine aerosol spray. In the spray chamber, larger droplets are drained away, whereas finer droplets are directed into an argon plasma (7000-10000°C). In the plasma, the droplets are atomised, and the elements contained within are excited to a higher state. When they go back to the lower energy state, they emit light which is characteristic of a specific element. The light is transferred into a high-resolution optical system which separates the light into specific wavelengths. The intensity of each wavelength is quantified allowing to identify the concentration of each metal ion present in the sample.[53]

In Chapter 4, a Perkin-Elmer Optima 8000 ICP-OES instrument was used to quantify the dissolution of Pb and PbF_2 in methanol and propionitrile. The extent of Pb and PbF_2 dissolution was measured separately in methanol, propionitrile and a 5 wt% MeOH- 95 wt% PN solution. To do so, ~3 mg of Pb or PbF_2 were mixed with ~3 ml of solvent. After 20 hours,

the solutions were centrifuged, and the supernatant filtered with 100-nm PTFE filters. Equal volumes of sample and a Mn (100 ppm) ICP standard solution were mixed and diluted by a factor of 100 to 300 depending on the sample. The dilution was done with a 2% HNO_3 solution in ultrapure water. This experiment was run by Maximilian Schart.

2.4 Microscopy Techniques

2.4.1 Scanning electron microscopy

Scanning electron microscopy (SEM) is a microscopy technique in which the image of the sample is produced by an electron beam. The electron beam is produced inside the instrument by a tungsten filament cathode, a lanthanum hexaboride (LaB_6) wire or a field emission gun. The beam is then accelerated inside the column of the instrument, which is under vacuum, thanks to a potential difference and is then focused on the sample through a series of lenses and apertures. The position of the beam on the sample is controlled by a series of scanning coils positioned on top of the closest lens to the sample (objective lens). The electron beam can penetrate the surface of the sample by a few micrometres depending on the accelerating voltage and the density of the sample. The interaction between the electron beam and the sample produces secondary electrons, and backscattered electrons (BSEs). Back-scattered electrons arise from elastic interactions and are generated from the surface and within the sample. BSEs show great sensitivity to differences in atomic number, which will show as brighter (higher Z) or darker regions (lower Z). Secondary electrons originate from inelastic interactions on the surface of the sample and provide more accurate information on morphology. The electrons are then collected by a detector to generate the image.

X-rays can also be emitted as a consequence of BSEs trapped inside the sample. Energy dispersive X-ray spectroscopy (EDS) allows to collect the emitted X-rays and provide elemental identification.[54]

In Chapter 3, SEM of the Pb-PbF_2 electrode's surface (by Dr Guillaume Matthews) and PbF_2 particles (by Maximilian Schart) was performed in a Zeiss Merlin FEG-SEM at an accelerating voltage of 10 kV. In addition, the Pb-PbF_2 electrode was coated with 4 nm of platinum using a Leica EM ACE200 coating system, in order to avoid local charging and improve image resolution.

2.4.2 Plasma focused ion beam

Focused ion beam has been increasingly popular for site-specific analysis, deposition, and ablation of materials, thanks to its ability to precisely shape objects on the nanoscale. Focused ion beam uses a similar principle to SEM. However, in this case the electron beam is replaced by an ion beam, generally of Ga^+ ions. In plasma focused ion beam (p-FIB), Xe^+ plasma is used instead of Ga^+ ions to avoid Ga contamination and enable high throughput milling for large volume characterization.[55]

In Chapter 3, the Pb-PbF_2 cross section was prepared with a p-FIB and imaged using SEM. This was done with a Helios G4 PFIB CXE Dual Beam (Thermo Scientific). After depositing a protective layer of organometallic Pt, all milling was done at 30kV and the samples were polished to 60nA to balance time taken and quality of the cross-section. SEM images were taken with 5kV 0.1nA and EDS was run with 5 kV 1.6 nA to obtain a more surface-sensitive signal. This experiments was carried out by Yvonne Chart.

2.5 Electrochemical Characterisation

2.5.1 Galvanostatic cycling

During galvanostatic cycling (GC) a constant current is applied to a cell overtime and the change in potential and capacity are recorded. This technique allows to study the performance and reversibility of the reactions occurring inside the cell. One way to operate GC is to apply a constant current and select a cut-off voltage that defines the operating potential range of the cell. The standard way of reporting GC data is by plotting the voltage (V) as a function of specific capacity (mAh g^{-1} of active material).[56] The shape of the profile relates to the nature of the reaction inside the cell. A flat plateau indicates the coexistence of two different phases, with one progressively replacing the other until the end of the plateau. A multistep profile, instead, denotes the presence of multiple stable phases, one at the end of each plateau.

The efficiency of a charge/discharge cycle, known as coulombic efficiency, is given by eq. (2.6).

$$\eta_C = \frac{Q_{discharge}}{Q_{charge}} \tag{2.6}$$

where $Q_{discharge}$ and Q_{charge} are the capacities obtained on discharge and charge, respectively.

The intensity of the current applied during cycling may have an impact on the achievable capacity as reactions with slow kinetics may require longer times to complete. The value of the current is often reported as current rate (C-rate) which represents the amount of current required to achieve full charge or discharge of the cell in a given time. 1C means that the amount of current required to charge/discharge the cell in 1 hour is applied, while C/10 indicates that the cell will charge/discharge in 10 hours.

In this work a Biologic VMP3 potentiostat was used to cycle symmetric and non-symmetric coin cells and to perform all the electrochemical experiments. A cycling rate of C/20 was applied for the cycling of any type of cell.

In Chapter 3, GC experiments were performed in symmetric Pb-PbF_2 coin cells. The purpose was to test the wetting capability of the different types of separators via a comparison of the overpotential. Additionally, GC was used to test the performance of the Pb-PbF_2 electrodes.

In Chapter 4, GC was used to test the cycling performance of symmetric Pb-PbF_2 cells in the diluted electrolyte, as well as BiF_3 vs Pb-PbF_2 cells.

In Chapter 5, GC experiments were performed in Pb-PbF_2 symmetric cells to test the performance of the ionic liquid electrolyte.

2.5.2 Potentiostatic electrochemical impedance spectroscopy

Potentiostatic Electrochemical Impedance Spectroscopy (PEIS) is used to measure the internal resistance of a sample, which is given by the ratio between the voltage (E) and the current (I) according to Ohm's law (eq. (2.7)).

$$R = \frac{E}{I} \tag{2.7}$$

In this technique, an AC potential is applied to the cell and its current response is measured. Assuming a sinusoidal behaviour, the potential change is defined by eq. (2.8).

$$E_t = E_0 \sin(\omega t) \tag{2.8}$$

Where E_t is the potential at a given time t, E_0 is the amplitude of the signal and ω is the angular frequency. The current response is also sinusoidal and given by the following relationship:

$$I_t = I_0 \sin(\omega t + \varphi) \tag{2.9}$$

where I_t is the current at time t, I_0 is the amplitude of the current and φ is the phase shift between the current and the potential. The impedance of the system is then calculated with eq. (2.10).

$$Z(\omega) = \frac{E_t}{I_t} \tag{2.10}$$

One way of displaying the impedance results is through a Nyquist plot in which the imaginary contribution of the impedance is plotted with respect to the real impedance (Fig. 2.1). In batteries, it is very complicated to deconvolute the contribution of each component towards the overall impedance result. As an approximation, the first intercept of the semicircle with the x-axis represents the solution resistance (R_S) which is related to the transport properties of the electrolyte. The second intercept arises from a combination of the charge transfer resistance (R_{CT}) and the mass transfer resistance (R_{MT}). They represent the resistance arising from the electrochemical reactions in the electrodes and that from the desolvation of the ions at the electrode-electrolyte interface, respectively.

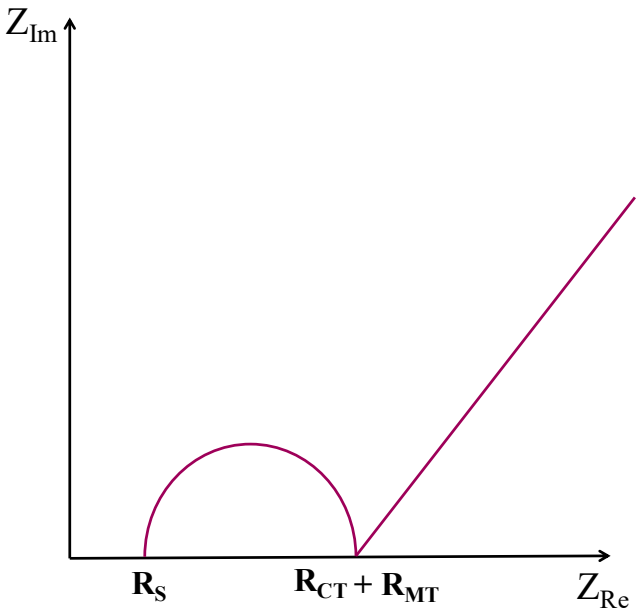


Figure 2.1: Nyquist plot of the imaginary impedance (Z_{Im}) as a function of the real impedance (Z_{Re}) for a standard battery configuration. R_s represents the solution resistance whereas R_{CT} and R_{MT} the charge and mass transfer at the electrodes, respectively.

The Nyquist plot for a cell with ideal blocking electrodes displays a straight vertical line that intercepts the real impedance at R_s, due to the lack of mass and charge transfer (Fig. 2.2-a). The equivalent circuit that describes this scenario is a resistor (solution resistance – R_s) in series with a capacitor (double layer capacitance – C_{DL}). The use of non-ideal blocking electrodes, such as polished metal that have some level of roughness, will result in a Nyquist plot that deviates from the ideal scenario (vertical line tilted by an angle Θ) (Fig. 2.2-b).[57]

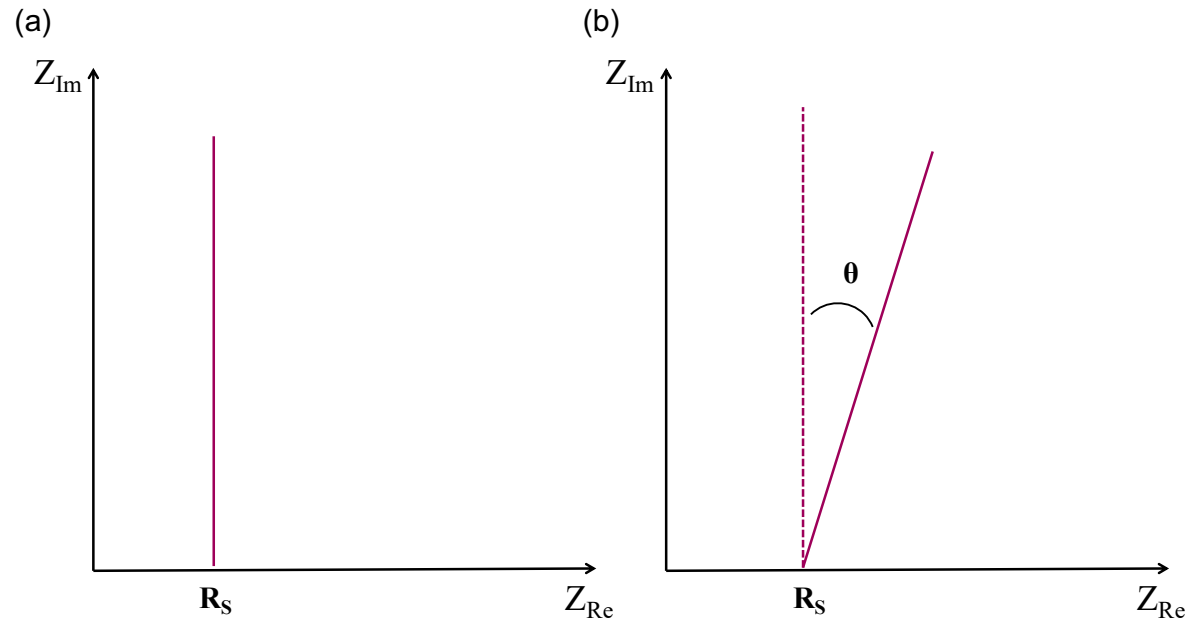


Figure 2.2: Nyquist plot for a cell with blocking electrodes. In this scenario, R_{CT} and R_{MT} are zero. **(a)** A vertical straight line is obtained with ideally flat electrodes. **(b)** With metal non-ideal electrodes, the straight line deviates from ideality by an angle Θ.

In Chapter 4 and 5, PEIS was used to measure the ionic conductivity of the liquid electrolytes. Measurements were acquired between 1 MHz and 100 mHz using a 2-electrode custom-made cell made of stainless steel and polyetheretherketone (PEEK) with a well-defined surface area and distance between the blocking electrodes. R_S was extracted from the Nyquist plot using a linear fit and used to calculate the ionic conductivity with eq. 2.11.

$$R_S = \frac{d}{I_C\, A} \tag{2.11}$$

Where d is the distance between the electrodes, A is the surface area of the electrode and I_C is the ionic conductivity.

The cells were rested for 30 minutes before the PEIS measurement to ensure they had reached the set temperature of 30°C. Fig. 2.3 demonstrates that 30 minutes were a long enough time as the resistance did not change after this period.

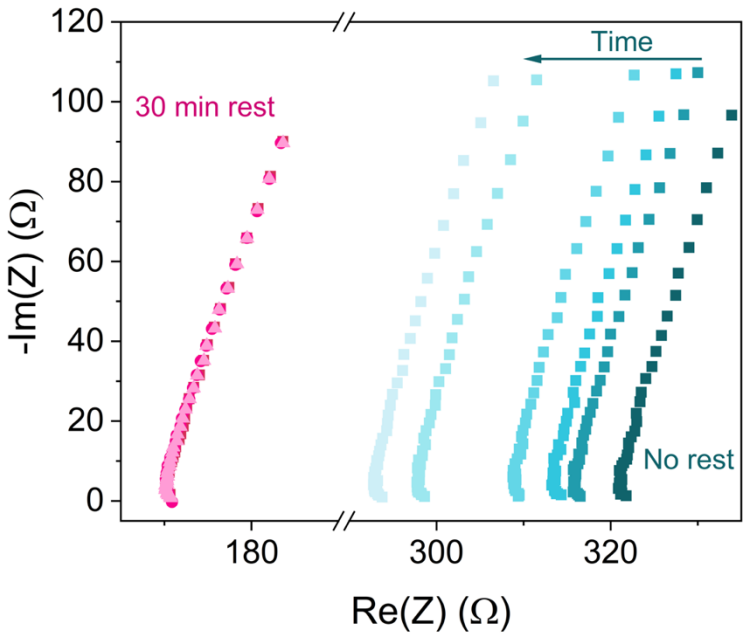


Figure 2.3: Resistance decreases with passing of time as the electrolyte progressively heats up to reach 30°C (blue). Resistance does not change after the cell was rested for 30 minutes as the electrolyte has stabilised at 30°C (red to pink).

2.5.3 Linear scanning voltammetry

Linear scanning voltammetry (LSV) is a commonly used technique to measure the electrochemical stability window of electrolytes. It works by varying the applied voltage within a defined range while recording the current output. The potential range in which the current is almost constant and zero represents the potential window in which the electrolyte is stable. The potential at which the current starts to increase (or decrease in the case of the reduction scan) exponentially defines the limit of the electrochemical stability window of the electrolyte. Often the current density, which is calculated by dividing the current by the surface area of the working electrode, instead of the current, is plotted against the applied voltage.[58] Different methods exist to determine the limit of the ESW. In this work 100 μA cm^{-2} was chosen as the current cut-off, unless stated otherwise.

In Chapter 4 and 5, LSV was used to measure the electrochemical stability window of the synthesised electrolytes. A 3-mm diameter glassy carbon working electrode, platinum wire

counter electrode and a Pb-PbF_2 counter-reference electrode were used. A scanning rate of 1 mV s^{-1} was used.

2.6 Monte Carlo Simulations

Monte Carlo simulations were used to predict how the solvation structure of F-ions changed between the highly concentrated electrolyte and the diluted liquid electrolyte of Chapter 4. The simulations were performed using the Empirical Potential Structure Refinement software (version 26.1) and visualised using the Aten packages.[59,60]

The cubic simulation box of sides 43.12 Å contains 200 TMAF molecules and 624 methanol molecules to reproduce the experimental concentration of 10 molal (1:3.12 TMAF:MeOH molecular ratio) with atomic number density of 0.0916 atoms $\dot{A}^{-3}$. When propionitrile (PN) is added to make a 0.5 molal TMAF:MeOH:PN ternary mixture, the cubic simulation box of sides 76.11 Å contains 100 TMAF, 312 methanol and 3450 propionitrile molecules to match the experimental density of 0.7885 g cm^{-3}, measured using a Anton Paar DMA 4100 density meter in an argon-filled glovebox at 30°C (<0.1 ppm O_2 and H_2O).

The force field used are the OPLS-AA for methanol, fluoride anions, TMA cations and propionitrile with a potential cut-off of 18 Å.[61–63] Lennard-Jones potentials and charges are presented in Table 2.1. The depth of the Lennard-Jones potential well for F^- is larger compared to that of the other atoms because it reproduces the Harthree Fock interactions energies for ion-water complexes. However, the ion-molecule potentials are relatively insensitive to the precise values of the Lennard Jones parameters since the energies are dominated by the coulombic term.[64]

All molecules were built in Avogadro and the geometries were optimised using the MMFF94 force field for 1000 steps.[65,66]

The simulations reached energy equilibration after 1,000 iterations, and a number of 10,000 configurations were accumulated in a trajectory file to extract the structural information of the two systems.

Table 2.1: Lennard-Jones parameters and charges from the OPLS-AA force field for methanol, tetramethylammonium cation (TMA^+), fluoride anion (F^-) and propionitrile.[61]

		σ /Å	ϵ /kJ mol^{-1}	q /e
MeOH	**O**	3.12	0.71128	-0.683
	$\mathbf{C_M}$	3.5	0.276144	0.145
	H	-	-	0.418
	$\mathbf{H_M}$	2.50	0.12552	0.04
TMA^+	$\mathbf{N_1}$	3.25	0.71128	-
	$\mathbf{C_1}$	3.50	0.29288	0.07
	$\mathbf{H_1}$	2.50	0.12552	0.06
	$\mathbf{F^-}$	2.733	3.01248	-1.0
Propionitrile	$\mathbf{C_{1p}}$	3.30	0.27614	0.46
	$\mathbf{C_{2p}}$	3.30	0.27614	-0.02
	$\mathbf{C_{3p}}$	3.50	0.12552	-0.18
	$\mathbf{H_{1p}}$	2.50	0.12552	0.06
	$\mathbf{H_{2p}}$	2.50	0.12552	0.06
	$\mathbf{N_{1p}}$	3.25	0.12552	0.06

The Monte Carlo simulations were done by Dr Camilla Di Mino and the results are discussed in Chapter 4.

Chapter 3

Inactive Components and Testing Set-Up

Table of Contents

3.1 Introduction 58

3.2 Results and Discussion 60

3.2.1 Active material selection and processing for counter-reference electrodes 60

3.2.2 Choice of a suitable binder 63

3.2.3 Manufacturing process for Pb-PbF_2 counter-reference electrodes 68

3.2.4 Choice of separator 71

3.2.5 Cycling of Pb-PbF_2 counter-reference electrodes in 2-electrode coin cells 76

3.3 Conclusion and Future Work 78

3.1 Introduction

As mentioned in the general introduction, to accelerate the progress of liquid electrolyte FIBs, flooded cells should be replaced by more realistic form-factors, such as coin and pouch cells. Coin cells would avoid the drawbacks of flooded cells; however, their use has been impeded by a few issues. Firstly, coin cells require a reliable counter-reference electrode, equivalent to Li metal in lithium-ion batteries, which is currently not available for FIBs. To achieve this, a suitable binder is needed to replace the commonly used PVDF and prevent chemical degradation. Furthermore, a suitable separator, particularly one that works well with any electrolyte (including ionic liquid-based electrolytes), is also missing.

A suitable counter-reference electrode, binder and separator should satisfy several requirements. The counter-reference electrode should exhibit a stable potential during cycling so that any variations in voltage can be attributed to the working electrode. Additionally, it should provide a readily accessible reservoir of F-ions to compensate for irreversible losses. These losses can be caused by the formation of solid electrolyte interphases or the decomposition of the electrolyte. Finally, the counter-reference electrode should exhibit

(electro)chemical stability towards F-ions in the electrolyte. The ideal binder should exhibit excellent chemical stability with F-ions, good thermal stability, strong adhesion (to the current collector, as well as the active material and carbon), and a large electrochemical stability window. Additionally, it should possess the ability to form a flexible and robust network capable of accommodating the volume changes of the active material during cycling to prevent electrode pulverization. Finally, the ideal binder should be able to dissolve in a solvent with desirable properties (e.g., high boiling point and viscosity). Lastly, the separator should be (electro)chemically compatible with the electrolyte, and wet well to minimise the cell internal resistance and the overpotential during cycling.

In this chapter I report a novel method to produce reliable and chemically stable Pb-PbF_2 electrodes, featuring a dry-process in the presence of a polytetrafluoroethylene (PTFE) binder. Additionally, I introduce a PTFE-based separator capable of wetting, even with ionic liquid-based electrolytes, while exhibiting electrochemical stability within the electrochemical stability window of the electrolyte.

All the work in this chapter was performed by me under the supervision of Prof. Mauro Pasta. Exceptions are the electrode cross section and corresponding EDS spectra done by Yvonne Chart using focused-ion beam scanning electron microscopy. Additionally, the SEM image of PbF_2 powder was taken by Maximilian Schart, whereas the one of the electrode surface was taken by Dr Guillaume Matthews. Some of the results in this chapter are part of the work that is under review in *ACS Energy Letters* authored by Giulia Galatolo, Omar Alshangiti, Dr Camilla Di Mino, Dr Guillaume Matthews, Dr Albert Xiao, Dr Gregory Rees, Maximilian Schart, Yvonne Chart and Prof. Mauro Pasta.

3.2 Results and Discussion

3.2.1 Active material selection and processing for counter-reference electrodes

The first step in developing a suitable counter-reference electrode is selecting the active material. In this work, Pb and PbF_2 were chosen because of their several advantages, which have already led to their investigation as potential working electrodes for FIBs. The low melting point of Pb (327.5°C), which facilitates metal crystallization, and the high ionic conductivity of PbF_2 at room temperature (10^{-7} – 10^{-9} S cm^{-1}) compared to other fluorides enable excellent conversion yields.[24,46,67] Additionally, the redox potential of PbF_2/Pb allows cycling in most FIBs electrolytes. Despite all these advantages, the Pb-PbF_2 electrodes reported in the FIB literature thus far have exhibited poor cycling performance in liquid electrolytes.[28,44,68] This might be linked to the limited emphasis on their microstructural design.

A uniform and well dispersed mixture of Pb and PbF_2 is required to achieve a stable electrode potential, reduce the overpotential during cycling and provide a reservoir of F-ions.[24] Furthermore, small sized particles and high ionic conductivity are fundamental to achieve full conversion during cycling. Kawasaki et al. have shown that Pb and PbF_2 particles no larger than 3 μm should be employed, to limit the diffusion distance of F-ions and ensure full conversion within reasonable amounts of time.[46]

To accomplish this reduction in particle size and increase ionic conductivity, PbF_2 was ball milled until the average particle size was reduced from ~6 μm to ~500 nm (details of the ball milling procedure are in Chapter 2) (Fig. 3.1-a). Ball-milled PbF_2 was further processed to convert the orthorhombic α-crystal structure (10^{-8} – 10^{-9} S cm^{-1} at RT) into the more ionically conductive cubic β-structure (10^{-7} – 10^{-8} S cm^{-1} at RT), via heat treatment (HT) (Fig. 3.1-b).[67] To achieve this the PbF_2 powder was heated at 350°C—above the α-β transition temperature—

for 90 minutes in an inert atmosphere. The successful conversion to the cubic structure is demonstrated in Fig. 3.1-b by XRD. The average particle size increase during heat treatment due to particle sintering (from ~500 nm to ~1.5 µm) (Fig. 3.1-a,c,d) is more than compensated by the one order of magnitude increase in ionic conductivity.[67] Unfortunately, the order of the ball milling and annealing steps cannot be reversed, since the pressure exerted on the particles during ball milling converts the β-phase back to the α-structure (Figure 3.1-b). The orthorhombic phase is, in fact, the only PbF_2 crystal structure that is stable at high pressures.[67]

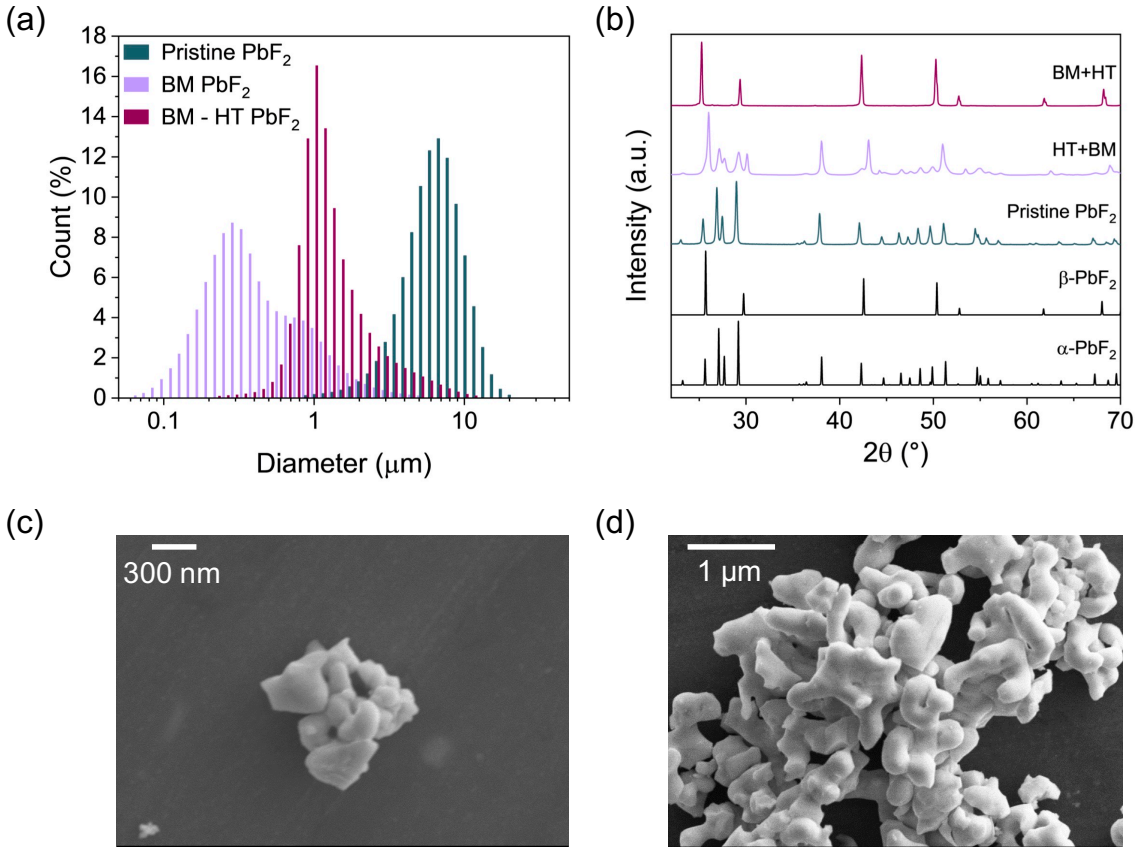


Figure 3.1: Preparation of PbF_2. **(a)** Particle size distribution showing a decrease in the average particle size after ball milling (BM), and a subsequent increase after heat treatment (HT). **(b)** XRD displaying a full conversion to β-phase after ball-milled PbF_2 is heat treated (BM+HT). However, if the ball milling is done after the heat treatment the α-phase reappears (HT+BM). SEM of **(c)** ball milled PbF_2 and **(d)** ball milled and heat treated PbF_2 showing a particle size increase compared to (c) due to particle sintering.

The particle size of Pb also needed to be minimised, since Pb converts to PbF_2 during cycling. The minimum particle size of commercially available Pb powder is ~45 µm, which

unfortunately cannot be reduced by ball milling due to the ductility of Pb. Here, thermal decomposition of lead acetate ($Pb(C_2H_3O_2)_2$) was used to achieve Pb particles with an average size of 2 μm (Fig. 3.2-a,b). Lead acetate was heated at 500°C for 27 minutes in an inert atmosphere.[69] The time is crucial as 500°C is above the melting point of Pb (328°C) and a longer exposure to this high temperature would result in larger particles.

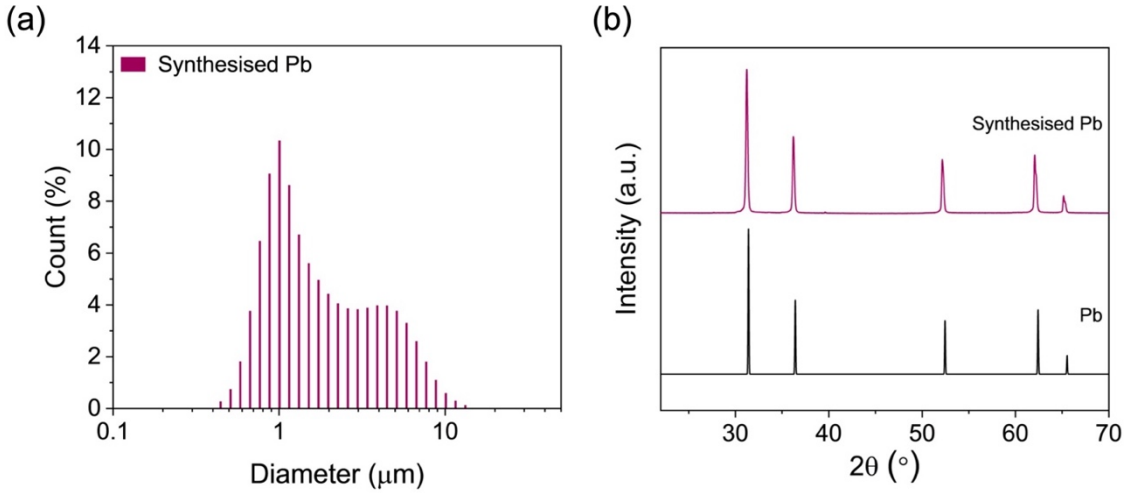


Figure 3.2: Preparation of Pb. **(a)** Particle size distribution of the synthesised Pb, and **(b)** the corresponding XRD proving full conversion to Pb metal.

Using the procedures described above and summarised in Fig. 3.3, Pb and β-PbF_2 powders with no impurities, and an average particle size which allows for full conversion were obtained. With the active material prepared, the next step involved finding an appropriate binder to transform the Pb and PbF_2 powders into the counter-reference electrode.

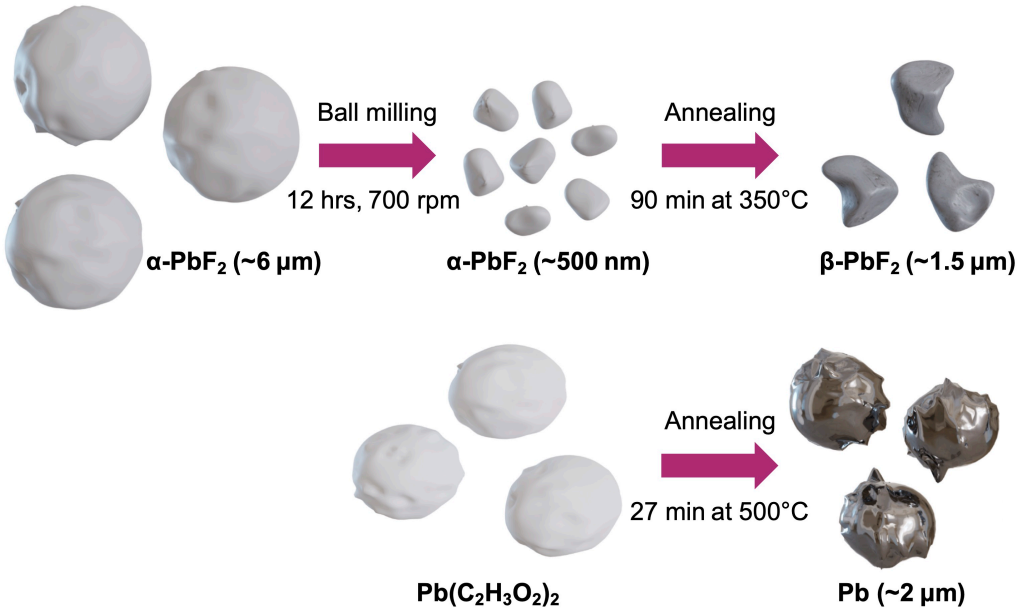


Figure 3.3: Summary of the preparation steps used to achieve β-PbF_2 (top) and Pb (bottom) powders.

3.2.2 Choice of a suitable binder

The binder, typically a polymer, is vital in holding all the electrode components together and ensuring proper contact between them. A lack of contact would lead to the pulverization of the electrode and a decline in performance. To create a conventional electrode, the active material, carbon, and binder are mixed in a solvent to form a slurry, which is then cast on a metal current collector and dried. The solvent used must be able to effectively dissolve the binder to produce satisfactory performance.

Polyvinylidene fluoride (PVDF) is a highly desirable binder in lithium-ion batteries due to its numerous advantages. The solubility of PVDF in N-methylpyrrolidone (NMP), a solvent with a high boiling point (202°C) and viscosity (1.89 mPa·s at 25°C), allows for optimal results. Additionally, PVDF has excellent thermal stability up to 160°C, a low Young's modulus, which offers high flexibility to the electrodes, and a wide electrochemical stability window, ensuring stability at both high and low potentials.[70,71] Another benefit is the ability to uniformly

distribute the carbon additive in the PVDF-NMP mixture, which results in excellent electrical conductivity of the electrodes.

Although PVDF offers numerous advantages as a binder in LIBs and remains the most common choice for FIBs, it should not actually be considered a suitable option for FIB applications due to its vulnerability to chemical degradation when exposed to F-ions. When exposed to strong bases, PVDF undergoes a dehydrofluorination reaction, resulting in the ejection of HF and the creation of C=C bonds or crosslinking between chains. Evidence of this reaction is a colour change towards yellow/brown.[70] Despite the known degradation issue, PVDF remains widely used as the preferred binder in FIBs due to the lack of a viable alternative, since virtually no research has been carried out on this topic so far. The search for a suitable binder for FIBs requires finding a polymer that possesses similar properties to PVDF, but at the same time is chemically stable when in contact with F-ions.

Several polymers were evaluated based on this criterion, and polyethylene (PE) emerged as a possible option. PE exhibits excellent chemical and thermal stability (up to 80°C) and low stiffness. However, the chemical stability also results in poor solubility, making it challenging to find solvents that can dissolve it.[72] In this work, xylene and dichlorobenzene, which are known to attack PE, were tested as possible solvents to dissolve PE.[73] However, both candidates proved to be unsuccessful even at temperatures as high as 100°C, making the manufacturing of electrodes using PE as the binder impossible.

Another possibility considered was polyisobutylene (PIB), which has already been investigated for Li-air and Li-sulphur batteries. PIB is an appealing candidate due to its known chemical and electrochemical stability, as well as solubility in non-polar solvents, like hexane.[74] To test its potential as a binder for FIBs, 1,2-dichlorobenzene (O-DCB) was selected as the solvent due to its higher viscosity and boiling point compared to hexane. A 50 mg ml^{-1}

solution of PIB in O-DCB was used to create a slurry with the active material and carbon, which was then cast onto an aluminium current collector (Fig. 3.4-a). Despite the casting appearing uniform (Fig. 3.4-a), the adherence between the casting and the current collector was weak, making it difficult to handle the electrodes. The casting easily delaminated from the Al foil, and the problem became even more pronounced after several cycles, with significant portions of the electrode separating from the current collector and sticking to the separator (Fig. 3.4-b). The cause of this reduced adhesion could be due to either the electrolyte infiltrating between the casting and Al foil, or the volume changes experienced by the active material. The problem of poor adhesion with PIB has already been observed in Li-sulphur batteries, indicating that it is an inherent problem to the polymer material.[75] In an attempt to mitigate this issue, a carbon-coated Al foil was employed as the current collector to enhance adhesion due to its higher surface porosity. The handling of the electrodes improved in comparison to the uncoated Al foil, however, delamination persisted during cycling, as shown in Fig. 3.4-c. This not only impacts performance, but also impedes post-mortem analysis of the electrodes. Overall, the poor adhesion makes PIB unsuitable as a binder for FIBs.

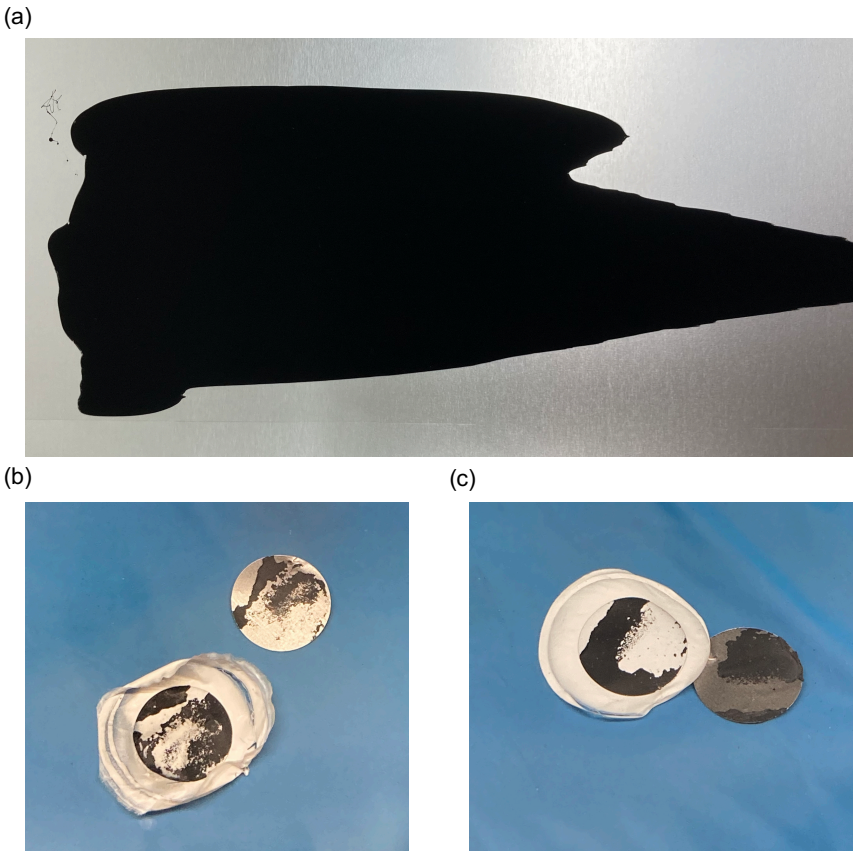


Figure 3.4: Slurry casting with PIB. **(a)** The casting made with PIB binder on an Al current collector looks uniform. **(b)** However, it delaminated after cycling, adhering to the separator. **(c)** The use of a carbon coated Al current collector did not mitigate the delamination issue.

After the failure of both PE and PIB as binders for FIBs, polytetrafluoroethylene (PTFE) was investigated because of its numerous desirable characteristics. PTFE exhibits exceptional chemical stability, making it a prime candidate for use as a binder in FIBs.[76] This same chemical stability, however, results in a lack of solvents able to dissolve PTFE at room temperature, rendering it unsuitable for slurry casting. Fortunately, PTFE fibres have a unique ability to form 3-D networks, called "gabion baskets," which interweave the electrode particles into freestanding films (known as dry casting), overcoming this issue.[77] The use of PTFE as a binder in thin-film solid electrolytes and cathodes in LIBs has proved particularly appealing due to the cost savings achieved through the elimination of solvents. With just 1 wt% or less of PTFE, a 3-D network of fibrils can be formed, effectively holding the electrode components

together and providing adequate mechanical strength.[77] This enables higher active material loading and higher energy densities, potentially surpassing the performance of conventional binders. By employing PTFE as a binder for FIBs, its benefits can be leveraged. While Yamamoto et al. have utilized PTFE in their work on FIBs, they failed to provide an explanation for their rationale for using PTFE, any details of the manufacturing procedure or any characterization of the resulting electrodes.[20,78] This likely explains the limited the adoption in the field of this novel manufacturing method, which was only employed by Kawauchi et al. three years later.[79]

While PTFE offers numerous advantages, producing electrodes with desirable performance through the dry casting method is challenging. The success of the electrodes depends on various factors, with carbon geometry and size being crucial. Flake-like particles found in certain types of carbon black and graphite pose difficulties in reducing the thickness of the casting during dry rolling. These particles tend to stack on each other, resulting in high shear resistance.[80] Additionally, the PTFE fibrils are unable to retain very small particles, causing carbon to leak out of the electrode 3-D structure. Carbon nanofibers (CNFs) or nanotubes (CNTs), however, do not exhibit either of these two problems as they both can interweave with PTFE fibrils and among particles, ensuring good contact. This leads to exceptional electronic conductivity in the dry-processed electrodes and improved structural integrity.[80]

By using PTFE (675-µm particle size) as the binder for FIBs it was possible to overcome the shortcomings encountered with both PE and PIB. In fact, despite not being soluble in any solvent at room temperature, PTFE was still capable of producing electrodes thanks to its ability of forming free-standing films. Additionally, these PTFE free-standing electrodes did not require the use of a current collector, eliminating the delamination problem

observed with PIB. In the case of PTFE-based electrodes, the coin cell case and cap or the spacer were used as the current collectors (Fig. 3.5). Furthermore, the mechanical strength of these free-standing electrodes prevented them from breaking during disassembly, specifically while peeling the separator off, enabling post-mortem analyses (Fig. 3.5).

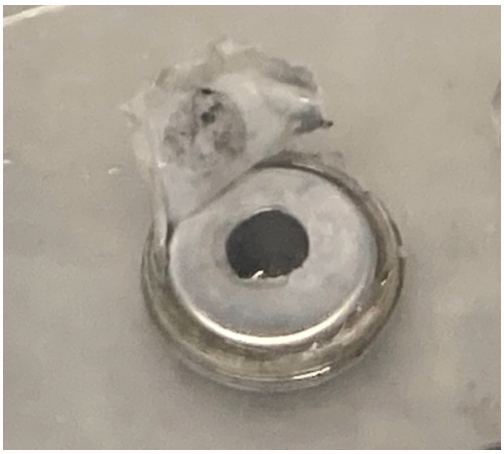


Figure 3.5: Electrodes with a PTFE binder do not have the delamination problem occurring with PIB. They can also hold the active material and carbon together even though PTFE cannot be dissolved in a solvent.

Among the screened polymers, PTFE proved to be the most promising option as a binder for FIBs due to its excellent chemical stability and ability to form flexible free-standing films. Because PTFE was used as the binder, the Pb-PbF_2 counter-reference electrodes were fabricated using dry processing. The manufacturing procedure and the characterisation of the dry-processed electrodes are discussed in the next section.

3.2.3 Manufacturing process for Pb-PbF_2 counter-reference electrodes

A PTFE binder was used for the first time in FIBs in 2019 but has rarely been employed since.[20] This could be partly due to the lack of reporting of any manufacturing details in that study. It is therefore pertinent to describe in detail how, in this work, the Pb-PbF_2 electrodes were manufactured using dry casting and what factors had to be carefully tailored to the mechanical properties of the active material (further details on the ratio of active material, binder and PTFE used are reported in Chapter 2).

The manufacturing procedure used to make free-standing electrodes, including Pb-PbF_2 electrodes, was the following. First, the active material and carbon were mixed well with a mortar and pestle until a uniform colour was reached. The shear force exerted during the mixing had to be adjusted depending on the nature of the active material. For example, Pb is extremely ductile, and an excessive force resulted in the coating of the mortar surface with Pb and the consequent loss of active material from the mixture. On the other hand, more brittle materials (e.g., BiF_3) required a higher shear force to facilitate the breaking of secondary particles. Once the active material was mixed well with the carbon nanofibers, PTFE was added to the mortar and mixed with the other components using a spatula to prevent any pressure from being applied at this stage. Once the PTFE looked uniformly dispersed, pressure was applied with the pestle to initiate the fibrilisation process. After the fibrilisation process had initiated and the 3-D network had started to form, it was no longer possible to easily mix the different components together. This is the reason why it was important to apply pressure only when all the powders were mixed well together, to avoid poorly dispersed regions in the casting. With the formation of the PTFE 3-D structure, the powders started to compact together to form flakes. Eventually, all the flakes merged to form a unique film. The film was then inserted between two stainless steel sheets for the calendaring step. Stainless steel was used instead of aluminium as the higher stiffness prevented the sheets from warping and damaging the casting. The high and uniform pressure applied by the rolling machine allowed to increase the mechanical strength of the film by continuing the fibrilisation process as well as tune the thickness of the freestanding casting. Once the casting was ready, 5-mm diameter discs were punched out to create the electrodes (Fig. 3.6).



Figure 3.6: Pb-PbF_2 electrodes made via dry casting with the PTFE binder.

SEM images of the Pb-PbF_2 electrodes indicate the success of the manufacturing procedure, including the formation of binder fibrils and the uniform distribution of the materials. An SEM image of the electrode's surface confirms the formation of PTFE fibrils (blue arrows in Fig. 3.7-a), which are embedded together with carbon nanofibres (red arrows in Fig. 3.7-a) in the Pb-PbF_2 matrix. The cross section of Pb-PbF_2 electrodes obtained with focused-ion beam scanning electron microscopy (FIB-SEM) coupled with energy dispersive X-ray spectroscopy (EDS) (Fig. 3.7-b,c) demonstrate the uniform distribution of Pb, PbF_2 and carbon. PbF_2 particles have an elipsoidal shape whereas Pb particles appear very elongated as a result of the pressure applied during the dry processing and the high ductility of Pb. The morphology of Pb appears to be responsible for the electrode's low porosity. This might prevent viscous electrolytes from infiltrating across the entire thickness of the electrode resulting in lower capacities during cycling. Despite this limitation, both Pb and PbF_2 are well dispersed in the carbon matrix. With the electrodes ready, the separator is the only missing element to test the performance of the Pb-PbF_2 electrodes in 2-electrode coin cells.

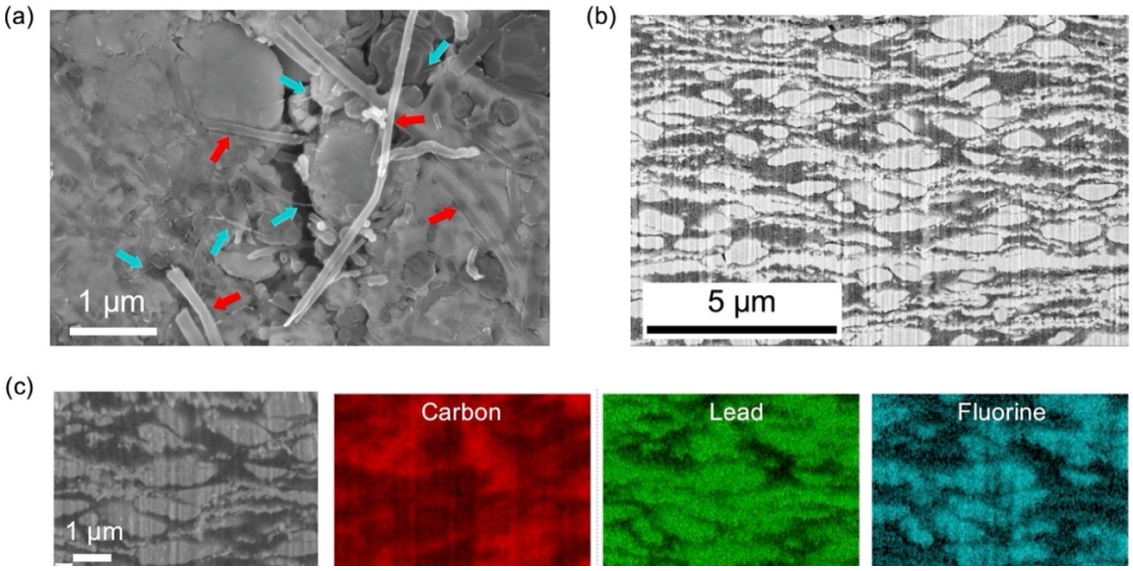


Figure 3.7: Morphology of the Pb-PbF_2 electrodes made with PTFE. **(a)** SEM image of the top surface of a Pb-PbF_2 electrode, with red arrows pointing to the carbon nanofibers while the blue arrows indicate the PTFE fibrils. **(b)** FIB-SEM cross section, and **(c)** EDS mapping showing how the distribution of Pb, PbF_2 and carbon is uniform across the thickness of the Pb-PbF_2 electrode.

3.2.4 Choice of separator

The separator in a battery serves a double function—it prevents physical contact between the electrodes, avoiding short circuits, while allowing the free movement of ions.[81] To fulfil these requirements, separators are constructed from porous and electrically insulating materials.

Several separator materials are available for LIBs, each having its own advantages and drawbacks. Polyolefin separators, such as polyethylene and polypropylene, are commonly used due to their low thickness and cost. However, they have some disadvantages including poor electrolyte wettability, which may increase the internal resistance of the battery, low thermal stability, and limited mechanical strength.[81] The poor wettability is particularly problematic with more viscous electrolytes, such as ionic liquid electrolytes. To address these limitations, various surface coatings have been investigated in the literature, including nitrides, oxides, and carbons, to enhance the wettability, thermal stability, and mechanical strength of polyolefin

separators. A different solution to ensure good wetting is to use glass fibre (GF) as a separator material. GF membranes have gained attention due to their improved wettability, owing to their well interconnected microporous structure, and superior thermal stability compared to PE or PP separators.[81]

Despite exhibiting several advantages, polyolefin and glass fibre separators are not well suited for FIBs. The most problematic of the two alternatives is glass fibre. While borosilicate glass is resistant to attack from F-ions, it is easily etched by HF.[82] Due to the possibility of trace amounts of HF being present in liquid electrolytes, GF separators are not a good option for FIBs. Polyolefin separators, on the other hand, are chemically stable towards F-ions or HF, and could therefore be used with low-viscosity electrolytes in FIBs. However, they are not suitable for more viscous electrolytes, such as ionic liquid electrolytes, and an alternative must be sought.[83]

As was the case of the binder, different materials were investigated as possible separators for FIBs. PTFE was examined because of the same advantages that made it the right candidate for the binder, particularly the excellent chemical and thermal stability. However, the drawback of using PTFE as the separator is its non-polar nature which prevents good electrolyte wetting, similarly to PE or PP. Optimising a surface coating to improve the wettability of PTFE is challenging and beyond the scope of this project. Fortunately, surface-coated hydrophilic PTFE is already used as a filtering membrane and is therefore commercially available. The hydrophilic coating enhances wetting with polar solvents (e.g., water). Among the different types of hydrophilic PTFE membranes available from Millipore, the one with the smallest pore size (0.1 μm) was chosen to minimise the chances of short circuiting. Although the exact composition of the hydrophilic coating is not disclosed, the manufacturer claims the

compatibility of hydrophilic PTFE membranes with virtually all solvents, acids, and alkaline solutions.

To test its suitability as a separator for FIBs, the degree of wetting of the hydrophilic PTFE membrane was tested and compared against a hydrophobic PTFE separator and a polyolefin separator (surfactant-coated polypropylene - Celgard 3501). The degree of wetting was assessed by a rough comparison of the contact angle of electrolyte's droplets on the separator surface and most importantly by the overpotential during cycling. Two different electrolytes were used for the assessment, a low viscosity organic electrolyte (described in Chapter 4) and a more viscous ionic liquid-based electrolyte (presented in Chapter 5). The cycling overpotential was measured using Pb-PbF_2 symmetric cells.

Both the hydrophilic PTFE separator and the polyolefin separator wet instantly upon the addition of the low viscosity organic electrolyte, resulting in a contact angle of ~0° (Fig. 3.8-a). The same behaviour was not observed for the hydrophobic PTFE separator, on which the low viscosity organic electrolyte formed droplets (Fig. 3.8-a). This trend in wetting was matched by the cycling overpotential. The hydrophilic PTFE separator and the polyolefin separator both displayed a low overpotential of 55 and 70 mV, respectively. However, the overpotential almost quadrupled when the hydrophobic PTFE separator was used (~200 mV) (Fig. 3.8-b). These results indicate that the hydrophobic PTFE separator is not suitable even for low viscosity electrolytes, whereas hydrophilic PTFE and polyolefin separators perform equally well with this electrolyte.

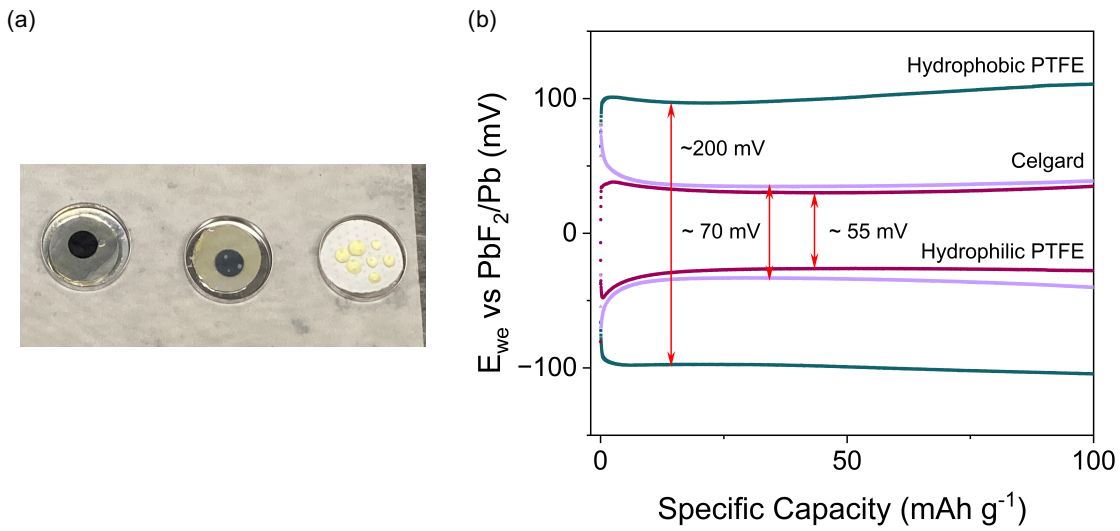


Figure 3.8: Separators wetting with a low-viscosity organic electrolyte. **(a)** Hydrophilic PTFE (left) and polyolefin (centre) wetted instantaneously, whereas droplets of electrolyte formed on the surface of the hydrophobic PTFE (right). **(b)** Overpotential of different separators in a Pb-PbF_2 symmetric coin cell. Hydrophilic PTFE displayed the lowest overpotential (~55 mV), followed closely by the polyolefin (~70 mV). The hydrophobic PTFE separator exhibited the highest overpotential of ~200 mV.

The same separators were then tested with an ionic liquid-based electrolyte. In this case, the hydrophilic PTFE was the only material to wet almost as fast as with the low viscosity electrolyte (Fig. 3.9-a). The polyolefin separator, on the other hand, wetted as poorly as the hydrophobic PTFE separator, with droplets exhibiting very large contact angles in both cases (Fig. 3.9-a). This trend was once again matched by the trend in overpotential. The hydrophilic PTFE separator exhibited the lowest value of ~100 mV, whereas the polyolefin and hydrophobic PTFE separators showed virtually no capacity due to the massive overpotential (Fig. 3.9-b). This poor behaviour had already been observed in LIBs with polyolefin separators and some ionic liquid-based electrolytes, which showed no cycling capability.[83] The low capacity observed was attributed to the poor utilisation of the active material resulting from the inadequate distribution of the electrolyte by the separator. These results indicate that hydrophilic PTFE separators are the only compatible material with ionic liquid-based electrolytes among the three tested.

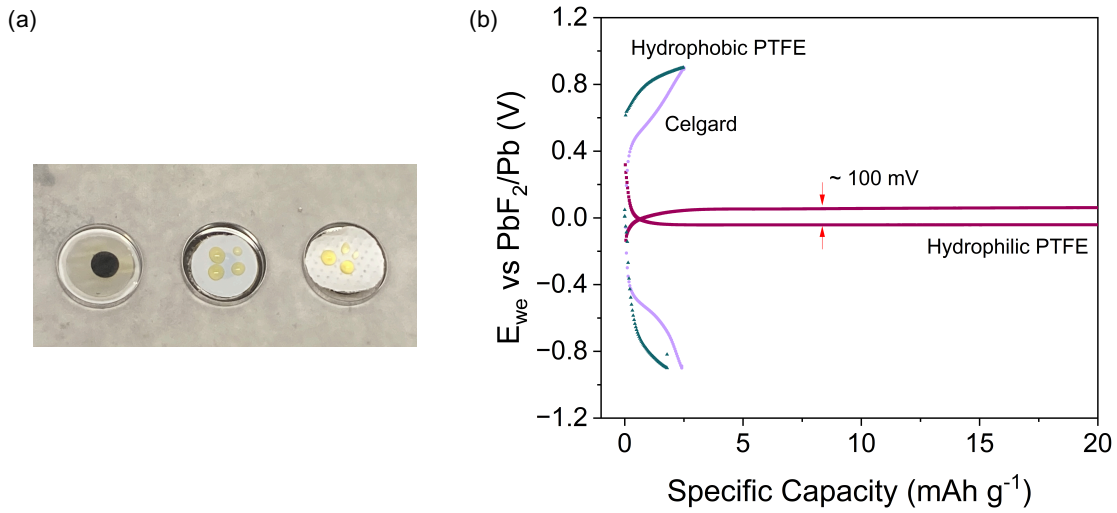


Figure 3.9: Separators wetting with an ionic liquid-based electrolyte. **(a)** Hydrophilic PTFE (left) wetted instantaneously, whereas droplets of electrolyte formed on the surface of both polyolefin (centre) and hydrophobic PTFE (right). **(b)** Overpotential of different separators in a Pb-PbF_2 symmetric coin cell. Hydrophilic PTFE showed the lowest overpotential (~100 mV), whereas both polyolefin and hydrophobic PTFE exhibited an extremely large overpotential with virtually no cycling capability.

The hydrophilic PTFE separator proved to be the most promising separator for FIBs among the three materials tested. On the other hand, the polyolefin separator demonstrated to be suitable for low viscosity electrolytes, but not for ionic liquid-based separators, as expected.

To further assess the compatibility of the hydrophilic PTFE separator, its electrochemical stability was tested in the potential range used for the cycling of the Pb-PbF_2 coin cells. Coin cells were assembled with stainless steel blocking electrodes and two hydrophilic PTFE separators to check for the occurrence of any current-drawing reaction during cycling. The cells were cycled using a ±12 μA current with a voltage cut-off of ±1.5 V vs stainless steel. The upcoming chapters will focus on cells, such as symmetric Pb-PbF_2 and BiF_3 vs Pb-PbF_2 configurations, which operate within this voltage window. The coin cells did not show any significant capacity (Fig. 3.10) suggesting that hydrophilic PTFE separators do not oxidise or reduce in that potential window.

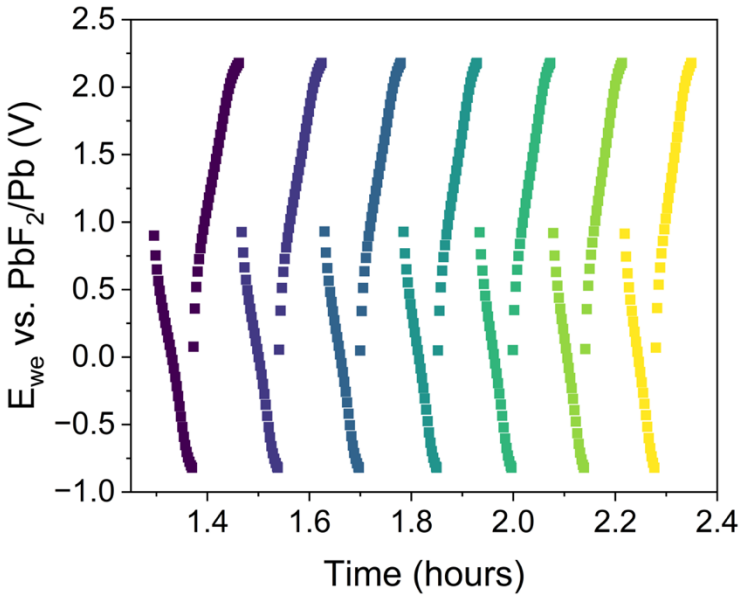


Figure 3.10: Cycling of the hydrophilic PTFE separator in a coin cell with stainless-steel blocking electrodes. The lack of capacity in each cycle indicates the lack of parasitic reactions, and therefore the electrochemical stability of this separator in the voltage window ~2.0 V – ~-0.7 V vs PbF_2/Pb. A current of ±12 µA was applied. The redox potential of stainless steel was approximated as 0.68 V vs PbF_2/Pb.

Due to their impressive performance, hydrophilic PTFE separators were selected for cycling FIB coin cells. These separators can effectively wet both low and high viscosity electrolytes and are electrochemically stable within the cell's operating voltage.

3.2.5 Cycling of Pb-PbF_2 counter-reference electrodes in 2-electrode coin cells

With all the components ready, the suitability of the Pb-PbF_2 counter-reference electrodes for 2-electrode coin cells could be tested. Coin cells were assembled in the following way. Pb-PbF_2 symmetric cells were used, meaning that Pb-PbF_2 was employed for both the working and counter-reference electrode. Two 18-mm diameter hydrophilic PTFE separators, instead of one, were inserted between the electrodes. This choice was made to minimise the chance of short circuiting, given the small thickness of each PTFE disc (65 µm). Additionally, two 0.5 mm thick stainless-steel spacers were added to ensure sufficient pressure within the coin cell, given the lack of current collectors (Fig. 3.11). Electrolyte excess was also used to

prevent any electrolyte degradation from limiting the performance of the cell. The cells were cycled at C/20 (a full charge or discharge occurs in 20 hours) to prevent the electrolyte's kinetics from affecting the cycling performance.

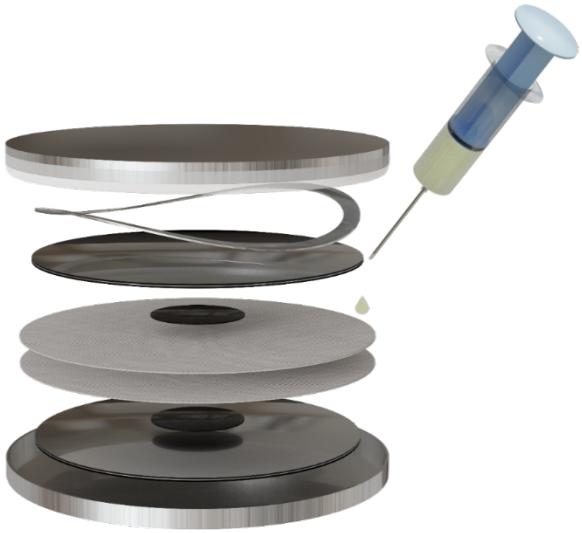


Figure 3.11: Schematic of a coin cell stack used in this work. Two hydrophilic PTFE separators were placed between the two self-standing electrodes and a stainless-steel spacer was placed next to each electrode.

The cycling performance of the Pb-PbF_2 symmetric cells, shown in Fig. 3.12, proves the suitability of these electrodes as counter-reference electrodes for coin cells. In fact, the low (± 30 mV) and constant overpotential throughout cycling, both on charge and discharge, and the reversibility of the reaction demonstrates the reliability of Pb-PbF_2 counter-reference electrodes.

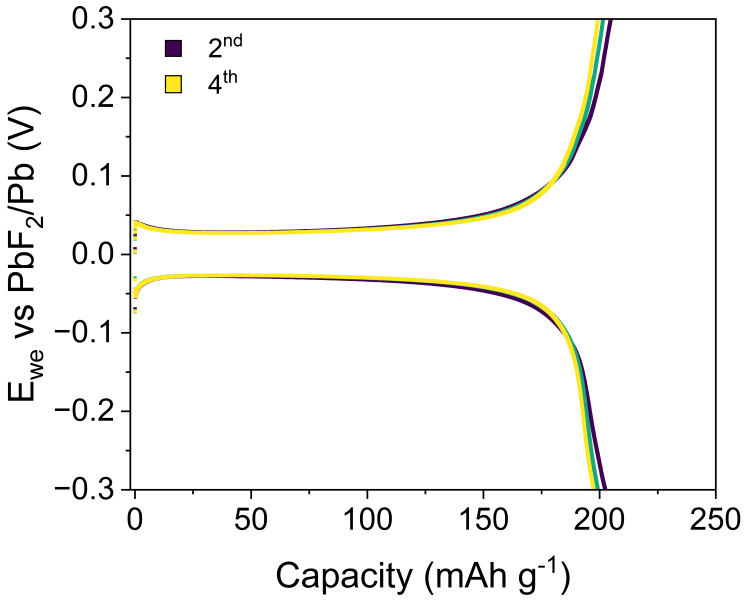


Figure 3.12: GCPL plot of a symmetric coin cell featuring Pb-PbF_2 counter-reference electrodes, cycled at a C/20 rate (10.9 mA $g^{-1}_{PbF_2}$) The counter electrode has higher loading than the working electrode. The second (blue), third (green) and fourth (yellow) cycles are shown. The flat plateau of the three reversible cycles proves the suitability of the counter-reference electrodes and inactive components (binder, and separator) for their use in coin cells.

A more detailed analysis of the cycling performance of Pb-PbF_2 is provided in Chapter 4 and 5, depending on the electrolyte used for the cycling. The cycling data reported here is collected with the organic electrolyte presented in Chapter 4.

3.3 Conclusion and Future Work

This chapter showcased the possibility of more reliable form-factors for FIBs, specifically coin cells, rather than the impractical and unrealistic flooded cells. This was achieved by solving the problems that have prevented coin cells from being used for FIBs. Namely, the lack of a reliable counter-reference electrode and a suitable separator. Careful microstructural design of Pb and PbF_2 particles and the use of a chemically stable binder (PTFE) resulted in a reliable counter-reference electrode for 2-electrode cells. Hydrophilic PTFE was demonstrated to perform well as a separator, exhibiting good wetting with both low

and high viscosity electrolytes and electrochemical stability within the battery operating voltage.

Further work is required to experimentally test the chemical compatibility of hydrophilic PTFE separators with F-ion containing liquid electrolytes. Despite the fact that the separator's performance during cycling did not seem to change (overpotential did not grow in Chapter 4 and 5), the thin (a few nm-thick) hydrophilic layer could still release trace amounts of HF or other by-products. One approach to test the chemical compatibility might involve submerging a separator in a solution containing F-ions and detecting using ^{19}F NMR if any new peaks emerge. Additional peaks would indicate the presence of new fluoride environments arising from the reaction between F-ions and the hydrophilic components of the separator's surface.

Additional work is also needed to further optimise the microstructure of the Pb-PbF_2 counter-reference electrodes, particularly to increase porosity. Higher porosity would allow for improved wetting with viscous electrolytes and better cycling capability. This is far from trivial to achieve given the high ductility of Pb. A different active material might be needed to obtain higher porosity, but this change could negatively impact cycling performance, thereby overshadowing the benefits of increased porosity.

Finally, to successfully and accurately study the behaviour of working electrodes cycled against the Pb-PbF_2 counter-reference electrode, it is necessary to establish a system to correct the profiles of the working electrode from the overpotential of the counter-reference electrode. To do so, the overpotential of the Pb-PbF_2 counter-reference electrode (for a given electrolyte and electrode mass) should be recorded at different cycling rates. The overpotential of the counter-reference electrode can then be subtracted from the operating potential of the cell featuring the working electrode and the Pb-PbF_2 counter-reference electrode. In this way, the

cycling profile will represent exclusively the behaviour of the working electrode. At low cycling rates this additional correction procedure might not always be necessary due to the low overpotential of the Pb-PbF_2 counter-reference electrode. However, this might become more relevant at higher cycling rates.

The coin cell set-up presented in this chapter allowed for the accurate investigation of the cycling performance of the novel liquid electrolytes discussed in the next two chapters. In the next chapter, I discuss a novel strategy to design liquid electrolytes for FIBs using a highly concentrated electrolyte with a diluent. I then test the cycling performance of the new electrolyte in the coin cell set-up discussed in the current chapter.

Chapter 4

A Diluted Liquid Electrolyte with Improved Cyclability

Table of Contents

4.1 Introduction 82

4.2 Results and Discussion 84

4.2.1 Selection and synthesis of fluoride salt 84

4.2.2 Selection of solvents 89

4.2.3 Characterization of solvation structure 90

4.2.4 HF formation 95

4.2.5 Characterization of electrolyte properties 96

4.2.6 Cycling of Pb-PbF_2 electrodes in the diluted electrolyte 97

4.2.7 Cycling of BiF_3 vs Pb-PbF_2 in the diluted electrolyte 102

4.2.8 Cycling of CuF_2 vs Pb-PbF_2 in the diluted electrolyte 106

4.3 Conclusion and Future Work 107

4.1 Introduction

It is particularly challenging to develop liquid electrolytes for fluoride-ion batteries. Firstly, fluoride salts are insoluble in organic aprotic solvents, which are commonly used in electrolytes for batteries.[84] This is the reason why anion acceptors have been widely investigated in FIBs. Additionally, F-ions, due to their very high reactivity, can easily extract acidic protons from the electrolyte's solvent, forming the corrosive HF. In fact, the great majority of liquid electrolytes in FIBs contain significant amounts of HF or HF_2^-.

The problem of solubility can be circumvented by using protic organic solvents, although these introduce a new set of challenges. Fluoride salts are extremely soluble in protic organic solvents thanks to the capability for hydrogen bonding between the solvent and F-ions.[84] The disadvantage of protic solvents, however, is the limited electrochemical stability window (ESW) due to the reactivity of the hydroxylic proton that reduces at intermediate potentials. This is the reason why protic solvents are not generally used for

battery electrolytes. Another disadvantage of protic solvents, which is specific to FIBs, is the possibility of forming corrosive HF due to the acidity of the proton responsible for F-ion solvation.

Protic organic solvents can be used in battery electrolytes if these drawbacks are mitigated. The use of protic solvents has already been demonstrated in LIBs and recently for the first time in FIBs as well (a work co-authored by me and other members of the group). The strategy to employ protic solvents involves increasing the concentration of salt to achieve a highly concentrated electrolyte. The availability of non-associated solvent molecules reduces with increasing salt concentration, leading to an expansion of the electrochemical stability window. In FIBs, high concentrations of salt also minimise HF formation, as donating solvent molecules become scarcer and the solution becomes more basic.[85]

Highly concentrated electrolytes, however, introduce two new problems. High salt concentrations lead to a large increase in viscosity, which may negatively influence the transport properties as well as the wetting of the separator and electrodes inside the cell. Additionally, such high concentrations of salt make the electrolyte impractical and expensive. In LIBs diluents are often added to highly concentrated electrolytes since they mitigate both issues. A good diluent ideally does not interact with the salt to not interfere with the solvation shell, has a wide ESW and it is miscible with the highly concentrated electrolyte.[86–89] The use of a diluent has attracted a growing interest in recent years in LIBs, however, it has never been applied to FIBs.

In this chapter, I discuss the properties of a highly concentrated electrolyte consisting of tetramethylammonium fluoride (TMAF) in methanol (MeOH) and how these change with the addition of propionitrile (PN) as the diluent. I also report the

electrochemical performance of the diluted electrolyte in the coin cell set-up introduced in the previous chapter.

All the work in this chapter was performed by me under the supervision of Prof. Mauro Pasta. Exceptions are the Monte Carlo simulations that were performed by Dr Camilla Di Mino and the measurement of the diffusion coefficient of F-ions via pfg-NMR which was done by Dr Gregory Rees. Some of the results in this chapter are part of the work that is under review in *ACS Energy Letters* authored by Giulia Galatolo, Omar Alshangiti, Dr Camilla Di Mino, Dr Guillaume Matthews, Dr Albert Xiao, Dr Gregory Rees, Maximilian Schart, Yvonne Chart and Prof. Mauro Pasta.

4.2 Results and Discussion

4.2.1 Selection and synthesis of fluoride salt

Among different organic fluoride salts, TMAF was chosen as the fluoride salt for the diluted electrolyte. Organic fluoride salts were considered rather than inorganic salts (eg. KF, CsF, NaF), because of their tendency to have higher solubility.[84] Tetramethylammonium fluoride (TMAF) seemed particularly appealing because it offers a source of free F-ions, its cation displays good chemical stability, and its cost is low. The chemical stability of $N(CH_3)_4^+$ arises from the high strength of the C-N bond (which provides a high activation energy towards chemical reactions), as well as from the lack of β-hydrogens.[7] These appealing characteristics were the reason why TMAF was chosen as the fluoride salt for the diluted electrolyte.

TMAF, however, has two main limitations that made the development of liquid electrolytes challenging. It is less soluble than bulkier organic salts, such as tetraethylammonium fluoride (TEAF), and is extremely hygroscopic and complicated to

dry.[21,84,90] The first drawback limits the number of solvents capable of dissolving TMAF, whereas the second one makes it difficult to obtain truly anhydrous electrolytes.

High water contents in liquid electrolytes are problematic, and in FIBs particularly so. Water can lead to parasitic reactions and have a detrimental effect on the electrochemical stability window of the electrolyte.[91,92] Even more concerning in FIBs, water can lead to HF formation. For these reasons, the water content in TMAF must be reduced as much as possible to minimise its impact on the electrolyte's properties.

Commercial TMAF is available in two different forms, which both have an unfeasibly high-water content. The first is tetrahydrate and has 98% purity, whereas the second form of TMAF is non-hydrated and has 97% purity. Unfortunately, the 3% impurity in the non-hydrated TMAF is almost all water, making it extremely wet as well. To use either of these two commercially available TMAF in the electrolyte, the water content must be substantially diminished.

Reducing the water content of commercial TMAF was possible but achieving a low enough water content was extremely challenging.[84] TMAF has a low degradation temperature that prevents it from being heated up to high temperatures to accelerate water evaporation. In fact, at ~170°C TMAF starts to decompose into $N(CH_3)_3$ and CH_3F while the rate of water evaporation is still low.[93] Heating TMAF powder at ~150°C under vacuum reduces the water content to ~1.5%, but further water removal is not feasible due to the slow evaporation rate at this temperature. Even the so-called "truly anhydrous" TMAF reported in the literature still contains over a thousand ppm of water, which is still far too high for battery applications.[90]

In an attempt to achieve water contents of a few hundred ppm, tetrahydrate TMAF was dried according to a newly developed multi-step procedure described in detail in the methods section (Chapter 2). This method, in addition to the usual heating under vacuum step, includes a drying step with molecular sieves to capture the water molecules released once TMAF is dissolved into a solvent. The final water content achieved with this procedure was 1000 ppm, which was lower than what could be achieved simply by heating under vacuum. However, this water content is still far too high for the TMAF to be used in the electrolyte.

To obtain TMAF with an acceptable water content a synthesis procedure was used instead. In the literature, two main procedures are available for the synthesis of TMAF.[93] The first one, which dates to 1888, consists of the neutralization of tetramethylammonium hydroxide with HF in aqueous solution, followed by heating to 160°C in vacuum to remove the water. This is the method used to produce the commercially available tetrahydrate TMAF, since tuning the drying temperature varies the number of water molecules coordinated to TMAF ($N(CH_3)_4F$-nH_2O with n = 1-5). This method produces wet TMAF, as the rate of water evaporation at 160°C is still slow while the TMAF is already beginning to decompose. Additionally, HF_2^- impurities are also present. The second method involves the reaction of $N(CH_3)_4Cl$ with KF in methanol to give $N(CH_3)_4F$ and KCl. This method produces drier TMAF, but the final product contains at least 1-2% Cl^- impurities.[93]

Although an optimisation of both procedures is available in the literature, the second synthesis was selected. The lack of HF and the smaller number of steps made it more appealing and practical. The method followed to achieve dry TMAF was the one proposed by Kolomeitsev et al., which uses tetramethylammonium tetrafluoroborate ($N(CH_3)_4BF_4$,

TMATFB) to replace $N(CH_3)_4Cl$ and avoid chloride impurities. In their work, TMAF free from MeOH, HF_2^-, BF_4^- and SiF_6^{2-} impurities, and with only ~600 ppm of water was achieved.[94] A description of the synthesis steps including some improvements made to the original procedure is available in the methods section (Chapter 2).

To verify the success of the procedure, the purity and water content of the synthesised TMAF were tested. This characterisation was done using X-ray diffraction (XRD), nuclear magnetic resonance (NMR), Fourier-transform infrared spectroscopy (FT-IR), and Karl Fisher titration (KFT). The XRD pattern of the synthesised powder (Fig. 4.1-a) matches well the hexagonal unit cell of TMAF reported by Christe et al., indicating that the synthesis successfully produced the desired material.[93] Only two additional small peaks at 24° and 31.1° can be attributed to some unknown impurity, as they do not correspond to either of the two precursors or the by-product (KBF_4). The origin of the unknown impurity might be linked to the TMATFB precursor, which was only 97% pure. The successful synthesis of TMAF was confirmed by ^{19}F NMR, which shows a perfect match between the chemical shift of the synthesised TMAF in water (-119 ppm) (Fig. 4.1-b) and the value reported by Christe et al.[93] Furthermore, the lack of additional peaks indicates the absence of other fluorinated impurities, such as TMATFB, KF or KBF_4. The structure of TMAF and its purity was further demonstrated with FT-IR. Once again, the spectrum of the synthesised TMAF (Fig. 4.1-c) is in very good agreement with what Christe at al.[93] reported. The FT-IR spectra also shows a lack of substantial water content present in the synthesised TMAF. This is evident by the absence of a sharp peak at 1634 cm^{-1}, corresponding to the water O-H scissors and a broad intense peak at 3266 cm^{-1} arising from the O-H stretch. To quantify more accurately the water content, the synthesised TMAF was dissolved in anhydrous isopropanol at a known concentration and KFT was employed. The water content was

found to be less than 300 ppm, which is about half of what was reported by Kolomeitsev et al. with the original synthesis procedure.[93,94] This lower water content might be ascribed to the higher drying temperature of TMATFB (200°C compared to 90°C), the longer drying time of the last step (7 days compared to 48 hours), the lack of exposure to air throughout the entire process and the use of dried plastic containers. By using this synthesis procedure, it was possible to obtain virtually pure TMAF with the lowest water content ever reported for this salt (Table 4.1). With such a water content the synthesised TMAF was therefore suitable to be used in the development of the diluted electrolyte.

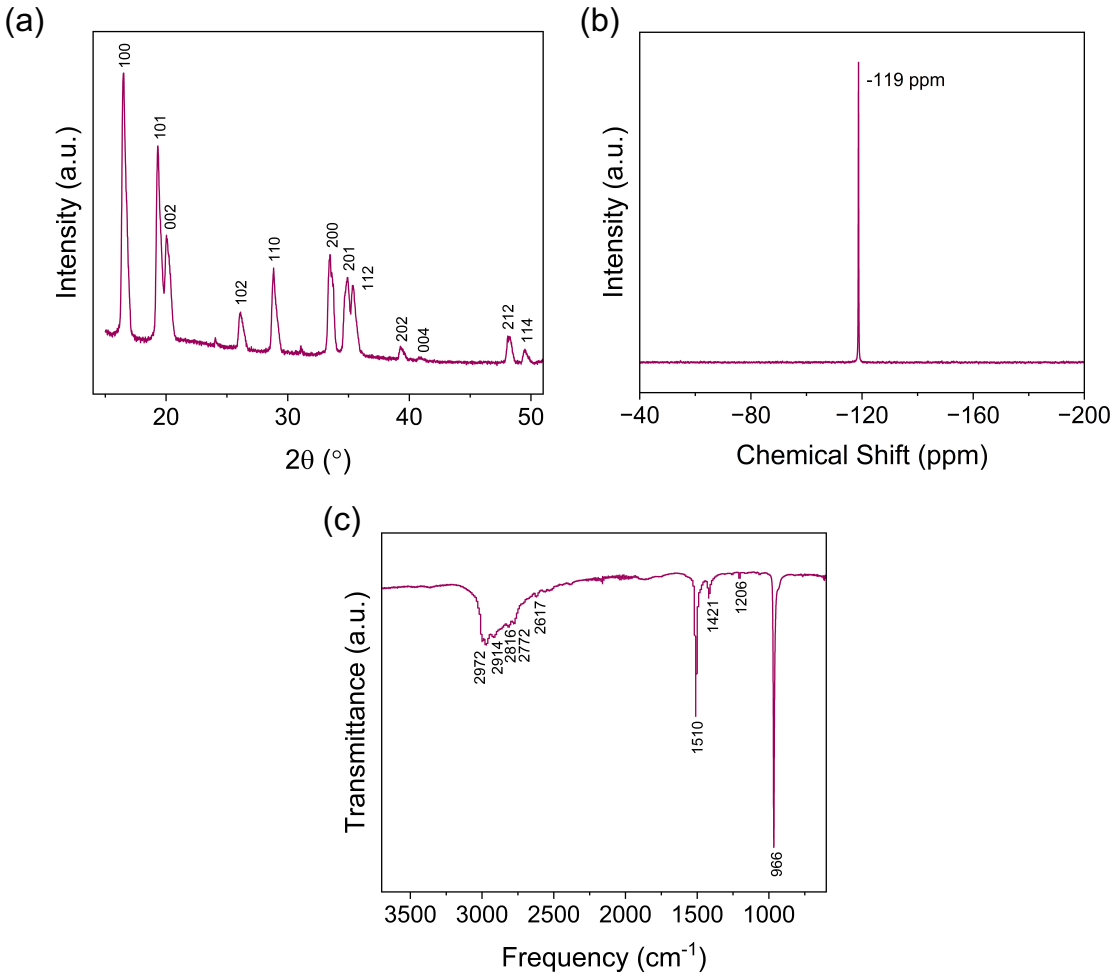


Figure 4.1: Characterisation of TMAF. **(a)** XRD, **(b)** ^{19}F NMR and **(c)** FT-IR confirm the successful synthesis of TMAF and the lack of precursors or by-products impurities.

Table 4.1: Comparison of the water content in tetramethylammonium fluoride achieved in this work and what has been obtained in the literature.

Water content (ppm)	Reference
300	this work
600	93
600	94
1600	90

4.2.2 Selection of solvents

After selecting and preparing the fluoride salt, the protic solvent and diluent had to be determined. Methanol was selected as the protic solvent for its ability to dissolve TMAF at high concentrations. Among protic solvents, alcohols exhibit the ability to dissolve fluoride salts due to the hydrogen bonding between the –OH group and F-ions. Choosing an alcohol capable of dissolving TMAF to high concentrations is important to maximise the expansion of the electrochemical stability window.[95] Within alcohols, methanol stands out thanks to its superior solvation capability, arising from the high dielectric constant (ε = 33). This is evident from the fact that the maximum concentration of TMAF that can be dissolved in isopropyl alcohol (ε = 21.8) is limited to 3 m, whereas in methanol, it reaches 10 m. Hence, methanol was selected as the solvent for solvating F-ions.

Propionitrile (PN) was chosen as the diluent for its numerous advantages. These include a wide electrochemical stability window (>5 V), low viscosity (0.399 mPa.s at 25°C) and high boiling point (97°C).[96,97] Low viscosity is crucial to satisfy one of the main purposes of a diluent: reduce the viscosity of the highly concentrated electrolyte. Additionally, propionitrile is chemically stable towards fluoride ions, which prevents

chemical degradation of the electrolyte, and does not dissolve TMAF, with a solubility of only 2 x 10^{-4} mol kg^{-1} (Fig. 4.2).[98] This last property is crucial for PN to behave as a diluent instead of a co-solvent. Finally, PN is miscible with alcohols, which prevents phase separation in the diluted electrolyte.

The chosen electrolyte comprises TMAF as the fluoride salt, MeOH as the protic solvent and PN as the diluent. A 10 m solution of TMAF in MeOH was diluted with PN to reach a final concentration of 0.5 m. This results in a ratio of 5%wt MeOH - 95 %wt PN.

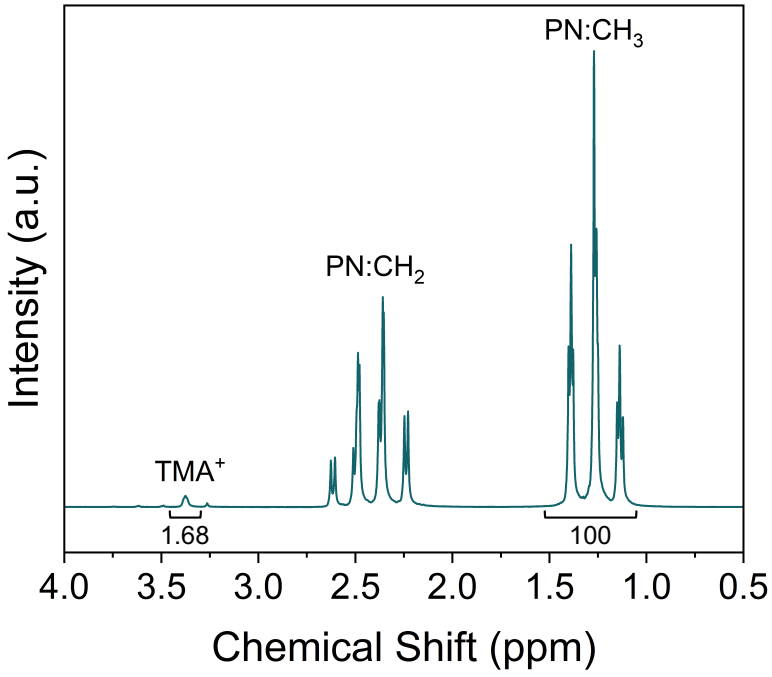


Figure 4.2: ^{1}H NMR of saturated TMAF in propionitrile. The integral of the peaks of TMA^{+} (1.68) and the methyl group of PN (100) leads to a maximum TMAF concentration of 2 x 10^{-4} mol kg^{-1} in PN, demonstrating lack of solubility.

4.2.3 Characterization of solvation structure

A combination of spectroscopic and computational characterisation methods was employed to investigate the structure of the highly concentrated electrolyte, and how it changes after adding the diluent. Particular focus was paid on the solvation of the fluoride ion, both with and without the diluent.

Among the spectroscopic methods, NMR shows evidence of hydrogen bonding between the proton of the –OH in MeOH and F-ions in the highly concentrated electrolyte. In the ^{1}H NMR spectra, the shift of the hydroxylic proton to higher frequencies with rising TMAF concentration reaches a maximum of 2.3 ppm at 10 m (Fig. 4.3-a,b). This shift in the proton NMR is matched by a shift to higher frequencies of the fluoride peak in the ^{19}F NMR of 12.9 ppm at 10 m (Fig. 4.3-c,d). The increase in number of –OH···F^- bonds at a higher TMAF concentration is also confirmed by the broadening of both -OH and F^- peaks greater than 0.2 ppm at the 10 m concentration (Fig. 4.3-b,d). This is a result of the restricted (and hence slower) motion of both F^- and the hydroxylic proton, arising from the tight bond between them.

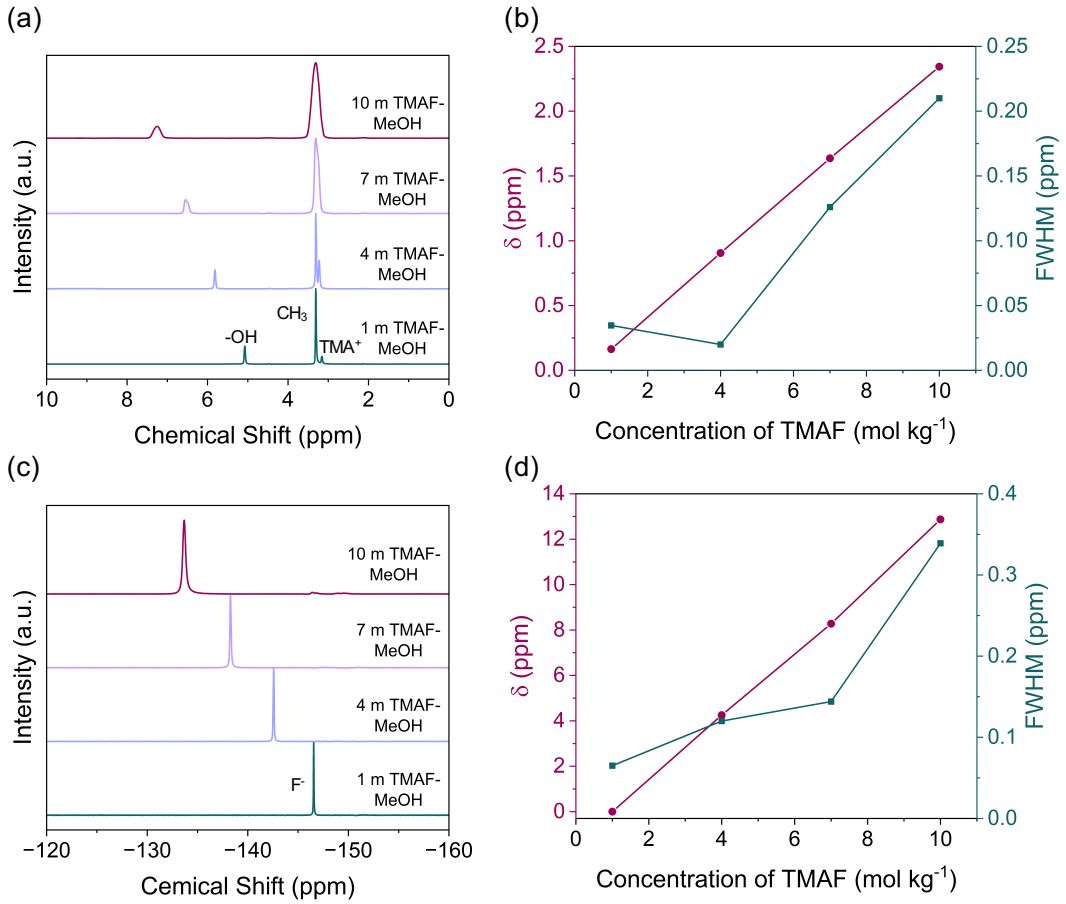


Figure 4.3: Solvation of F-ions by the hydroxylic group of MeOH. **(a)** ^{1}H NMR of TMAF in MeOH at different concentrations, and **(b)** corresponding -OH peak shift (δ) to high frequencies and increase in full width at half maximum (FWHM). **(c)** ^{19}F NMR of TMAF in MeOH at the same four concentrations, and **(d)** corresponding F^- peak shift (δ) to high frequencies and increase in FWHM.

Monte Carlo simulations were used to investigate the solvation structure, and how it changes upon the addition of PN. The simulations confirmed the hydrogen bonding between MeOH and F-ions. The bond length between the hydroxylic proton and F^- was calculated to be 1.58 Å (Fig. 4.4-a,b,c), in alignment with reported gas-phase calculations.[99] According to the calculated solvation structure, an average of 2.3 ± 0.1 MeOH molecules interact with each F-ion in the highly concentrated electrolyte (Fig. 4.4-c). TMA^+ counter ions are found in the proximity of fluoride ions, at a distance of 2.58 Å (Figure 4.4-e), due

both to strong coulombic interactions, and the tendency to form ion-pairs and aggregates in highly concentrated solutions.[100,101]

Upon addition of PN, the hydrogen bonding between MeOH and F-ions is retained, although the solvation shell around F-ions is slightly altered. In the diluted electrolyte, the –OH···F^- distance of 1.58 Å does not change, while the average number of MeOH molecules coordinated to F-ions decreases from 2.3 ± 0.1 to 0.5 ± 0.1 (Figure 4.4-c). This is caused by the competing interaction between PN and MeOH, and the large excess of the former. Adding the diluent decreases (from four to two) the number of TMA^+ ions interacting with each fluoride ion at a distance of 2.58 Å. Similarly, the number of TMA^+ molecules interacting with F-ions at a longer distance (~4 Å) also decreases, reaching four TMA^+ per F^- (Table 4.2 displays a summary of all interactions with F-ions). This change might indicate a modified arrangement between F-ions and their cations, and the formation of more complex structures such as tetramers in the diluted electrolyte.[102]

The simulations also indicate the presence of microsegragation between methanol and propionitrile in the diluted electrolyte. This is evident from the remarkable increase in peak intensity in Fig. 4.4-f. The microsegregation can be attributed to the known tendency of methanol to form linear and cyclic hydrogen bonding motifs, as it has been seen before in alcohol-water mixtures.[103,104] Microsegregation of methanol further indicates a strong solvation of fluoride ions by methanol, while propionitrile interacts with the anions by weaker van der Waals forces (Fig. 4.4-d propionitrile CH_2···F^-) such as dipole-ion and weak hydrogen bonding. The weaker interaction compared to MeOH matches the inherent insolubility of TMAF in PN. These results have shown that propionitrile acts as a diluent by interacting with F-ions via weaker van der Waals forces, which do not alter the distance

between F^- and MeOH (Fig. 4.4-a,b,c) and by reducing the viscosity of the highly concentrated electrolyte.[89]

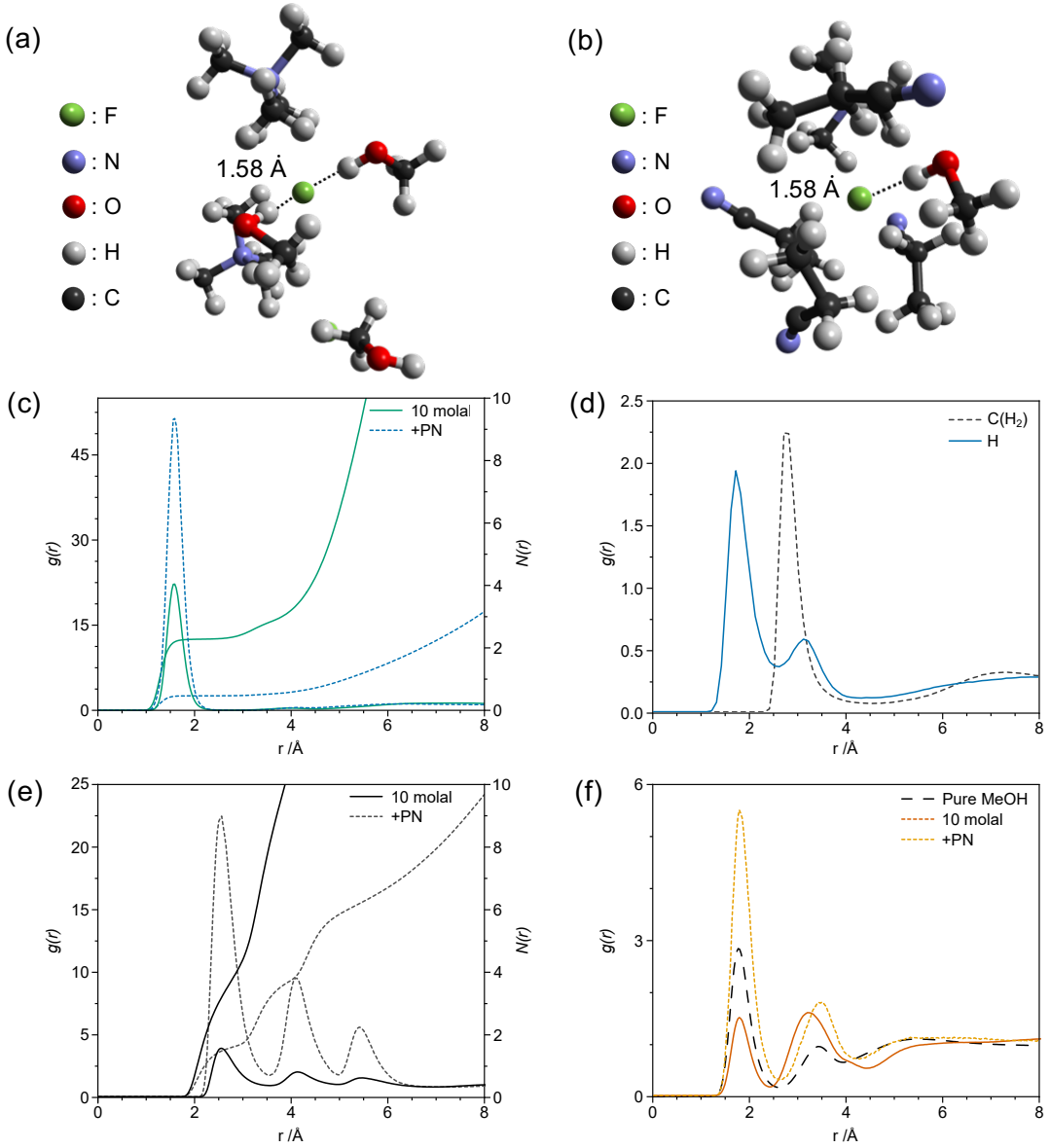


Figure 4.4: Solvation structure calculated by Monte Carlo simulations. Snapshots of Monte Carlo simulation boxes showing F^- solvated by: **(a)** MeOH molecules in the highly concentrated electrolyte, and **(b)** MeOH and PN in the diluted electrolyte. Partial Radial Distribution Functions g(r) relative to: **(c)** fluoride ion and hydroxylic proton of methanol in presence (blue) and in absence of propionitrile (green). Note that the peak position does not change with the addition of the diluent; **(d)** F^- and CH_2 of PN; **(e)** F^- and H of TMA^+ in presence (dotted line) and absence (solid line) of PN; **(f)** MeOH proton H and methanol oxygen O in the pure liquid methanol, in the highly concentrated electrolyte and in the diluted electrolyte. Note that the hydrogen bonding network of methanol is preserved.

Table 4.2: Summary of the hydrogens from different molecules interacting with F-ions. The distance and coordination number for each interaction are compared between the highly concentrated (10 m TMAF-MeOH) and the diluted (0.5 m TMAF-5wt%MeOH-95wt%PN) electrolytes.

Interaction	10 m TMAF-MeOH		0.5 m TMAF-5wt%MeOH-95wt%PN	
	Distance (Å)	Coordination number	Distance (Å)	Coordination number
(MeOH) –OH···F^-	1.58	2.3	1.58	0.5
(TMA^+) –CH_3···F^-	2.58	4	2.58	2
	4	>10	4	4
(PN) –CH_2···F^-	N/A	N/A	1.8	-

4.2.4 HF formation

The tight bond between F^- and the hydroxylic proton in MeOH can be a concern due to the possible generation of large amounts of HF in the electrolyte. To estimate the degree of HF formation, the equilibrium constant for the HF formation reaction was calculated by combining the acidic dissociation constants (K_a) for methanol and HF:

$$MeOH + F^- \rightleftharpoons MeO^- + HF \quad (4.1)$$

The K is 4.6 x 10^{-13} indicating that the equilibrium in eq. (4.1) is shifted to the left. The low number indicates that the formation of the products, including HF, is not favourable. This does not indicate that HF is not present in the electrolyte but rather that its concentration will be very low. Even more so in the diluted electrolyte in which only 5% of MeOH is present.

4.2.5 Characterization of electrolyte properties

After establishing the role of the diluent in the solvation structure, the subsequent step was to explore how propionitrile influences both transport and electrochemical properties. Following the addition of PN, the reduced viscosity and the lower number of MeOH molecules coordinated to fluoride ions results in a one order of magnitude increase in the fluoride diffusion coefficient (1.4×10^{-9} m^2 s^{-1}) compared to the highly concentrated electrolyte (2.05×10^{-10} m^2 s^{-1}). Meanwhile, the ionic conductivity was still high at 7 mS cm^{-1}, despite decreasing from the 28 mS cm^{-1} of the highly concentrated electrolyte. This decrease is due to the considerably lower number of charge carriers in the diluted electrolyte. An ionic conductivity of 7 mS cm^{-1} is still higher than that of most liquid electrolytes for FIBs.[45,47,68]

In addition to improving F-ion transport and decreasing the amount of salt required, the diluted electrolyte retained the main advantage of the highly concentrated electrolyte, namely the wide ESW. In fact, the ~0.5 V expansion in the electrochemical stability window between 1 m and 10 m TMAF in MeOH (from 2.4 V to 2.86 V) (Fig. 4.5-a) was maintained after the addition of propionitrile (Fig. 4.5-b). The widening of the ESW occurring only on reduction, rather than equally between oxidation and reduction, might be related to the counter-reference electrode used. In fact, the redox potential of the Pb-PbF_2 reference electrode depends on the activity of the fluoride ions in solution. And this will change considerably between the two different concentrations. Hence, the expansion of the ESW window should be taken as an absolute value rather than a precise indication of its limits.

Overall, these results show that the addition of propionitrile to the highly concentrated electrolyte increases the diffusion coefficient of F^- by an order of magnitude, while obtaining a high ionic conductivity and retaining a similarly wide electrochemical stability window. Additionally, using a diluent reduces the amount of salt needed, making the electrolyte more practical.

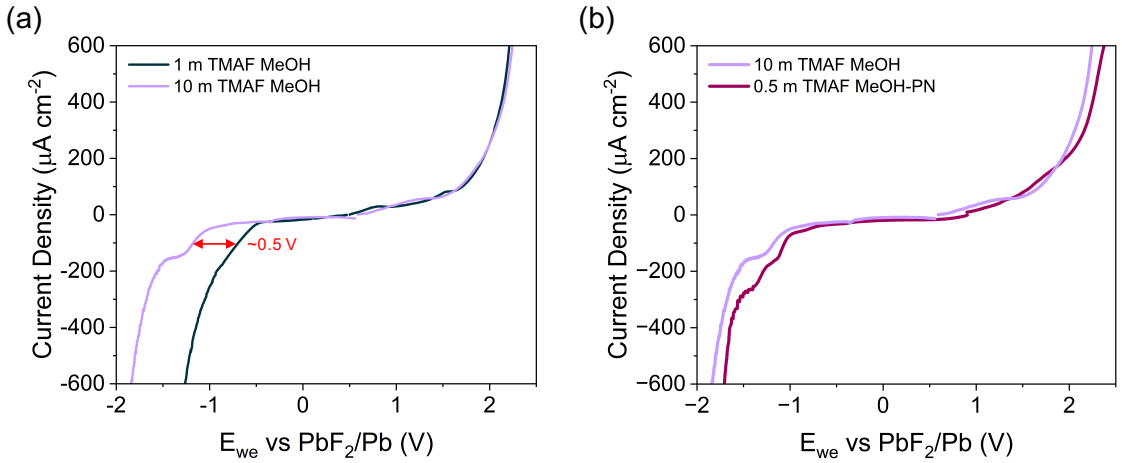


Figure 4.5: Electrochemical stability window. **(a)** The ESW widens by 0.5 V by increasing the TMAF concentration in MeOH from 1 to 10 m. **(b)** The wider ESW is retained in the diluted electrolyte.

4.2.6 Cycling of Pb-PbF_2 electrodes in the diluted electrolyte

After the solvation structure and properties of the electrolyte were characterized, its cycling performance was investigated. The electrochemical performance of the diluted electrolyte was tested in symmetric coin cells with the Pb-PbF_2 electrodes, and the inactive components selected in Chapter 3, using galvanostatic cycling and ex-situ XRD. The electrodes used had 48 wt% Pb, 48 wt% PbF_2, 3 wt% carbon nanofibers and 1 wt% PTFE and 80 µm thickness. Since the cells were assembled in a 50% state of charge, the maximum capacity accessible on the 1st discharge is half the theoretical capacity (109 mAh g^{-1}). Starting from the 1st charge, the maximum achievable capacity corresponds to the theoretical capacity of PbF_2 (218 mAh g^{-1}).

The cells achieved almost theoretical capacity on the first cycle and excellent capacity retention for 30 cycles. On the 1st discharge, 106 out of the 109 mAh g^{-1} was accessed (Figure 4.6-a), suggesting that almost all the active material underwent the conversion reaction. On the first charge, the capacity reached 211 out of the 218 mAh g^{-1} and then decreased to 202 mAh g^{-1} on the 2nd discharge (Figure 4.6-a,b). The XRD at the end of the 1st charge and 2nd discharge confirmed that the obtained capacity arose from the reversible conversion between Pb and PbF_2 (Figure 4.6-c). Upon recharge the β-crystal structure of PbF_2 converted to the α-phase, suggesting it is the most kinetically stable under these conditions.[24] In the FIBs literature, both the reversible cycling of β-PbF_2 and the conversion from β- to α-PbF_2, as in this case, have been reported.[24,68] More work is required to understand the underlying causes of this interesting mechanism. The cell retained 97.8% of its original capacity after the 30th cycle, because of a slowdown in capacity fading between the 15th and 20th cycle and an increase in capacity between the 20th and 30th cycles. Additionally, it exhibited a low overpotential of 30 mV on both charge and discharge, which remained constant throughout cycling (Figure 4.6-a). These results outperform previously reported Pb-PbF_2 electrodes, including in flooded cells.[24,28,44,68]

The presence of a reliable counter-reference electrode and the realistic cell design also allowed meaningful measurements of coulombic efficiency, rarely reported for FIBs. The coulombic efficiency started at 96% on the 1st cycle, and from the 15th cycle plateaued at ~101% (Figure 4.6-b). The value higher than 100%, coupled with the increase in capacity after the 20th cycle could be indicative of a parasitic reaction with the electrolyte or a partial dissolution of the active material. The dissolved ions of the active material in the electrolyte can plate on the other electrode during cycling, increasing the capacity and leading to a higher than 100% coulombic efficiency. Unfortunately, in a symmetric cell, the plating of

the dissolved ions cannot be detected from XRD, as the active material is the same in both electrodes.

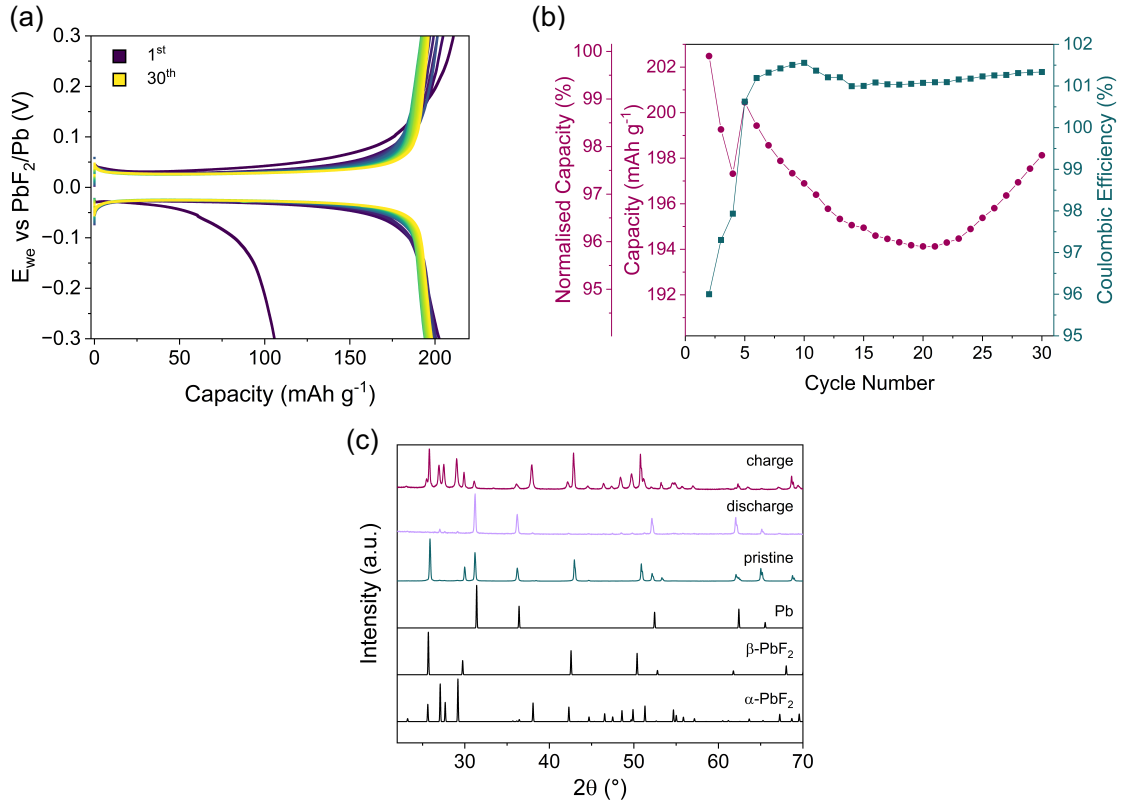


Figure 4.6: Cycling performance of Pb-PbF_2 electrodes in 0.5 m TMAF MeOH-PN. **(a)** GCPL plot showing the cycling of a Pb-PbF_2 symmetric cell at a C/20 rate (10.9 mA $g^{-1}_{PbF_2}$). **(b)** Capacity, normalised capacity and coulombic efficiency as a function of cycle number for the Pb-PbF_2 symmetric cell. **(c)** XRD demonstrating almost full conversion after 1st charge and 2nd discharge.

To assess how the diluent influenced cycling performance, the cycling of Pb-PbF_2 electrodes in the diluted electrolyte was compared to the cycling of the same set-up with the highly concentrated electrolyte (10 m TMAF in MeOH). The diluted electrolyte led to an improvement in cycling performance compared to the highly concentrated electrolyte. In fact, the absence of diluent resulted in a lower capacity retention of 78.5% on the 30th cycle compared to 97.8% with the diluted electrolyte (Fig. 4.7-a,b). Interestingly, the lack of diluent did not cause an increase in overpotential due to the higher viscosity of the highly

concentrated electrolyte (Fig. 4.6-a, Fig. 4.7-a). This suggests that the separator was capable of wetting well even with the highly concentrated electrolyte, as well as spreading the electrolyte within the coin cell. This is not surprising given that the hydrophilic PTFE separator wetted well even with an ionic liquid-based electrolyte (Chapter 3). The coulombic efficiency increased to over 100% between the 9th and 14th cycles, similarly to the diluted electrolyte. However, it then decreased to below 100% and it plateaued at ~99.5% until the 30th cycle (Fig. 4.7-b). The over 100% coulombic efficiency with the diluted electrolyte, but not with the highly concentrated electrolyte, suggests that the diluent is the cause of the higher active material dissolution or parasitic reactions in the diluted electrolyte.

To assess if the columbic efficiency values indeed reflected active material dissolution, inductively coupled plasma spectroscopy (ICP) was employed to quantify the maximum solubility of PbF_2 and Pb in methanol and propionitrile. The results indicate that PbF_2 can dissolve in MeOH up to a concentration of 31.5 ppm (mg L^{-1}), whereas it is insoluble in PN, as it was below the 0.01 ppm detection limit of the experiment (Fig. 4.7-c). Pb also appears to be soluble in MeOH, despite to a lesser degree than PbF_2 (14.6 ppm). It is possible that the observed Pb dissolution arose from Pb acetate traces left in the synthesised powder rather than the metal itself. Similar to PbF_2, Pb was also insoluble in PN. Interestingly, neither Pb nor PbF_2 dissolved in a 5 wt% MeOH – 95 wt% PN mixture (Fig. 4.7-c), which is the same ratio used in 0.5 m TMAF MeOH-PN. Evidently, the low amount of MeOH is not sufficient to provide detectable dissolution.

The ICP results suggest that active material dissolution in the highly concentrated electrolyte should be expected. However, due to the high TMAF concentration in the highly

concentrated electrolyte, the level of active material dissolution is likely lower than what is indicated by ICP. The 10 m concentration entails that roughly two thirds of MeOH molecules are occupied with solvating F-ions and might not be available to dissolve PbF_2. The higher active material dissolution in the highly concentrated electrolyte might be the reason for the inferior capacity retention, since it contains a much higher proportion of MeOH compared to the diluted electrolyte. However, it is difficult to draw definite conclusions given that in symmetric cells, dissolved ions from the active material can plate on the opposite electrode, without it being possible to detect them. Additionally, it is possible that soluble intermediates form during cycling, causing active material dissolution also in the diluted electrolyte, and giving rise to the over 100% coulombic efficiency.

Overall, the reversible cycling of Pb-PbF_2, the excellent capacity retention, and the low overpotential indicate the feasibility of 0.5 m TMAF MeOH-PN as an electrolyte for FIBs.

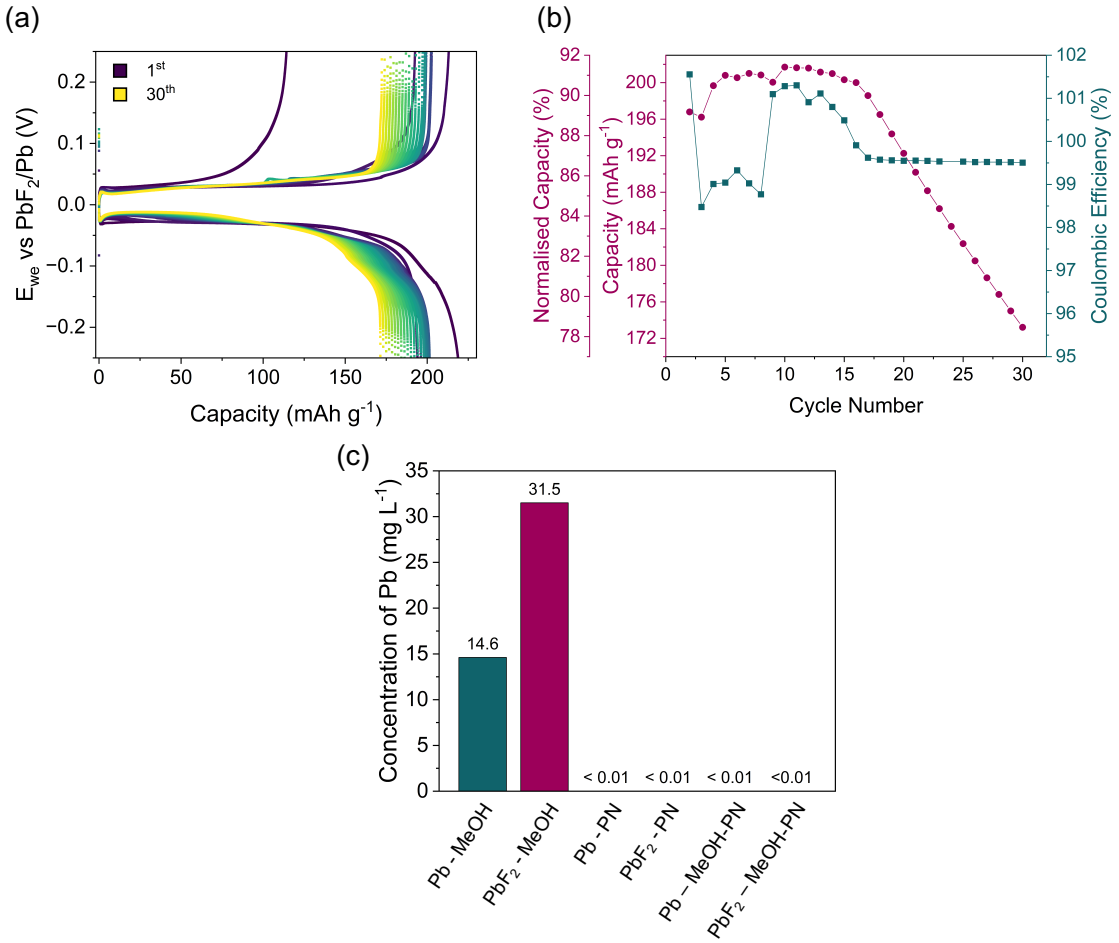


Figure 4.7: **(a)** GCPL plot showing the cycling of a Pb-PbF_2 symmetric cell in 10 m TMAF-MeOH at a C/20 rate (10.9 mA $g^{-1}_{PbF_2}$). **(b)** Capacity, normalised capacity and coulombic efficiency as a function of cycle number for the Pb-PbF_2 symmetric cell. **(c)** ICP showing Pb and PbF_2 dissolution in MeOH but not in PN or a mixture of the two. The ratio in the MeOH-PN mixture is 5 wt% methanol and 95 wt% propionitrile as in the diluted electrolyte.

4.2.7 Cycling of BiF_3 vs Pb-PbF_2 in the diluted electrolyte

The successful cycling of Pb-PbF_2 allowed testing other promising metal fluorides in the diluted electrolyte, and BiF_3 was one of the materials selected for this purpose. BiF_3 is a cathode material that has been widely investigated in liquid electrolyte FIBs, because of its high redox potential (0.24 V vs PbF_2/Pb) and moderately high theoretical capacity (302 mAh g^{-1}). BiF_3 was cycled against the Pb-PbF_2 counter-reference electrode with 0.5 m TMAF MeOH-PN, and its performance compared to what has been previously reported

in the FIB literature. BiF_3 electrodes with 60 wt% active material, 30 wt% carbon, and 10 wt% PTFE were used, whereas the Pb-PbF_2 counter-reference electrode had 65 wt% Pb, 15 wt% PbF_2, 10 wt% carbon, and 10 wt% PTFE. These ratios result in a N:P (negative:positive) ratio of 2.2, which indicates an excess of Pb. This was used to ensure that the cycling of BiF_3 was not limited by the counter-reference electrode. Ball milled BiF_3 powder with an average particle size of ~700 nm was used to fabricate the electrodes.

The diluted electrolyte enabled the reversible cycling of BiF_3. On the first discharge, a capacity of 284 mAh g^{-1} out of the theoretical 302 mAh g^{-1} was achieved, suggesting that most of the BiF_3 was converted to Bi metal (Figure 4.8-a,b). Upon recharge, a considerably lower capacity of 178 mAh g^{-1} was reached, indicating that not all the Bi metal was converted back to BiF_3 (Figure 4.8-a,b).

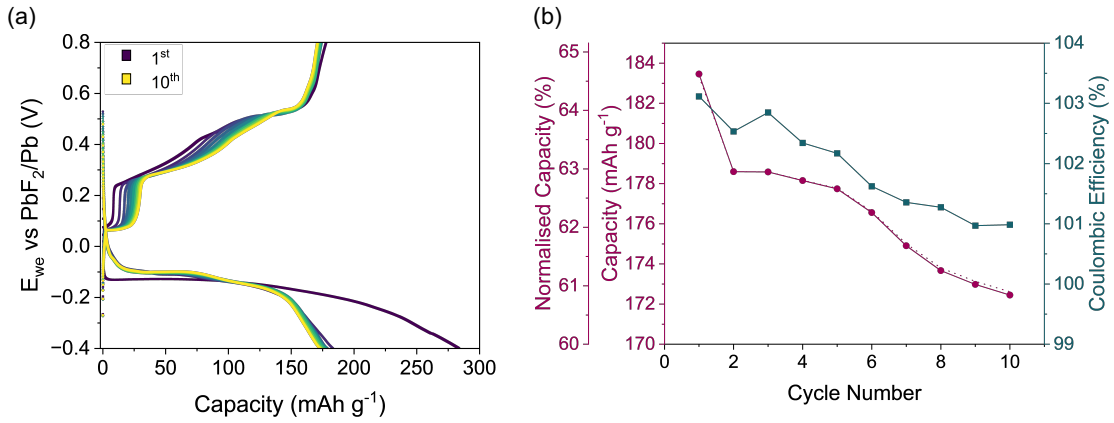


Figure 4.8: BiF_3 cycling performance. **(a)** Cycling of BiF_3 vs the Pb-PbF_2 counter-reference electrode at a rate of C/20 (15.1 mA $g^{-1}_{BiF_3}$). **(b)** Corresponding capacity retention and coulombic efficiency as a function of cycle number.

XRD results confirmed the occurrence of the conversion reaction during cycling. The pristine BiF_3 electrode comprised a mixture of cubic ($Fm\bar{3}m$) and orthorhombic (Pnma) crystal structures. At the end of the first discharge the BiF_3 electrode converted to Bi metal, indicating that the observed capacity arose from the active material conversion (Fig. 4.9-

a,b). On recharge, part of the Bi metal converted back to cubic BiF_3 proving the reversibility of the conversion reaction. However, large peaks corresponding to Bi metal were still visible in the charged state, confirming the lack of full conversion as evident from the lower than theoretical capacity obtained after recharging (Fig. 4.9-c,d). Furthermore, the several additional peaks present in the charged electrode indicate the formation of some unknown phases, possibly some intermediates, which require further investigation (Fig. 4.9-d).

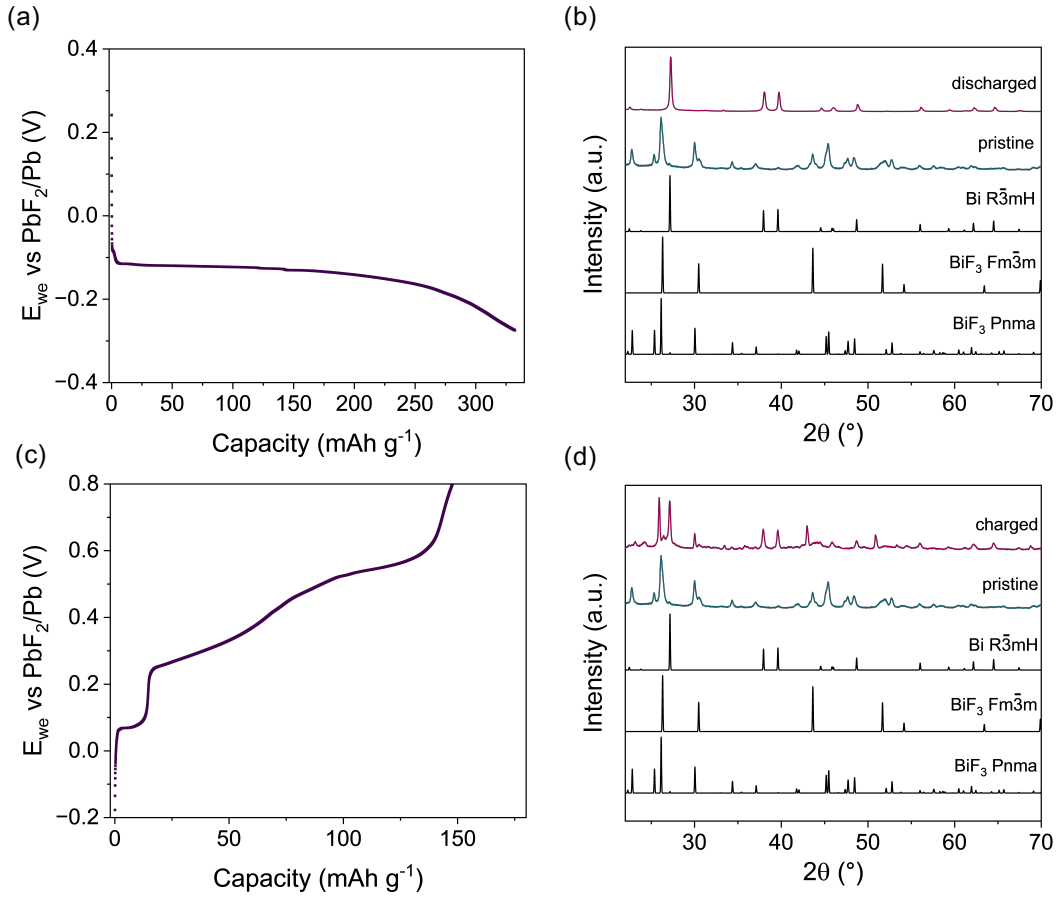


Figure 4.9: XRD of BiF_3 electrodes at different states of charge. **(a)** Discharge profile of a BiF_3 electrode cycled versus Pb-PbF_2 with **(b)** its corresponding XRD demonstrating full conversion. **(c)** Recharged BiF_3 electrode with **(d)** its XRD profile showing additional unknown peaks.

The cycling profile of BiF_3 appears very asymmetric between charge and discharge. The charge profile exhibits three plateaus, a short one at 0.07 V, a second one at 0.27 V and a third one at 0.52 V. The discharge profile displays a unique plateau at -0.12 V. The same

behaviour has been observed by Yaokawa et al.[21] However, in the literature, BiF_3 has also been reported to cycle with a unique plateau on both charge and discharge. The cause of this discrepancy in cycling behaviour among different studies is still not clear and a mechanistic study is required to link each plateau to a specific crystallographic change.

BiF_3 electrodes exhibited excellent reversibility in the diluted electrolyte. Despite not achieving full conversion, BiF_3 reached a capacity retention of 173 mAh g^{-1} (61%) after 10 cycles at a cycling rate of C/20 (Fig. 4.8-b), making this capacity retention the best for BiF_3 in a FIB (Table 4.3). Similar to the Pb-PbF_2 symmetric cell, the coulombic efficiency was over 100% and appeared to plateau at 101% on the 9^{th} cycle, suggesting the occurrence of minor degradation processes (Fig. 4.8-b). The reversible cycling of BiF_3 further proved the suitability of the diluted electrolyte to cycle metal fluorides in FIBs.

Table 4.3: Cycling performance of BiF_3. The performance reported in this work (first row) is compared to what has been previously reported in the FIB literature for BiF_3. The values in red highlight the parameters that are better in this work compared to the literature.

Set-up	CE	Cycling rate	1st discharge capacity (mAh g^{-1})	1st charge capacity (mAh g^{-1})	Capacity retention 10th cycle (mAh g^{-1})	Reference
coin cell	Pb-PbF_2	**C/20**	284	180	**173**	this work
flooded cell	Pt	C/40	316	218	~140	105
flooded cell	Pt	C/40	427	239	119	106
coin cell	Mg	N/A	140	55	25	107
flooded cell	Pt	C/40	312	220	~10	40
flooded cell	Pt	C/40	228	180	N/A	39
flooded cell	Pt	C/40	340	117	N/A	23
flooded cell	Pt	C/40	215	100	N/A	108
flooded cell	Pt	C/40	319	82	N/A	109
2-electrode cell	Pb	C/360	110	60	N/A	21

4.2.8 Cycling of CuF_2 vs Pb-PbF_2 in the diluted electrolyte

BiF_3 was reversibly cycled in the 0.5 m TMAF MeOH-PN electrolyte. However, BiF_3 is not the most promising cathode material because its high density reduces the gravimetric energy density achievable. CuF_2, on the other hand, is the most promising binary fluoride as a cathode material for FIBs due to its high theoretical capacity (527 mAh g^{-1}) and redox potential (~0.6 V vs PbF_2/Pb). Because of its appeal, the cycling capability of CuF_2 in the diluted electrolyte was investigated.

Unfortunately, CuF_2 proved to be soluble in the electrolyte and it was not possible to cycle it reversibly. Upon disassembly of the cells, it was evident that Cu metal had plated on the counter electrode during cycling (Fig. 4.10). This does not come to a surprise since CuF_2 is known to be soluble in alcohols and slightly in water, whereas Cu metal is known to dissolve in aqueous solutions of acetonitrile, which might also apply to propionitrile.[110] The diluted electrolyte is therefore not suitable for the cycling of CuF_2.



Figure 4.10: Cu^{2+} ions dissolved into the electrolyte and reduced on the surface of the counter-reference electrode.

4.3 Conclusion and Future Work

This chapter has presented a novel approach to design liquid electrolytes for FIBs by utilising a highly concentrated electrolyte with the addition of a diluent. The use of a high salt concentration mitigates the drawbacks of a protic solvent, whereas the introduction of a diluent reduces the high viscosity and the impractically large amounts of salt required in highly concentrated electrolytes.

The addition of propionitrile as the diluent improved the performance of the highly concentrated electrolyte. The reduced viscosity in the diluted electrolyte led to a one order of magnitude increase in the diffusion coefficient of F-ions, while the ionic conductivity remained high. Additionally, the capacity retention of Pb-PbF_2 cells was significantly

improved with the diluted electrolyte. Meanwhile, the wider electrochemical stability window of the highly concentrated electrolyte was retained upon the addition of the diluent.

This electrolyte also allowed to cycle reversibly not only the Pb-PbF_2 electrodes introduced in Chapter 3, but also full cells of BiF_3 vs Pb-PbF_2. In both cases, nearly full conversion of the active material and excellent capacity retention could be achieved. However, possible active material dissolution could be detected from the higher than 100% coulombic efficiency. Unfortunately, CuF_2 could not be cycled in the diluted electrolyte due to major active material dissolution.

Further work is required to investigate the conversion mechanism of the active materials used. Regarding the Pb-PbF_2 electrodes, it is necessary to determine what factors trigger the change from β-PbF_2 to α-PbF_2. Additionally, it would be important to establish whether soluble intermediates form during cycling. As for the BiF_3, more work is required to identify all the peaks visible in the XRD pattern upon recharge and verify whether the recognised structures match the BiF_3 conversion mechanism reported in the FIB literature. All this information could be obtained by carrying out an *in-situ* XRD study using the coin cell set-up proposed in this work.

To enhance performance, a range of optimisations could be implemented for this electrolyte. First, it would be worth investigating lower concentrations of propionitrile and their effect on the solvation shell of F-ions and on the properties of the electrolyte, to select the concentration that gives the best performance. Second, it would be worth investigating whether it is possible to reduce the water content in the synthesised tetramethylammonium fluoride even further by using ultra-high vacuum during the drying step. This would further reduce the chances of having parasitic reactions.

Additionally, it would be interesting to search for alternative solvents that could provide improved performance. Particularly, protic solvents that could achieve a wider electrochemical stability window than methanol in the highly concentrated solution. This would allow to have a wider range of electrodes that could be tested with the electrolyte. Another avenue for improvement would be identifying a different diluent that retains most of the properties of propionitrile but has a lower dielectric constant. A lower dielectric constant might reduce the interaction between the diluent and F-ions and perform more closely to an ideal diluent. Finally, the most important improvement, despite possibly being the most complicated to achieve, would be to select both a protic solvent and a diluent that do not cause active material dissolution, particularly of CuF_2. This would achieve an improved and more realistic cycling performance.

In the next chapter, I present a different strategy to design liquid electrolytes for FIBs, which involves the use of ionic liquids rather than organic solvents.

Chapter 5

A Chemically Stable Ionic Liquid-Based Electrolyte

Table of Contents

5.1 Introduction 111

5.2 Results and Discussion 112

5.2.1 Selection process for the ionic liquid 112

5.2.2 Solvation of F^- in the two ionic liquids 114

5.2.3 Chemical stability of the two electrolytes 117

5.2.4 Transport and electrochemical properties 124

5.2.5 Cycling of 0.3 m TMAF-DMIM TFSI with Pb-PbF_2 electrodes 128

5.2.6 Purification of DMIM TFSI 131

5.3 Conclusion and Future Work 134

5.1 Introduction

In the previous chapter, the concept of a diluent, capable of improving the properties of a highly concentrated electrolyte, was reported for the first time in the FIBs field. In this chapter, a different strategy is used to propose another novel liquid electrolyte for FIBs. Rather than focusing on obtaining high F-ion solubility as in the previous chapter, the design strategy presented here aims at achieving true chemical stability over time. Only one study in the FIBs literature has attempted to attain chemical stability in a liquid electrolyte, and it did not succeed.[47] Chemical stability (especially without HF formation) is extremely important to the success of FIBs. Even if great cycling performance were to be achieved, the presence of HF in liquid electrolytes would exclude FIBs from any practical applications due to safety concerns.

It is particularly challenging to achieve chemical stability in FIBs due to the high reactivity of F-ions. Free F-ions act as very strong Lewis bases which quickly react with Lewis acids to form the corresponding fluoro anions. When good fluoride acceptors are not

available, F-ions can extract even firmly bound protons, as in the case of acetonitrile (CH_3CN).[93] Achieving chemical stability is further complicated by the presence of β-hydrogens in the majority of solvents and salts used in batteries. These acidic protons are particularly susceptible to fluoride attack, as discussed in the general introduction (Chapter 1).

In this chapter I characterise the chemical stability, transport properties and electrochemical performance of a novel ionic liquid electrolyte containing tetramethylammonium fluoride (TMAF) as the salt, and 1,3-dimethylimidazolium bis(trifluoromethane)sulfonimide (DMIM TFSI) as the ionic liquid. I then test the cycling performance of this novel electrolyte in the Pb-PbF_2 symmetric coin cell introduced in Chapter 3.

All the work in this chapter was performed by me under the supervision of Prof. Mauro Pasta. Exceptions are the collection of the NMR data for the chemical stability over time done by Omar Alshangiti, and the measurement of the diffusion coefficient via pfg-NMR which was done by Dr Gregory Rees.

5.2 Results and Discussion

5.2.1 Selection process for the ionic liquid

Designing ionic liquid-based electrolytes for FIBs presents two main challenges. The first is selecting an ionic liquid (IL) without β-Hs (to avoid HF formation), as most ionic liquids require large sized cations and/or anions to be liquid at room temperature.[111] The second challenge is to find an ionic liquid capable of solvating the F-ion.

Among the ILs commercially available, four lacking β-Hs could be found. These have all imidazolium-based cations and bis(trifluoromethanesulfonyl)imide (TFSI) anions,

namely 1,3-dimethoxyimidazolium TFSI, 1,3-dimethoxy-2-methylimidazolium TFSI, 1-benzyl-3-methylimidazolium TFSI and 1,3-dimethylimidazolium TFSI (Fig. 5.1).

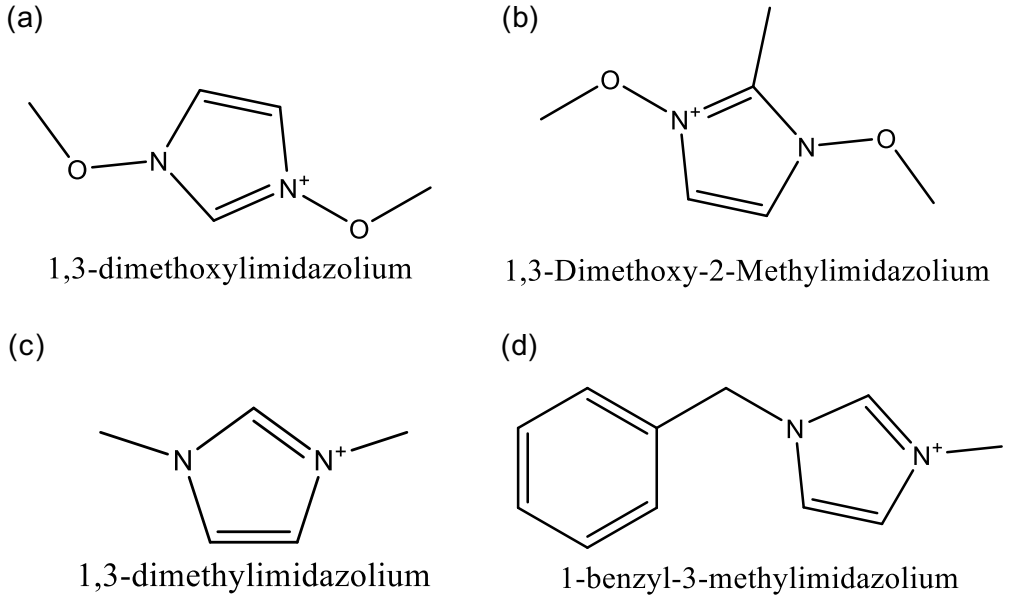


Figure 5.1: Imidazolium-based cations of the ionic liquids tested. All these cations do not contain β-hydrogens.

To test the compatibility of TMAF with these ionic liquids, the salt was mixed with each of the selected ILs, which had previously been dried. TMAF was used because of its numerous advantages as already described in Chapter 4, especially for its chemical stability. Among the four ILs tested, two did not exhibit any compatibility with TMAF. When the 1,3-dimethoxyimidazolium TFSI made contact with the TMAF a violent reaction occurred, which caused some TMAF to fly out of the vial and resulted in the formation of two separate solid phases, an orange and a black one (Fig. 5.2-a). Clearly, this outcome indicates the lack of chemical stability between the two compounds and the unsuitability of 1,3-dimethoxyimidazolium TFSI to be used in an electrolyte for FIBs. 1,3-dimethoxy-2-methylimidazolium TFSI did not provoke such a strong reaction but the orange extremely viscous gel that arose immediately upon mixing also indicates the unsuitability of this IL (Fig. 5.2-b). Hence, both compounds were discarded as viable options and not included in

any further analysis. These two unstable ILs differ from the other two candidates due to the presence of methoxyl groups attached to the nitrogens of the imidazolium ring. It is therefore plausible to speculate that the methoxyl groups are the cause of the observed chemical instability.

On the other hand, both 1-benzyl-3-methylimidazolium TFSI (BMIM TFSI) and 1,3-dimethylimidazolium TFSI (DMIM TFSI) did not cause any unexpected reactions and appeared to be capable of dissolving TMAF. The two electrolytes originating from these ILs have a yellow colour and TMAF-BMIM TFSI appears to be considerably more viscous than TMAF-DMIM TFSI. This is consistent with the four times higher viscosity of BMIM TFSI (153 cP) compared to DMIM TFSI (37.1 cP), arising from the larger size of the cation.[112–114]

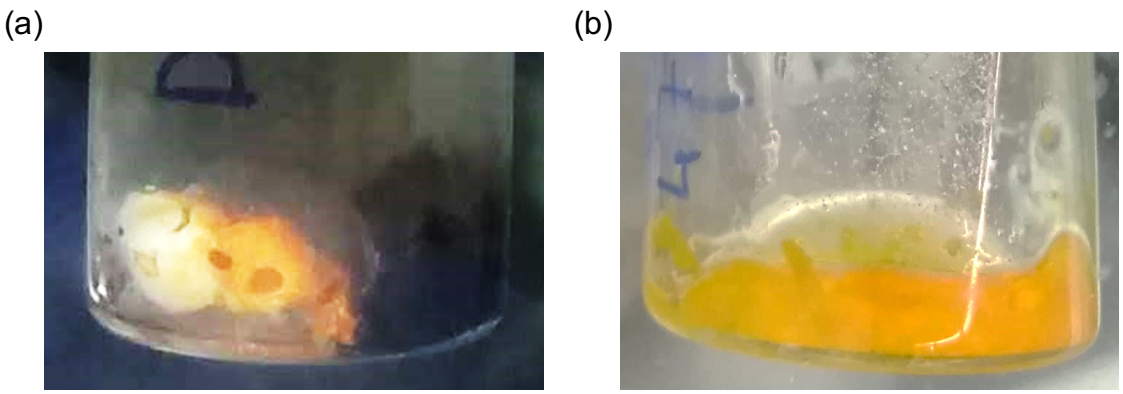


Figure 5.2: Results of contact between TMAF and the two unstable ionic liquids. **(a)** A black and an orange phase originated from the reaction between TMAF and 1,3-dimethoxyimidazolium TFSI. **(b)** A viscous orange gel arose from the reaction between TMAF and 1,3-dimethoxy-2-methylimidazolium TFSI. Both ionic liquids were discarded from any further analysis as they are not stable in contact with TMAF.

5.2.2 Solvation of F^- in the two ionic liquids

To assess whether either of the two abovementioned ionic liquids is suitable to produce a liquid electrolyte for FIBs, the first step was to measure the extent of solubility of the fluoride salt (TMAF) in both DMIM TFSI and BMIM TFSI. To accomplish this, ^1H

NMR was used to measure the maximum concentration of TMAF in a saturated solution of DMIM TFSI and BMIM TFSI. The appearance of an additional peak at 3.3 ppm in the proton NMR spectrum of the two electrolytes (Fig. 5.3-b,d), which corresponds to TMA^+, confirms the solubility of TMAF in both DMIM TFSI and BMIM TFSI. Specifically, the maximum concentration of TMAF was found to be 0.3 m (~0.5 mol L^{-1}) in DMIM TFSI and 0.2 m (~0.3 mol L^{-1}) in BMIM TFSI. Both ILs, but especially DMIM TFSI, achieve among the highest solubilities ever reported in the FIBs literature for nonaqueous organic electrolytes (<0.5 mol L^{-1} fluoride solubility with anion acceptors).[68]

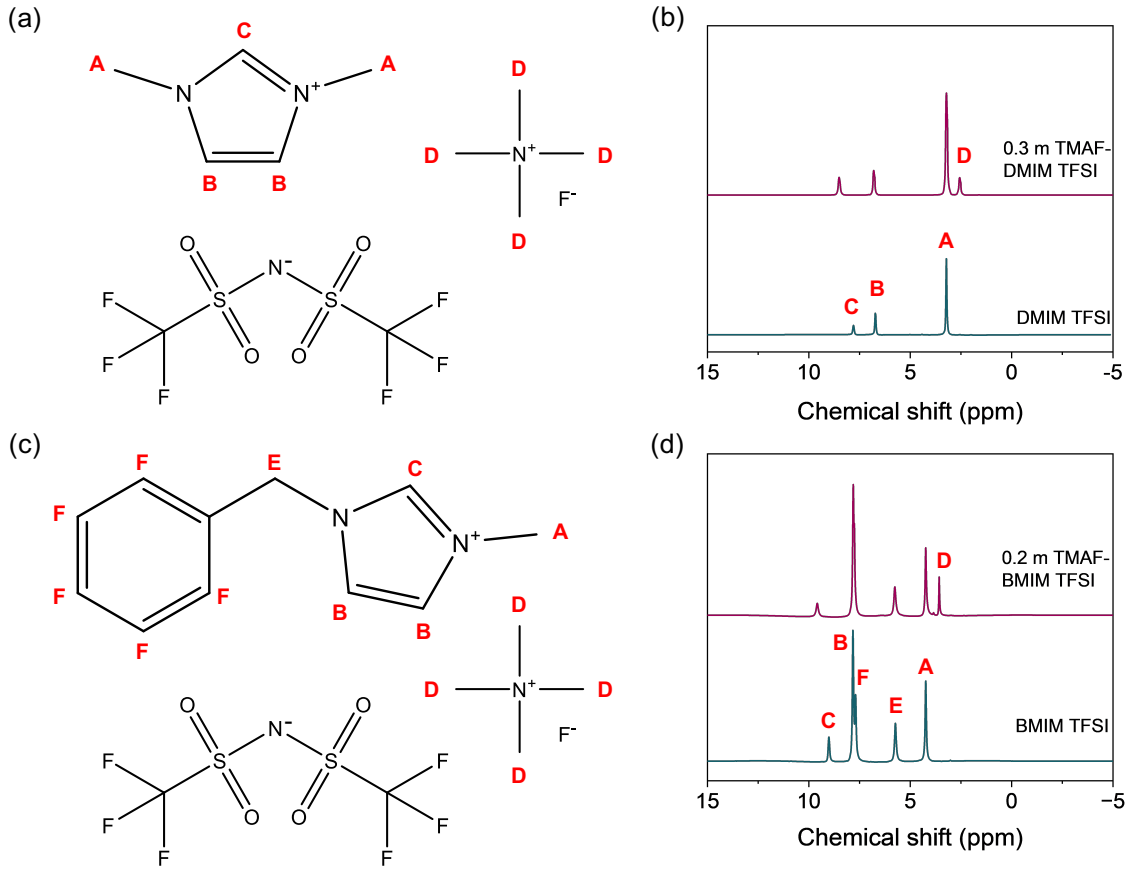


Figure 5.3: ^{1}H NMR of the two electrolytes. **(a)** Structure of TMAF-DMIM TFSI with the protons labelled to match the peaks in **(b)** the corresponding ^{1}H NMR spectrum. **(c)** Structure of TMAF-BMIM TFSI with the protons labelled to match the peaks in **(d)** the corresponding ^{1}H NMR spectrum. The appearance in both electrolytes of the peak "D" corresponding to TMA^+ confirms the solubility of TMAF in the two ionic liquids.

With TMAF's solubility established in both ILs, the focus shifted to examining how DMIM TFSI and BMIM TFSI solvate the F-ions. ^{1}H NMR indicates a preferential solvation of fluoride ions by both DMIM TFSI and BMIM TFSI. A more pronounced shift to high frequencies is observed for the peak corresponding to the second hydrogen on the imidazolium ring, (labelled "C") upon addition of TMAF to the ILs. Particularly, a 0.7 and ~0.6 ppm shift to higher frequency of this peak is observed in 0.3 TMAF-DMIM TFSI and 0.2 m TMAF-BMIM TFSI, respectively (Fig. 5.4) This suggests that the hydrogen “C” is primarily responsible for the solvation of the fluoride ion in both ILs, which is likely caused by the higher acidity of this hydrogen compared to the others.[115]

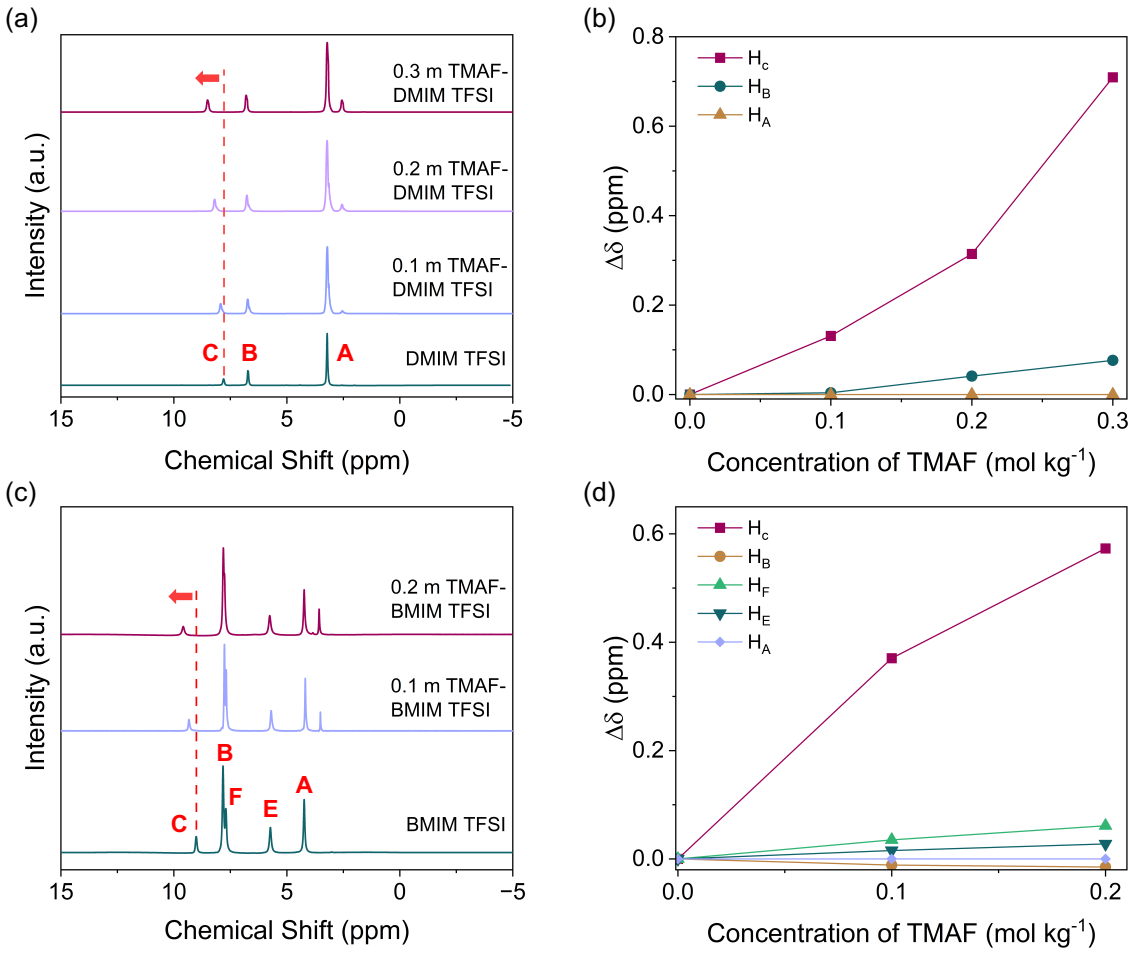


Figure 5.4: Solvation of F^- in the imidazolium-based ionic liquids. **(a)** Increasing TMAF concentration shifts the "C" proton peak in TMAF-DMIM TFSI towards higher frequencies, which reaches **(b)** 0.7 ppm at 0.3 m (H_C). **(c)** Same phenomenon occurs in TMAF-BMIM TFSI, in which the shift towards higher frequencies reaches a maximum of **(d)** ~0.6 ppm at 0.2 m. The observed shift indicates that F-ions are solvated by the "C" hydrogen of the imidazolium ring.

5.2.3 Chemical stability of the two electrolytes

Despite enabling the solvation of the F-ion, the acidity of the second proton on the imidazolium ring might be a cause of concern due to the potential for hydrogen abstraction and HF formation. Huang et al. have argued against this possibility and demonstrated the thermodynamic and kinetic stability of imidazolium fluoride. In particular, they have shown the unfavourableness of the proton transfer reaction to form HF.[116]

To verify the lack of HF formation in the two electrolytes, and further validate the findings of Huang et al., the chemical stability of 0.3 m TMAF-DMIM TFSI and 0.2 m TMAF-BMIM TFSI was investigated. ^{19}F NMR was used for this purpose. Contrary to expectations the ^{19}F NMR spectrum of both electrolytes (Fig. 5.5-a,b) shows two additional peaks compared to the pure ionic liquids. The peak at -75 ppm corresponds to the solvated F^-, whereas the doublet at -140 ppm arises from the bifluoride anion (HF_2^-). The presence of HF_2^- is further confirmed by a triplet at ~16 ppm in the proton NMR of both electrolytes (Fig. 5.5-c). The presence of HF_2^-, which arises from the further reaction of HF and F^-, appears to indicate the occurrence of a side reaction in the two electrolytes.[117–120]

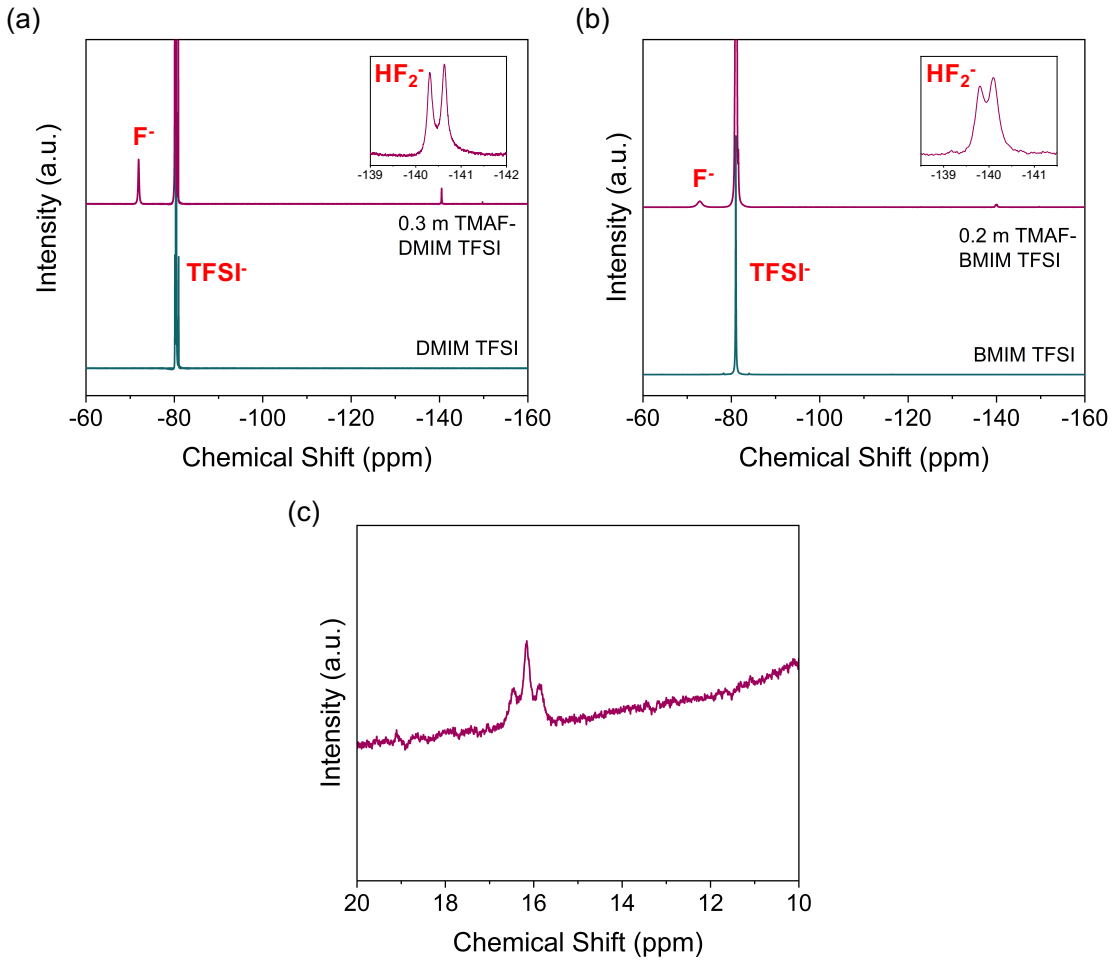


Figure 5.5: Appearance of HF_2^-. **(a)** and **(b)** display the ^{19}F NMR of 0.3 m TMAF-DMIM TFSI and 0.2 m TMAF-DMIM TFSI, respectively, exhibiting an additional doublet at -140 ppm corresponding to HF_2^-. The presence of HF_2^- in the two electrolytes is confirmed by **(c)** the appearance of triplet at 16 ppm in the ^1H NMR.

Further tests were run to investigate the origin of the HF_2^-. The objective was to assess whether the second proton on the imidazolium ring is indeed the culprit, or rather if an impurity in either the fluoride salt or ionic liquid is responsible. The latter option seems plausible given that the purity of both ionic liquids is only 99%, which is well below the standard for battery applications (Fig. 5.6). Since the potential degradation mechanism is the same for both ionic liquids, DMIM TFSI was selected to carry out the HF_2^- investigation.

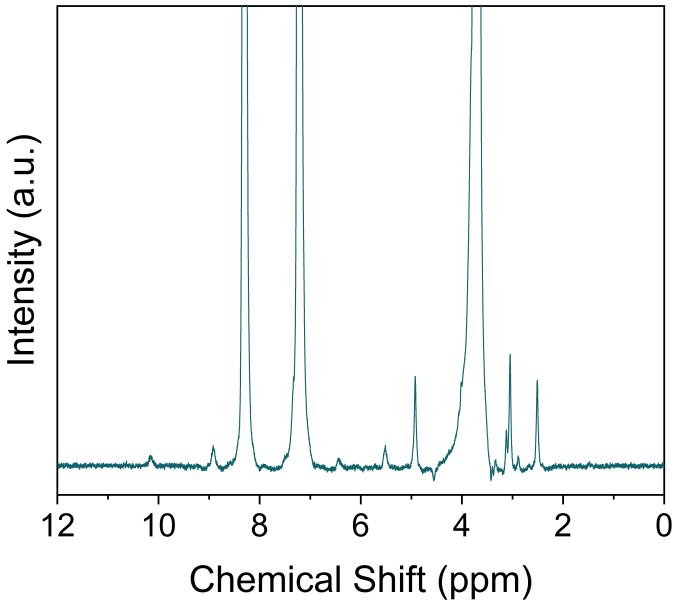


Figure 5.6: Impurities in DMIM TFSI. Zoomed in view of the ^{1}H NMR for DMIM TFSI displaying several additional peaks ascribable to unknown impurities (rather than to the IL itself).

In the first test, the concentration of HF_2^- in DMIM TFSI was monitored over time and compared to the HF_2^- evolution in an electrolyte known to degrade over time. TMAF in N-propyl-N-methylpyrrolidinium bis(fluorosulfonyl)imide (Pyr_{13} FSI) was chosen as the reference electrolyte as it contains β-Hs, and it is therefore expected to form HF_2^- and degrade over time. The concentration of HF_2^- in TMAF- Pyr_{13} FSI kept increasing over time (Fig. 5.7). After 113 days the proportion of HF_2^- with respect to F^- reached 54%, indicating that more than half of F-ions had turned into HF_2^-. This behaviour was not observed for TMAF-DMIM TFSI. The proportion of HF_2^- with respect to F^- in TMAF-DMIM TFSI remained constant at 7% for over 50 days indicating no ongoing degradation (Fig. 5.7). If the amount of HF_2^- was growing over time in TMAF-DMIM TFSI (as in the case of the other electrolyte), this would have been conclusive proof that the ionic liquid is the cause of HF_2^-, rather than an impurity. However, the constant amount of HF_2^- indicates the occurrence of either of these two scenarios. One possibility is that an impurity is

responsible for the HF_2^- formation. If this is the case, the impurity gets depleted immediately upon addition of TMAF giving rise to the observed HF_2^- concentration and explaining the lack of growth over time. The other possibility is that DMIM TFSI is the cause of HF_2^- and the lack of increase over time can be ascribed to an equilibrium in the reaction between F^- and HF_2^-, which prevents further generation of HF_2^-. A further test was run to establish which one of these two scenarios occurred.

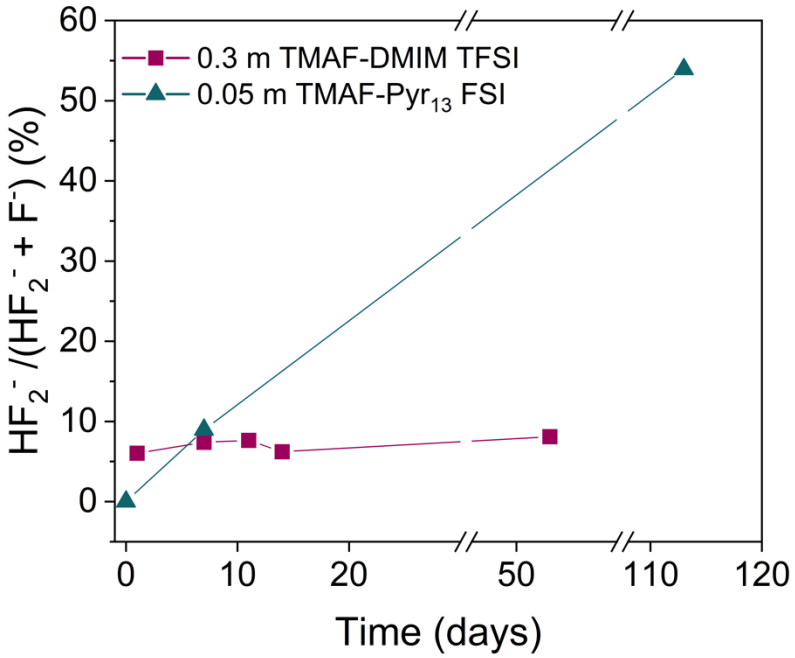


Figure 5.7: Ratio between the concentration of HF_2^- and that of F^- as a function of time. The concentration of HF_2^- increases over time in the β-H containing electrolyte (0.05 m TMAF-Pyr_{13} FSI), whereas it remains constant in 0.3 m TMAF-DMIM TFSI.

To establish whether an impurity or the ionic liquid caused the observed HF_2^-, a second test was run to investigate how the concentration of F-ions affected the amount of HF_2^-. To do so, the concentration of TMAF-DMIM TFSI was decreased from 0.3 to 0.1 m and the quantity of HF_2^- measured again. The results show that the proportion of HF_2^- with respect to the anion of the ionic liquid ($TFSI^-$), whose amount was almost unaffected by the change in TMAF concentration, stays constant regardless of the change in TMAF

concentration (Fig. 5.8-a). At the same time, the proportion of HF_2^- with respect to F^- increased to 26% (at 0.1 m) from 7% (at 0.3 m) (Fig. 5.8-b), as a result of the HF_2^- concentration remaining the same and the F^- concentration decreasing. These results show that HF_2^- does not scale with TMAF concentration, indicating that HF_2^- formation is not limited by the concentration of F-ions in the electrolyte but rather by the amount of the proton responsible for HF_2^-. This is the conclusive proof that an impurity is the cause of the observed HF_2^- rather than the acidic proton of the imidazolium ring. In fact, the proton of the ionic liquid is present in a much higher concentration than F-ions and therefore cannot be the limiting factor to the HF_2^- formation. The results of this second test also indicates that the impurity causing the formation of HF_2^- is not present in the TMAF but rather in the ionic liquid, as otherwise the amount of HF_2^- would scale with salt concentration.

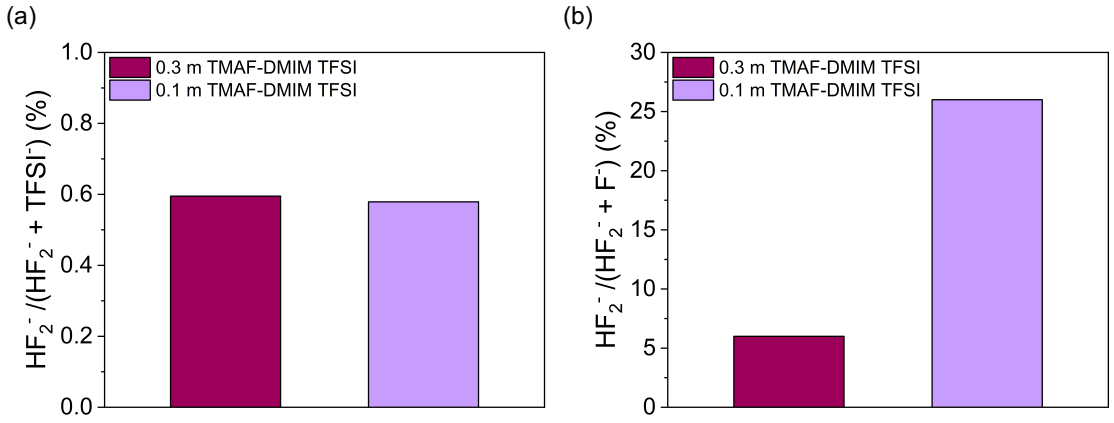


Figure 5.8: Effect of TMAF concentration on HF_2^- content. Proportion of HF_2^- with respect to **(a)** $TFSI^-$ and **(b)** F^-, as a function of TMAF concentration. The overall concentration of HF_2^- remains the same regardless of the TMAF concentration.

Okazaki et al. also observed HF_2^- in their liquid electrolyte. They ascribed its presence to the existence of trace amount of water in the electrolyte.[121] However, given the that their electrolyte contained β-hydrogens, this seems a much more plausible cause for the observed HF_2^- formation. If water was indeed causing HF_2^-, increasing the water content

should lead to a growth in the HF_2^- concentration. They did not perform this test, but in the present work this hypothesis was tested by increasing the water content in TMAF by four times and by measuring whether the HF_2^- concentration grew. Fig. 5.9 shows that the four-time higher water content in the electrolyte (purple circles in Fig. 5.9) did not lead to any change in the proportion of HF_2^- with respect to F-ions, indicating that trace amount of water does not affect the concentration of HF_2^- in the electrolyte. These results do not only disproof the claim by Okazaki et al. but also confirm that water impurities are not causing the observed HF_2^- in TMAF-DMIM TFSI and a different unknown impurity in the ionic liquid is the cause. Further discussion on the nature of this impurity is present in section 5.2.6.

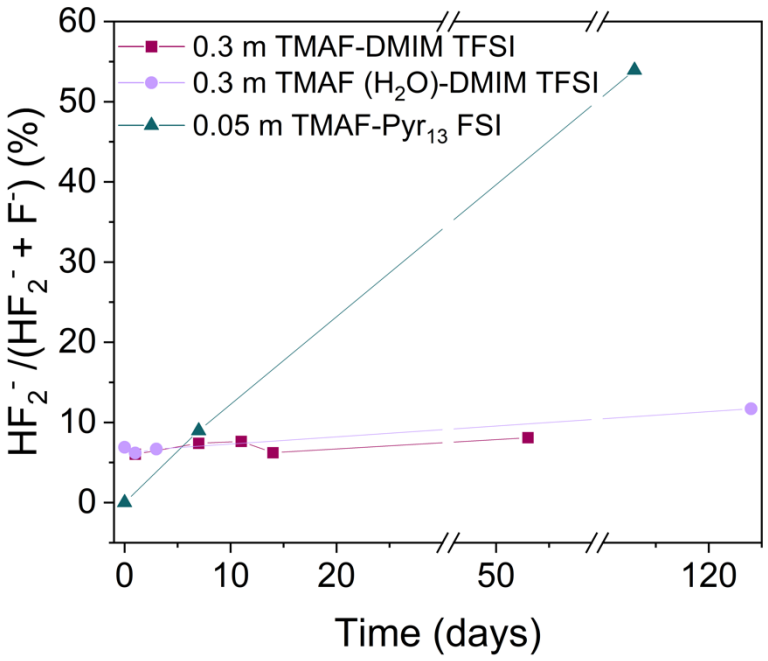


Figure 5.9: Effect of water impurities on HF_2^- content. A four times increase in the water content (0.3 m TMAF (H_2O)-DMIM TFSI) did not affect the HF_2^- concentration compared to 0.3 m TMAF-DMIM TFSI, especially over the first week.

These tests have demonstrated the chemical stability of the imidazolium-based ionic liquids towards F-ions attack, confirming the findings of Huang et al. TMAF-DMIM TFSI

and TMAF-BMIM TFSI are therefore chemically stable over time and the observed HF_2^- is caused by an impurity in the ionic liquids, which are only 99% pure.

5.2.4 Transport and electrochemical properties

After establishing the chemical stability of the ILs towards F-ions, the suitability of TMAF-DMIM TFSI and TMAF-BMIM TFSI as liquid electrolytes for FIBs was tested. Specifically, the ionic conductivity, diffusion coefficients and electrochemical stability window were measured.

Ionic conductivity follows a similar trend in both electrolytes. It decreases with increasing TMAF concentration (Fig. 5.10), matching the typical pattern of ionic liquid electrolytes. This behaviour has already been observed in LIBs and can be ascribed to a higher viscosity at higher salt concentrations.[122] The highest ionic conductivity is therefore observed for the 0.1 m concentration, with values of 6.2 mS cm^{-1} and 0.76 mS cm^{-1} for DMIM TFSI and BMIM TFSI, respectively. On the other hand, the lowest ionic conductivity of 3.8 mS cm^{-1} and 0.73 mS cm^{-1} is reached at the highest concentrations of 0.3 m (for DMIM TFSI) and 0.2 m (for BMIM TFSI), respectively. Not surprisingly, the high viscosity of BMIM TFSI (153 cP) results in a considerably lower ionic conductivity, making TMAF-DMIM TFSI the most promising electrolyte for FIBs. In fact, even the lowest ionic conductivity of 3.8 mS cm^{-1} for 0.3 m TMAF DMIM TFSI is higher than that of many electrolytes reported in the FIB literature and sufficient to provide good electrolyte performance.[45–47]

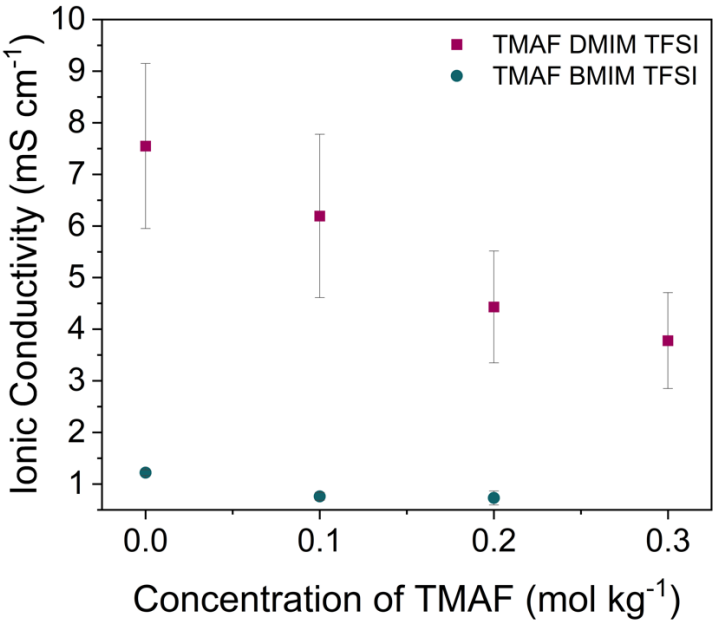


Figure 5.10: Trends in ionic conductivity as a function of TMAF concentration for TMAF-DMIM TFSI and TMAF-BMIM TFSI. In both electrolytes the ionic conductivity decreases with increasing TMAF concentration.

To better assess performance, in addition to ionic conductivity, the self-diffusion coefficient of the different ions in the two electrolytes was measured. In LIBs, the self-diffusion coefficient generally has a similar trend to that of ionic conductivity, that is, decreasing with increasing concentration and viscosity.[122] In TMAF-DMIM TFSI, this trend is observable (although not very pronounced) for $DMIM^+$, TMA^+, $TFSI^-$ and HF_2^- (Fig. 5.11-a). Surprisingly, though, the diffusion coefficient for the F-ion (D_F^-) has the opposite behaviour. It is ~0 $m^2\ s^{-1}$ at the lowest concentrations of 0.1 and 0.2 m and it increases up to 3.2 x 10^{-11} $m^2\ s^{-1}$ at 0.3 m. It is worth noticing that the diffusion coefficient of F-ions at 0.3 m (3.2 x 10^{-11} $m^2\ s^{-1}$) is higher than that of HF_2^- (2.8 x 10^{-11} $m^2\ s^{-1}$), suggesting that F-ions might be the main charge carrier during cycling. The increase in diffusion coefficient at 0.3 m for F-ions could indicate a change in solvation structure at higher concentrations that enables faster diffusion. In fact, the F-ion peak in the ^{19}F NMR becomes narrower in the 0.3 m concentration (0.27 ppm) compared to the 0.1 m (0.74 ppm)

(Fig. 5.11-b), suggesting a more mobile F-ion.[123] However, further investigation is required to understand this phenomenon.

A similar behaviour is observed for TMAF-BMIM TFSI, even though F-ions are not mobile at any concentration. In TMAF-BMIM TFSI, the diffusion coefficient for $TFSI^-$ and HF_2^- decreases when the TMAF concentration increases from 0.1 m to 0.2 m, whereas the diffusion coefficient for F^- is ~0 $m^2\ s^{-1}$ at both concentrations (Fig. 5.11-c). The lack of increase in D_{F^-} suggests that the change in solvation structure observed at 0.3 m TMAF-DMIM TFSI does not occur with BMIM TFSI, possibly due to the lower TMAF solubility. This behaviour is confirmed by the large width (1.31 ppm) of the F^- peak at 0.2 m TMAF-BMIM TFSI (Fig. 5.11-d). This value is even higher than the widest F^- peak in TMAF-DMIM TFSI (0.74 ppm at 0.1 m), suggesting an even lower mobility in BMIM TFSI. The higher viscosity of BMIM TFSI compared to DMIM TFSI, which also resulted in a lower ionic conductivity, affected the diffusion coefficients. In fact, even though both $TFSI^-$ and HF_2^- ions are mobile, their diffusion coefficients are lower than the same ions in DMIM TFSI.

These results strongly indicate that DMIM TFSI performs better than BMIM TFSI, given the higher diffusion coefficients for all anions and the higher TMAF solubility which enables F-ions mobility at 0.3 m. Among the different concentrations of TMAF-DMIM TFSI, 0.3 m TMAF-DMIM TFSI is the electrolyte that performed the best due to the highest D_{F^-} of 3.2 x 10^{-11} $m^2\ s^{-1}$ and a high ionic conductivity of 3.8 mS cm^{-1} and was therefore chosen to cycle Pb-PbF_2 electrodes.

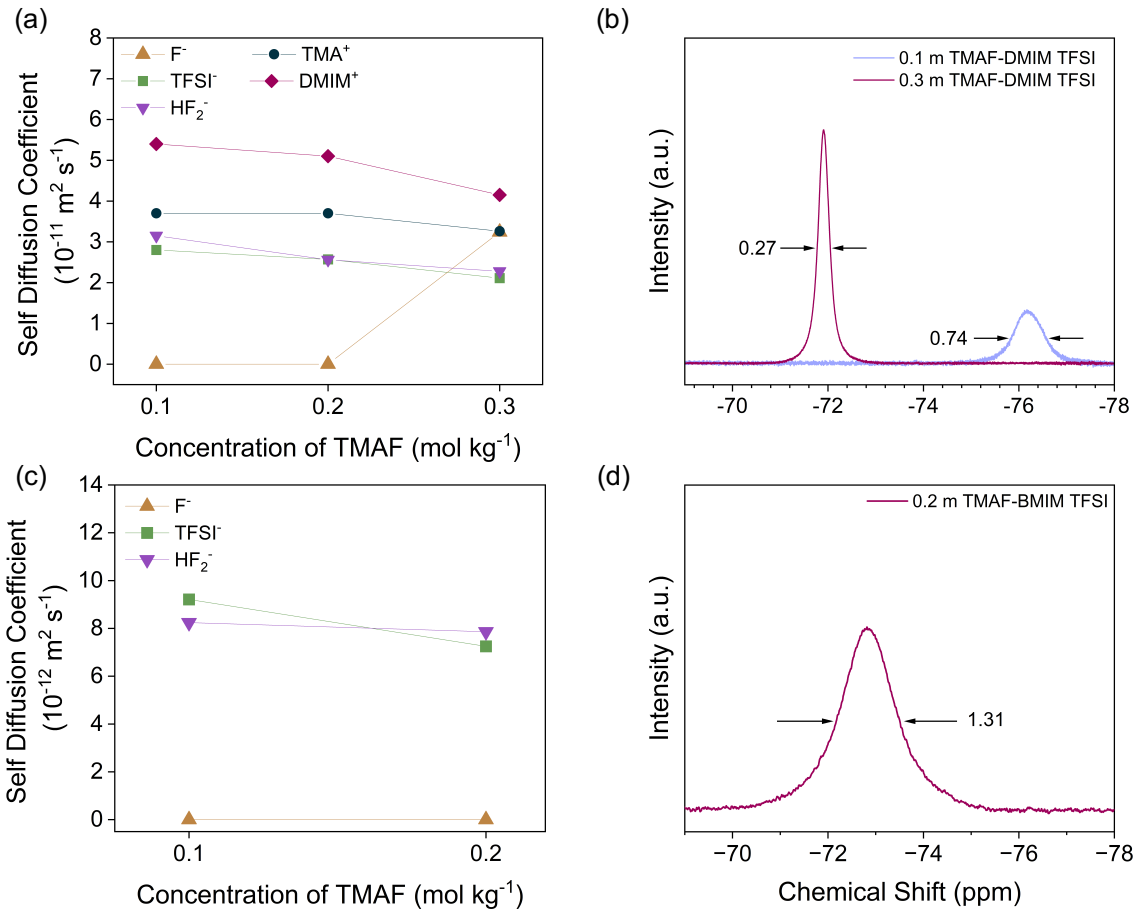


Figure 5.11: Ion diffusion in TMAF-DMIM TFSI and TMAF-BMIM TFSI. **(a)** Self-diffusion coefficients of the ions in TMAF-DMIM TFSI as a function of TMAF concentration. **(b)** Decrease in FWHM of F^- peak in ^{19}F NMR (from 0.74 ppm at 0.1 m to 0.27 ppm at 0.3 m). **(c)** Self-diffusion coefficients of the ions in TMAF-BMIM TFSI as a function of TMAF concentration. **(d)** FWHM of F^- peak in 0.2 m TMAF-BMIM TFSI. The 1.31 ppm width is larger than the widest F^- peak in (b). The diffusion coefficients were measured at 30°C with pfg-NMR.

To determine what electrodes can be cycled in this electrolyte, the electrochemical stability window (ESW) was measured using linear sweep voltammetry (LSV) with a glassy carbon working electrode, a Ag wire counter electrode and a Pb-PbF_2 counter-reference electrode. The ESW for 0.3 m TMAF-DMIM TFSI is 3.14 V wide (cut-off of 100 µA cm^{-2}) with an anodic limit of 2.16 V and a cathodic limit of -0.98 V vs PbF_2/Pb (Fig. 5.12-a). The low reductive stability arises from the high reactivity of the second proton in the imidazolium ring, which is known to lend imidazolium-based ionic liquids a narrower

ESW compared to pyrrolidinium-based ionic liquids.[115] Whereas the oxidative limit cannot be ascribed to the ionic liquid (Fig. 5.12-b) nor TMAF (the peak did not appear in the diluted electrolyte) and was attributed to some unknown impurity. The ESW of TMAF-DMIM TFSI is wider than that of several electrolytes reported in the FIB literature and allows to cycle all the most promising cathode materials.[23,39] Unfortunately, the lack of stability at low potentials prevents the cycling of the most promising anode materials and therefore large redox pairs (e.g., CuF_2 vs Ca). Nonetheless, the redox potential of PbF_2/Pb lies well within the ESW of TMAF-DMIM TFSI allowing for the electrochemical testing of this electrolyte using the Pb-PbF_2 electrodes presented in Chapter 3.

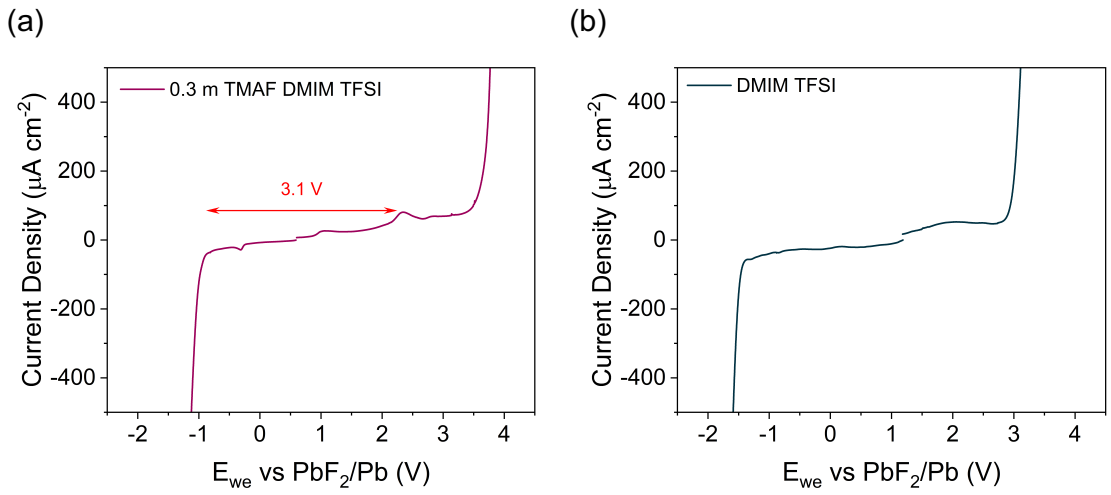


Figure 5.12: Electrochemical stability window of **(a)** 0.3 m TMAF-DMIM TFSI and **(b)** DMIM TFSI. The ESW of the electrolyte is 3.1 V if a 100 µA cm^{-2} cut-off is used, due to the presence of an oxidative peak at 2.5 V vs PbF_2/Pb, which is not present in the pure ionic liquid.

5.2.5 Cycling of 0.3 m TMAF-DMIM TFSI with Pb-PbF_2 electrodes

The cycling performance of 0.3 m TMAF-DMIM TFSI was assessed by assembling Pb-PbF_2 symmetric cells, and maintaining the same conditions used in the cycling of the diluted electrolyte in Chapter 4. The electrodes used had 48 wt% Pb, 48 wt% PbF_2, 3 wt%

carbon nanofibers and 1 wt% PTFE. Their thickness was 18 μm, this extremely low value was selected to maximise the surface area and the percentage of active material exposed to the electrolyte. This decision was a consequence of the higher viscosity of this electrolyte which prevents it from penetrating across the thickness of the electrode (due to the low porosity). Since the cells were assembled in a 50% state of charge, the maximum capacity accessible on the 1st discharge is half the theoretical capacity (109 mAh g^{-1}). Starting from the 1st charge, the maximum achievable capacity corresponds to the theoretical capacity of PbF_2 (218 mAh g^{-1}).

The cycling performance of Pb-PbF_2 electrodes with the ionic liquid-based electrolyte demonstrated good capacity retention, despite theoretical capacity was never achieved. On the 1st charge only ~40 out of the 109 mAh g^{-1} was accessed (Fig. 5.13-a), suggesting that only ~35% of Pb converted to PbF_2. On the 1st discharge, the capacity reached 140 mAh g^{-1} out of the theoretical 218 mAh g^{-1}, indicating that a higher proportion of the active material (~60%) underwent the conversion reaction (Fig. 5.13-a). From the 1st discharge until the 7th cycle the capacity increased until reaching a maximum of 158 mAh g^{-1} (Fig. 5.13-a). This increase in capacity during the first 7 cycles may be caused by improved wetting during cycling, in which volume changes during the conversion reaction expose fresh active material into contact with the electrolyte. After the 7th cycle the cell exhibits good cycling capability for over 30 cycles, with a flat plateau at ~55 mV on charge and -40 mV on discharge (Fig. 5.13-b). The highest capacity of 158 mAh g^{-1} is obtained on the 7th cycle (Fig. 5.13-a,b,c). The capacity then fades over the following cycles until reaching 101 mAh g^{-1} at the 30th, which corresponds to a capacity retention of 64.4% (Fig. 5.13-b,c). Interestingly, the coulombic efficiency decreases between the 7th and 12th cycle, reaching 97.9%, and then increases back to 99.2% on the 25th cycle (Fig. 5.13-b,c),

indicating a slower capacity fading. More importantly, the coulombic efficiency never exceeded 100%, indicating that a lower degree of parasitic reactions compared to the diluted electrolyte (Chapter 4) occurred with 0.3 m TMAF-DMIM TFSI.

The lower-than-theoretical capacity achieved during cycling suggests an incomplete conversion of the active material, as demonstrated by the XRD in Fig. 5.13-d. The spectra for the charged and discharged electrodes after the 50th cycle show the presence of Pb and PbF_2, respectively. However, compared to the pristine electrodes, the lower intensity of the Pb peaks in the charged state, and of the PbF_2 peaks in the discharged state, confirm the occurrence of the conversion reaction during cycling. As with the diluted electrolyte (Chapter 4), β-PbF_2 converts to the α-phase during cycling, suggesting that the formation of the orthorhombic structure is more favourable, even with this electrolyte.

Despite not achieving the theoretical capacity, the capacity retention of the Pb-PbF_2 electrodes in 0.3 m TMAF-DMIM TFSI is superior to what has been reported in the literature with anion acceptors-based electrolytes.[24,29,44,68] The maximum capacity achieved with 0.3 m TMAF-DMIM TFSI is lower than the values achieved with the diluted electrolyte in Chapter 4. This can be explained by the low porosity of the electrodes, and the higher viscosity of this electrolyte (compared to TMAF-MeOH-PN), which prevents it from penetrating across the entire thickness of the electrodes. Despite not achieving full conversion, Pb-PbF_2 electrodes exhibit good cycling capability, with a constant overpotential, and good capacity retention in 0.3 m TMAF-DMIM TFSI. This further proves the suitability of these electrodes as counter-reference electrodes for cycling FIB coin cells.

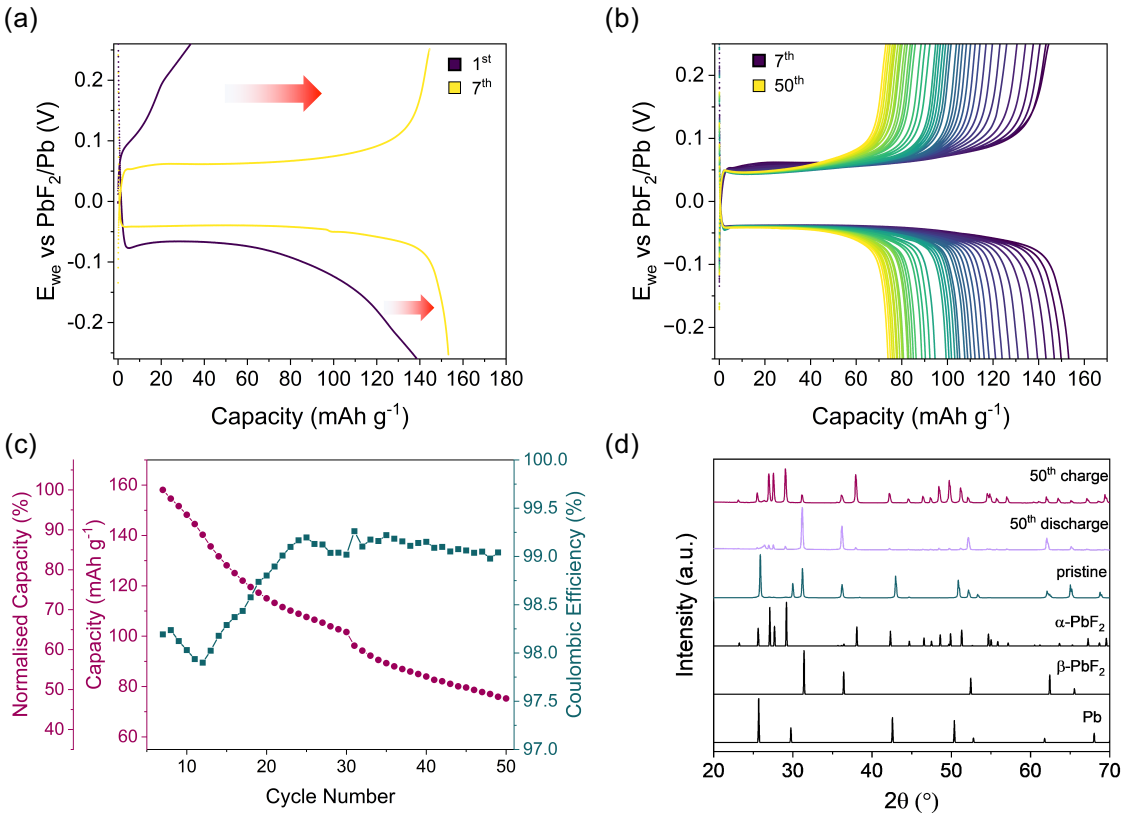


Figure 5.13: Cycling performance of Pb-PbF_2 electrodes in 0.3 m TMAF-DMIM TFSI. **(a)** GCPL plot showing the capacity increasing from the 1st to the 7th cycle of a Pb-PbF_2 symmetric cell at a C/20 rate (10.9 mA $g^{-1}_{PbF_2}$). **(b)** GCPL plot of the 7th to 50th cycles, showing fading in capacity. **(c)** Capacity, normalised capacity and coulombic efficiency as a function of cycle number for the Pb-PbF_2 symmetric cell. The capacity is normalised to the highest capacity reached (158 mAh g^{-1} on the 7th discharge). **(d)** XRD demonstrating the conversion between Pb and PbF_2 at the 50th cycle. The lack of full conversion is demonstrated by the presence of PbF_2 peaks in the discharged state and Pb peaks in the charged state.

5.2.6 Purification of DMIM TFSI

Although F-ions diffuse slightly faster than HF_2^- ions, the presence of HF_2^- in the electrolyte could cast doubt on whether F^- or HF_2^- is the main charge carrier during cycling. As previously explained the formation of HF_2^- can be traced to unknown impurities in the ionic liquid. Therefore, to assess whether the cycling performance or transport properties change in the absence of HF_2^-, the ionic liquid must be purified to remove the impurities.

The formation of HF_2 is likely caused by the presence of acidic protons in the impurities of the ionic liquid, as these protons can be easily extracted by F-ions. ^{1}H NMR confirmed this hypothesis, as two of the several impurities peaks lay at the chemical shifts (8.5 and 9.7 ppm) where acidic protons appear in proton NMR (deshielded region) (solid line in Fig. 5.14-a). Furthermore, once TMAF was added to DMIM TFSI the peak at 9.7 ppm disappeared (dashed line in Fig. 5.14-a), suggesting the occurrence of a reaction with F-ions that consumed the proton. It was not possible to establish whether the proton at 8.5 ppm was depleted as well since it overlapped with the peak of the 2nd hydrogen of the imidazolium ring.

It would be extremely complicated to determine what exactly these impurities are, given that DMIM TFSI was not synthesised in-house. However, by looking into the synthesis procedure of DMIM TFSI, it was possible to infer the likely presence of one such impurity featuring an acidic proton. Methyl sulphate is used as an alkylating agent to add the second methyl group to the imidazolium ring. Methyl sulphate impurities in their acidic form (methyl hydrogen sulphate) could therefore be present in the final ionic liquid and react with F-ions to form HF_2^- (Fig. 5.14-b). The manufacturer confirmed the plausibility of methyl hydrogen sulphate impurities being present in the ionic liquid (personal communication). Unfortunately, this theory could not be confirmed since the peaks of methyl sulphate overlap with those of DMIM TFSI. Regardless, determining the specific type of the acidic impurities was not crucial, given that the same strategy can be used to remove any acidic protons.

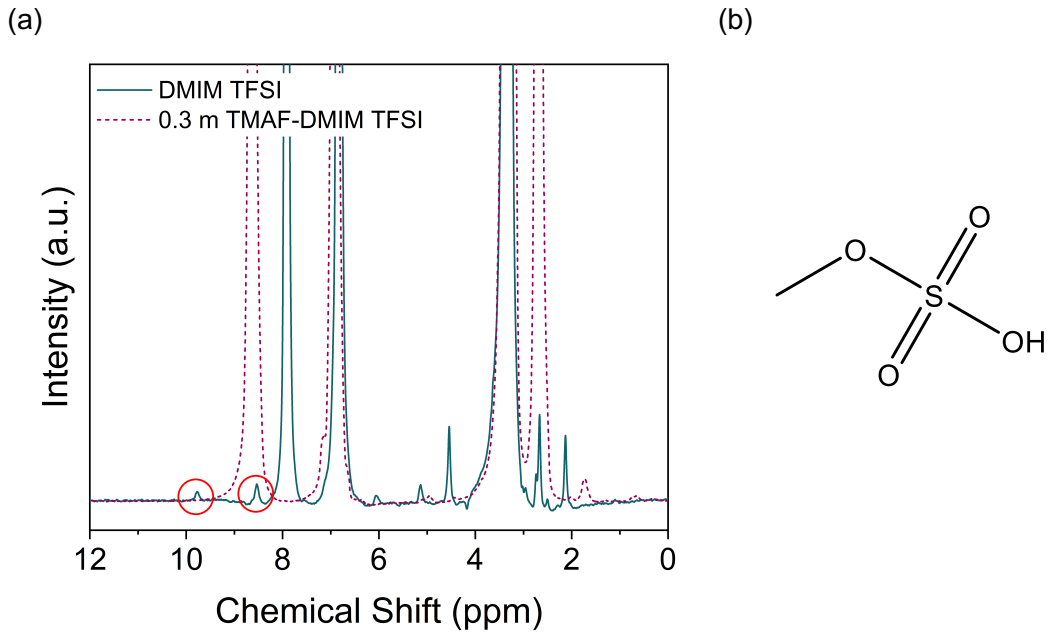


Figure 5.14: Acidic impurities in DMIM TFSI. **(a)** ^{1}H NMR of DMIM TFSI and 0.3 m TMAF-DMIM TFSI. DMIM TFSI contains several impurities, some of which possess protons with an NMR shift at high frequencies (acidic protons, circled in red). In 0.3 m TMAF-DMIM TFSI the impurity peak at the highest frequency disappears. **(b)** Chemical structure of methyl hydrogen sulphate (acidic) which may be present as an impurity in DMIM TFSI.

A washing procedure was used to try to eliminate the acidic impurity. DMIM TFSI was washed with a base and the amount of HF_2^- formed in 0.3 m TMAF-(washed)DMIM TFSI was compared to the initial HF_2^- content. An aqueous solution of Na_2CO_3 was mixed and vigorously stirred with the ionic liquid to force the two immiscible liquids to make contact with each other and neutralise any acidic impurity (details of the different washing procedures trialled are in Chapter 2). Following the washing, the HF_2^- concentration in 0.3 m TMAF-(washed)DMIM TFSI more than halved from 5.5 x 10^{-3} to 1.9 x 10^{-3} mol kg^{-1} (Fig. 5.15). This drastic reduction is conclusive proof that an acidic impurity, possibly methyl hydrogen sulphate, was the cause of the observed HF_2^- in the electrolyte.

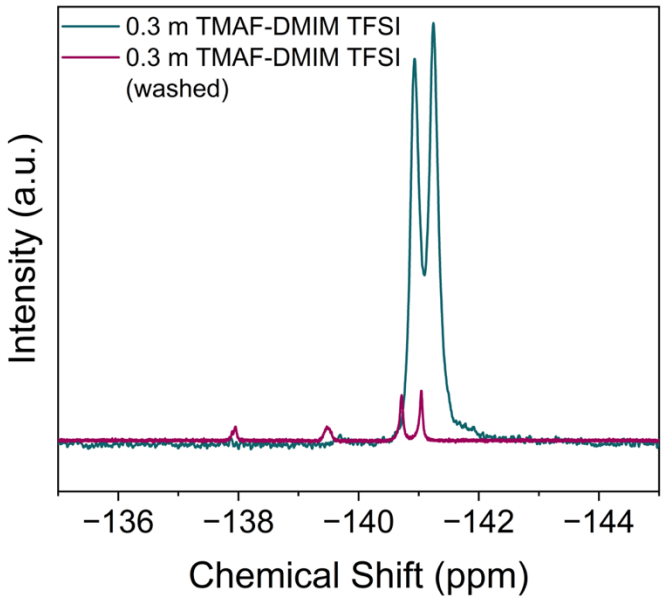


Figure 5.15: Decrease in HF_2^- following the washing of DMIM TFSI with a base. The ^{19}F NMR spectra of 0.3 m TMAF-DMIM TFSI before and after washing shows a significant decrease in peak intensity, indicating a lower HF_2^- content.

Although the washing procedure managed to reduce the impurity content and hence decrease the concentration of HF_2^- in the electrolyte, it failed to eliminate it. This is not surprising given that ionic liquids are notoriously difficult to purify. A different strategy was therefore chosen to produce a HF_2^- free TMAF-DMIM TFSI electrolyte. Rather than purifying commercial DMIM TFSI, the ionic liquid will be synthesised to achieve even higher purity and be certain of what impurities might be present. The synthesis and further purification will be carried out by collaborators at the Queen's University Ionic Liquid Laboratories (QUILL) in Belfast (UK) who are experts in the synthesis of ionic liquids.

5.3 Conclusion and Future Work

In this chapter, by using TMAF-DMIM TFSI, the first chemically stable liquid electrolyte for FIBs (without HF or HF_2^- formation) was reported. The electrolyte also displayed good transport properties at the 0.3 m concentration, and a wide electrochemical

stability window, which allows cycling of the most promising cathode materials. Unfortunately, the problem of low reductive stability was not solved with this electrolyte, meaning that an electrolyte that can function with the most promising anode materials is still missing. Lastly, by using TMAF-DMIM TFSI, good cycling of Pb-PbF_2 electrodes was achieved, with no evidence of electrolyte degradation.

The properties of TMAF-DMIM TFSI reported here are tainted by the presence of HF_2^-arising from acidic impurities contained in the ionic liquid. Further work is required to characterise the performance of TMAF-DMIM TFSI free from the acidic impurity and consequently HF_2^-, to assess whether the transport properties and the cycling performance are affected by its absence.

Furthermore, additional work is required to investigate the underlying cause for the peculiar trend observed in the diffusion coefficient of F-ions (no diffusion at the two lowest concentrations). Neutron scattering could be used to investigate how the solvation structure changes with increasing TMAF concentration, and how this change might relate to the trend in the diffusion coefficient.

The use of DMIM TFSI, as demonstrated here, has paved the way for the design of novel liquid electrolytes for FIBs by highlighting a crucial factor for success: solvents should contain a proton with sufficient acidity to enable fluoride ion solvation, while avoiding the excessive acidity that results in proton extraction and HF formation. Future work should focus on quantifying this optimal acidity of protons, to enable the search for other suitable solvents capable of solvating F-ions while being chemically stable.

Chapter 6

Conclusion and Future Work

Table of Contents

6.1 Conclusion 137

6.2 Future Work 139

6.1 Conclusion

Conversion-type fluoride-ion batteries with liquid electrolytes are a promising next-generation battery technology thanks to their high energy densities and lack of critical battery materials (e.g., Li and Co). Currently, liquid electrolyte FIBs have inferior cycling performance compared to all-solid-state FIBs because of the lack of a suitable liquid electrolyte and a reliable testing set-up. The challenge in developing liquid electrolytes lays in the limited solubility of fluoride salts and the reactivity of F-ions, which restrict the choice of possible solvents. Regarding the testing set-up, the use of flooded cells as the standard for liquid electrolyte FIBs has led to inaccurate cycling results. In this work, a strategy to solve each of these problems has been demonstrated.

In Chapter 3, the use of coin cells, which provide more realistic results compared to flooded cells, was enabled by addressing the problems that have prevented their use in FIBs to this date. First, a reliable and chemically stable counter-reference electrode was presented. Careful design of the counter-reference electrode's microstructure allows to achieve reversible cycling with a stable overpotential. Additionally, the use of PTFE as the binder for the counter-reference electrode prevents chemical degradation caused by the electrolyte during cycling. Moreover, hydrophilic PTFE proved to be a good separator due to its excellent wettability and electrochemical stability. The combination of these components enables the use of coin cells and allows for the accurate testing of the liquid electrolytes presented in the following chapters.

In Chapter 4, a novel strategy for the design of liquid electrolytes for FIBs was introduced. The use of a diluent for highly concentrated electrolytes addresses the drawbacks of high viscosity and high amounts of salt required while retaining the advantage of the highly concentrated electrolyte. This concept was demonstrated by using a highly concentrated solution of 10 m tetramethylammonium fluoride in methanol which was diluted with propionitrile. By adding propionitrile the diffusion coefficient of F-ions increases by an order of magnitude, the wider electrochemical stability window of 10 m TMAF in MeOH is retained and the amount of TMAF required is significantly decreased making the electrolyte practical. Additionally, the diluted electrolyte exhibits improved cycling performance of Pb-PbF_2 electrodes with an almost 20% increase in capacity retention. This cycling performance is the best for Pb-PbF_2 ever achieved in FIBs. TMAF-MeOH-PN also allowed to achieve the best capacity retention for BiF_3 electrodes. The cycling performance of these electrodes proves the validity of the coin cell set-up and the diluent strategy.

In Chapter 5, a different strategy was shown for the development of liquid electrolytes for FIBs: the use of ionic liquids without β-hydrogens. Thanks to this, the imidazolium-based ionic liquid electrolyte exhibits the best chemical stability (no HF or HF_2^- generation) ever reported for a liquid electrolyte for FIBs. Additionally, the electrolyte exhibits good ionic conductivity and a wide electrochemical stability window. Finally, this electrolyte showcases the importance of having a hydrogen in the solvent that is acidic enough to enable F-ion solvation, while is not too acidic to prevent proton extraction and HF formation.

6.2 Future Work

The aim of this thesis has been to advance the progress of liquid electrolyte FIBs by demonstrating novel strategies in cell and electrolyte design. This work also opens many promising avenues to progress the field further.

Highly concentrated electrolytes with the addition of a diluent can be an effective strategy to achieve a liquid electrolyte that satisfies all the requirements for successful performance. In this work good transport properties and great cycling performance have been achieved using this strategy, however the electrochemical stability window is still too narrow to achieve high energy densities. Expanding the electrochemical stability window is of paramount importance because up until now liquid electrolytes (including the ones reported in this work) are stable at high potentials, but not at the low redox potentials of the most appealing anodes. To accomplish this, a protic solvent that dissolves the fluoride salt to higher concentrations than that achieved with TMAF in MeOH should be used. Additionally, a diluent that is still miscible with the protic solvent but has lower polarity and dielectric constant than propionitrile would also improve performance. Such a diluent would have a reduced interaction with F-ions, leading to a lower degree of disruption of the solvation shell of the protic solvent molecules around F-ions. A lower disruption should translate into an even wider electrochemical stability window.

To enhance cycling performance beyond what is attainable with the diluted electrolyte discussed in Chapter 4, it is imperative to ensure that no active material dissolution occurs. With TMAF-MeOH-PN, dissolution seems to occur to some small extent with Pb-PbF_2 electrodes, whilst it is catastrophically high for the CuF_2 electrodes.

For the Pb-PbF_2 electrodes, it would be important to establish whether the issues observed after repeated cycling (coulombic efficiency exceeding 100%) are a result of

active material dissolution. To determine if this is the case, it would be necessary to establish whether the <0.01 ppm dissolution of Pb and PbF_2 recorded with ICP is enough to account for such a high coulombic efficiency, or whether the cause of this issue is the formation of more soluble intermediates during cycling. The latter might be more plausible given that <0.01 ppm dissolution is extremely low. To determine whether any soluble intermediates form during cycling, Pb-PbF_2 dissolution in the diluted electrolyte should be measured at different states of charge (e.g., after 50% discharge, full discharge, 50% recharged, fully charged). These datapoints would indicate whether a particular event triggers the dissolution, or if instead the concentration of Pb ions in the electrolyte increases gradually with cycle number. Being aware of the existence of such soluble intermediates would be useful during the testing of other liquid electrolytes with Pb-PbF_2 electrodes, so that the occurrence of dissolution is not attributed entirely to a fault of the electrolyte.

To prevent dissolution of CuF_2 into the electrolyte and enable cycling, a different pair of solvents should be used, as both methanol and propionitrile likely dissolve CuF_2. Selecting solvents that do not dissolve CuF_2 is not trivial given the possibility of forming Cu(I) intermediates during cycling that are very soluble (as observed in LIBs). Nonetheless, being able to cycle CuF_2 would provide a great advancement in the field.

The imidazolium-based electrolyte introduced in Chapter 5 represents another encouraging avenue for developing liquid electrolytes for FIBs. A crucial test to carry out involves quantifying the acidity of the second proton on the imidazolium ring, which enables F-ion solvation. Following this, a screening process can be conducted to identify solvents featuring one or more protons with similar acidity. This would allow to create a pool of potential solvents that allow the solvation of F-ions while preventing HF formation.

Having such a list of suitable solvents available would very likely allow to design the ideal electrolyte capable of satisfying all the requirements.

The novel design strategies reported in this work have advanced the performance of liquid electrolyte FIBs. However, this performance is still far from what is required for commercial applications, and much work remains to be done. The success of FIBs will be dependent on the discovery of a suitable liquid electrolyte. Hopefully the work and results presented here will aid such a discovery.

References

List of References

1. IPCC. Framing and Context. in *Global Warming of 1.5°C* 49–92 (Cambridge University Press, 2022). doi:10.1017/9781009157940.003.

2. Clark, M. A. *et al.* Global food system emissions could preclude achieving the 1.5° and 2°C climate change targets. *Science (1979)* **370**, 705–708 (2020).

3. Bibra, E. M. *et al. Global EV Outlook 2022 Securing supplies for an electric future*. www.iea.org/t&c/ (2022).

4. IEA. *Global EV Outlook 2023: Catching up with climate ambitions*. www.iea.org (2023).

5. Benchmark Mineral Intelligence. *Lithium Forecasts*. (2022).

6. Xiao, A. W., Galatolo, G. & Pasta, M. The case for fluoride-ion batteries. *Joule* **5**, 2823–2844 (2021).

7. Liu, T. *et al.* Insight into anion storage batteries: Materials, properties and challenges. *Energy Storage Mater* **42**, 42–67 (2021).

8. Karkera, G., Reddy, M. A. & Fichtner, M. Recent developments and future perspectives of anionic batteries. *J Power Sources* **481**, (2021).

9. Chen, Y., Juang, Y. & Chu, S. A Solid-State Galvanic Cell with Fluoride-Conducting Electrolytes. *J. Electrochem. Soc* **123**, 1772 (1976).

10. Danto, Y., Poujade, G., Pistré, J. D., Lucat, C. & Salardenne, J. A Pb|PbF2|BiF3|Bi thin solid film reversible galvanic cell. *Thin Solid Films* **55**, 347–354 (1978).

11. Chun, J. *et al.* Thin-Film Galvanic Cell Pb/PbF2/PbF2, CuF2/Cu. *Journal of Electrochemical Society* **123**, (1976).

12. Schoonman, J. & Wolfert, A. Solid-state galvanic cells with fast fluoride conducting electrolytes. *Solid State Ion* **3**, 373–379 (1981).

13. Anji Reddy, M. & Fichtner, M. Batteries based on fluoride shuttle. *J Mater Chem* **21**, 17059–17062 (2011).

14. McRae, M. *Mineral commodity summary - Fluorspar*. (2023).

15. Jaskula, B. *Mineral commodity survey - Lithium*. (2023).

16. Wang, J. & Ma, C. Superior room-temperature cycling stability of fluoride-ion batteries enabled by solid electrolytes synthesized by the solid-state reaction. *Sci China Mater* **65**, 3025–3032 (2022).

17. Wang, Y. *et al.* Properties of Composite Electrodes for All-solid-state Fluoride-ion Secondary Batteries Processed by High-pressure Torsion. *Electrochemistry* **91**, (2023).

18. Marshall, J. E. *et al.* On the solubility and stability of polyvinylidene fluoride. *Polymers (Basel)* **13**, (2021).

19. Kobayashi, S. *et al.* Nanoscale Defluorination Mechanism and Solid Electrolyte Interphase of a MgF2 Anode in Fluoride-Shuttle Batteries. *ACS Appl Energy Mater* **4**, 996–1003 (2021).

20. Yamamoto, T., Matsumoto, K., Hagiwara, R. & Nohira, T. Room-Temperature Fluoride Shuttle Batteries Based on a Fluorohydrogenate Ionic Liquid Electrolyte. *ACS Appl Energy Mater* **2**, 6153–6157 (2019).

21. Yaokawa, R., Shiga, T., Moribe, S. & Mukai, K. Evidence of a reversible redox reaction in a liquid-electrolyte-type fluoride-ion battery. *RSC Adv* **12**, 31786–31791 (2022).

22. Gschwind, F. *et al.* Fluoride ion batteries: Theoretical performance, safety, toxicity, and a combinatorial screening of new electrodes. *J Fluor Chem* **182**, 76–90 (2016).

23. Celik Kucuk, A., Minato, T., Yamanaka, T. & Abe, T. Effects of LiBOB on salt solubility and BiF3 electrode electrochemical properties in fluoride shuttle batteries. *J Mater Chem A Mater* **7**, 8559–8567 (2019).

24. Nowroozi, M. A. & Clemens, O. Insights on the Behavior of Conversion-Based Anode Materials for Fluoride Ion Batteries by Testing against an Intercalation-Based Reference Cathode. *ACS Applied Energy Materials* **1**, 6626–6637 (2018).

25. Nowroozi, M. A., Wissel, K., Rohrer, J., Munnangi, A. R. & Clemens, O. LaSrMnO4: Reversible Electrochemical Intercalation of Fluoride Ions in the Context of Fluoride Ion Batteries. *Chemistry of Materials* **29**, (2017).

26. Wissel, K. *et al.* Electrochemical Reduction and Oxidation of Ruddlesden-Popper-Type La2NiO3F2within Fluoride-Ion Batteries. *Chemistry of Materials* **33**, 499–512 (2021).

27. Konishi, H., Minato, T., Abe, T. & Ogumi, Z. Reactivity of the anion acceptor in electrolyte: An important factor in achieving high electrochemical performance of a lead (II) fluoride electrode in a fluoride shuttle battery. *Journal of Electroanalytical Chemistry* **871**, (2020).

28. Konishi, H., Minato, T., Abe, T. & Ogumi, Z. Charge and Discharge Reactions of a Lead Fluoride Electrode in a Liquid-Based Electrolyte for Fluoride Shuttle

Batteries:-The Role of Triphenylborane as an Anion Acceptor. *Chemistry Select* **4**, 5984–5987 (2019).

29. Konishi, H., Minato, T., Abe, T. & Ogumi, Z. Charge and Discharge Reactions of a Lead Fluoride Electrode in a Liquid-Based Electrolyte for Fluoride Shuttle Batteries: The Role of Triphenylborane as an Anion Acceptor. *ChemistrySelect* **4**, 5984–5987 (2019).

30. He, M., Guo, R., Hobold, G. M., Gao, H. & Gallant, B. M. The intrinsic behavior of lithium fluoride in solid electrolyte interphases on lithium. *PNAS* **117**, 73–79 (2020).

31. Wang, A., Kadam, S., Li, H., Shi, S. & Qi, Y. Review on modeling of the anode solid electrolyte interphase (SEI) for lithium-ion batteries. *NPJ Comput Mater* **4**, (2018).

32. Nowroozi, M. A. *et al.* Fluoride ion batteries - past, present, and future. *J Mater Chem A Mater* **9**, 5980–6012 (2021).

33. Liu, L. *et al.* SnF2-based fluoride ion electrolytes MSnF4(M=Ba, Pb) for the application of room-temperature solid-state fluoride ion batteries. *J Alloys Compd* **819**, (2020).

34. Mohammad, I., Witter, R., Fichtner, M. & Reddy, A. M. Introducing Interlayer Electrolytes Toward Room-Temperature High-Potential Solid-State Rechargeable Fluoride Ion Batteries. *ACS Appl Energy Mater* **2**, 1553–1562 (2019).

35. Wang, J. *et al.* A Fluoride-Ion-Conducting Solid Electrolyte with Both High Conductivity and Excellent Electrochemical Stability. *Small* **18**, (2022).

36. Okazaki, K.-I., Uchimoto, Y., Abe, T. & Ogumi, Z. Charge−Discharge Behavior of Bismuth in a Liquid Electrolyte for Rechargeable Batteries Based on a Fluoride Shuttle. *ACS Energy Lett* **2**, 1460–1464 (2017).

37. Yamamoto, T. Next-generation Rechargeable Batteries Utilizing Ionic Liquids and Various Charge Carriers. *Electrochemistry* **90**, (2022).

38. Yamamoto, T., Matsumoto, K., Hagiwara, R. & Nohira, T. Charge–Discharge Performance of Copper Metal Positive Electrodes in Fluorohydrogenate Ionic Liquids for Fluoride-Shuttle Batteries. *J Electrochem Soc* **168**, 040530 (2021).

39. Celik Kucuk, A. & Abe, T. Borolan-2-yl involving anion acceptors for organic liquid electrolyte-based fluoride shuttle batteries. *J Fluor Chem* **240**, (2020).

40. Konishi, H., Minato, T., Abe, T. & Ogumi, Z. Electrochemical Performance of a Bismuth Fluoride Electrode in a Reserve-Type Fluoride Shuttle Battery. *J Electrochem Soc* **164**, A3702–A3708 (2017).

41. Konishi, H., Minato, T., Abe, T. & Ogumi, Z. Improvement of cycling performance in bismuth fluoride electrodes by controlling electrolyte composition in fluoride shuttle batteries. *J Appl Electrochem* **48**, 1205–1211 (2018).

42. Konishi, H., Minato, T., Abe, T. & Ogumi, Z. Electrochemical properties of lead fluoride electrode in fluoride shuttle battery. *Journal of Electroanalytical Chemistry* **826**, 60–64 (2018).

43. Konishi, H., Minato, T., Abe, T. & Ogumi, Z. Reversible Electrochemical Reaction of a Fluoride Shuttle Battery with a Bismuth(III) Fluoride Electrode and Electrolyte Containing Triphenylboroxine as an Anion Acceptor. *ChemistrySelect* **5**, 6237–6241 (2020).

44. Konishi, H., Minato, T., Abe, T. & Ogumi, Z. Electrochemical performance of a lead fluoride electrode mixed with carbon in an electrolyte containing triphenylboroxine as an anion acceptor for fluoride shuttle batteries. *Mater Chem Phys* **226**, 1–5 (2019).

45. Celik Kucuk, A., Yamanaka, T., Yokoyama, Y. & Abe, T. Low-Cost Fluoride Source for Organic Liquid Electrolyte-Based Fluoride Shuttle Battery. *J Electrochem Soc* **168**, 010501 (2021).

46. Kawasaki, M. *et al.* Lactone-Based Liquid Electrolytes for Fluoride Shuttle Batteries. *J Electrochem Soc* **168**, 010529 (2021).

47. Davis, V. K. *et al.* Room-temperature cycling of metal fluoride electrodes: Liquid electrolytes for high-energy fluoride ion cells. *Science (1979)* **362**, 1144–1148 (2018).

48. Hore, P. *Nuclear magnetic resonance spectroscopy*. (Oxford University Press, 2015).

49. Momot, K. I. & Kuchel, P. W. PFG NMR diffusion experiments for complex systems. *Concepts Magn Reson Part A Bridg Educ Res* **28**, 249–269 (2006).

50. Berne, B. J. & Pecora, R. *Dynamic Light Scattering: With Applications to Chemistry, Biology, and Physics*. (Courier Corporation, 2000).

51. Warren, B. E. *X-Ray Diffraction*. (Courier Corporation, 1990).

52. Smith, B. C. *Fundamentals of Fourier Transform Infrared Spectroscopy*. (CRC Press, 2011).

53. Thompson, M. & Walsh, N. J. *Handbook of Inductively Coupled Plasma Spectrometry*. (Springer US, 2012).

54. Vernon-Parry, K. D. Scanning Electron Microscopy: an introduction. *III-Vs Review* **13**, (2000).

55. Giannuzzi, L. A. *Introduction to Focused Ion Beams: Instrumentation, Theory, Techniques and Practice*. (Springer Science & Business Media, 2006).

56. Palagonia, M. S., Erinmwingbovo, C., Brogioli, D. & La Mantia, F. Comparison between cyclic voltammetry and differential charge plots from galvanostatic cycling. *Journal of Electroanalytical Chemistry* **847**, (2019).

57. Lazanas, A. C. & Prodromidis, M. I. Electrochemical Impedance Spectroscopy─A Tutorial. *ACS Measurement Science Au* **3**, 162–193 (2023).

58. Parker, V. D. Linear Sweep and Cyclic Voltammetry. *Comprehensive Chemical Kinetics* **26**, 145–202 (1986).

59. Soper, A. K. & Phillips, M. G. A new determination of the structure of water at 25°C. *Chem Phys* **107**, 47 (1986).

60. Youngs, T. G. A. Aten - An application for the creation, editing, and visualization of coordinates for glasses, liquids, crystals, and molecules. *J Comput Chem* **31**, 639–648 (2010).

61. Jorgensen, W. L., Maxwell, D. S. & Tirado-Rives, J. Development and Testing of the OPLS All-Atom Force Field on Conformational Energetics and Properties of Organic Liquids. *J Am Chem Soc* **118**, 11225–11236 (1996).

62. Jorgensen, W. L., Ulmschneider, J. P. & Tirado-Rives, J. Free energies of hydration from a generalized born model and an all-atom force field. *Journal of Physical Chemistry B* **108**, 16264–16270 (2004).

63. Price, M. L. P., Ostrovsky, D. & Jorgensen, W. L. Gas-phase and liquid-state properties of esters, nitriles, and nitro compounds with the OPLS-AA force field. *J Comput Chem* **22**, 1340–1352 (2001).

64. Chandrasekhar, J., Spellmeyer, D. C. & Jorgensen, W. L. Energy Component Analysis for Dilute Aqueous Solutions of Li+, Na+, F-, and Cl- Ions. *Journal of American Chemistry Society* **106**, 903–910 (1984).

65. Hanwell, M. D. *et al.* Avogadro: an advanced semantic chemical editor, visualization, and analysis platform. *J Cheminform* **4**, 17 (2012).

66. Halgren, T. A. Merck molecular force field. I. Basis, form, scope, parameterization, and performance of MMFF94. *J Comput Chem* **17**, 490–519 (1996).

67. Portella, K. F. *et al.* Characterization of α ↔ β PbF 2 phase transition by several techniques. *J Mater Sci* **3 5**, 3263–3268 (2000).

68. Konishi, H., Minato, T., Abe, T. & Ogumi, Z. Reactivity of the anion acceptor in electrolyte: An important factor in achieving high electrochemical performance of a

lead (II) fluoride electrode in a fluoride shuttle battery. *Journal of Electroanalytical Chemistry* **871**, (2020).

69. Wang, Y., Herricks, T. & Xia, Y. Single crystalline nanowires of lead can be synthesized through thermal decomposition of lead acetate in ethylene glycol. *Nano Lett* **3**, 1163–1166 (2003).

70. Marshall, J. E. *et al.* On the Solubility and Stability of Polyvinylidene Fluoride. *Polymers (Basel)* **13**, (2021).

71. Huang, W. *et al.* Overcoming the fundamental challenge of PVDF binder use with silicon anodes with a super-molecular nano-layer. *J Mater Chem A Mater* **9**, 1541–1551 (2021).

72. Zhong, X., Zhao, X., Qian, Y. & Zou, Y. Polyethylene plastic production process. *Insight - Material Science* **1**, 1 (2018).

73. Huseby, T. W. & Bair, H. E. Dissolution of Polyethylene Single Crystals in Xylene and Octadecane. *Journal of Applied Physiscs* **39**, 4969–4973 (1968).

74. Heine, J., Rodehorst, U., Badillo, J. P., Winter, M. & Bieker, P. Chemical stability investigations of polyisobutylene as new binder for application in lithium air-batteries. *Electrochim Acta* **155**, 110–115 (2015).

75. Batzer, M., Voges, K., Wang, W., Michalowski, P. & Kwade, A. Systematic evaluation of materials and recipe for scalable processing of sulfide-based solid-state batteries. *Mater Today Commun* **30**, (2022).

76. Teng, H. Overview of the development of the fluoropolymer industry. *Applied Sciences* **2**, 496–512 (2012).

77. Wang, C. *et al.* Solvent-Free Approach for Interweaving Freestanding and Ultrathin Inorganic Solid Electrolyte Membranes. *ACS Energy Lett* **7**, 410–416 (2022).

78. Yamamoto, T., Matsumoto, K., Hagiwara, R. & Nohira, T. Charge–Discharge Performance of Copper Metal Positive Electrodes in Fluorohydrogenate Ionic Liquids for Fluoride-Shuttle Batteries. *J Electrochem Soc* **168**, 040530 (2021).

79. Kawauchi, S., Nakamoto, H., Takekawa, R., Kobayashi, T. & Abe, T. Electrolytes for Room-Temperature Rechargeable Fluoride Shuttle Batteries. *ACS Appl Energy Mater* **5**, 2096–2103 (2022).

80. Lu, Y. *et al.* Dry electrode technology, the rising star in solid-state battery industrialization. *Matter* **5**, 876–898 (2022).

81. Choi, J. & Kim, P. J. A roadmap of battery separator development: Past and future. *Curr Opin Electrochem* **31**, (2022).

82. Qiao, Q., He, H. & Yu, J. Evolution of HF etching rate of borosilicate glass by friction-induced damages. *Appl Surf Sci* **512**, (2020).

83. Francis, C. F. J., Kyratzis, I. L. & Best, A. S. Lithium-Ion Battery Separators for Ionic-Liquid Electrolytes: A Review. *Advanced Materials* **32**, (2020).

84. Clark, J. H. Fluoride Ion as a Base in Organic Synthesis. *Chem. Rev* **80**, 429–452 (1980).

85. Alshangiti, O. *et al.* Solvent-in-Salt Electrolytes for Fluoride Ion Batteries. *ACS Energy Lett* **12**, 2668–2673 (2023).

86. Ren, F. *et al.* Solvent–Diluent Interaction-Mediated Solvation Structure of Localized High-Concentration Electrolytes. *ACS Appl Mater Interfaces* **14**, 4211–4219 (2022).

87. Wang, H. *et al.* Liquid electrolyte: The nexus of practical lithium metal batteries. *Joule* vol. 6 588–616 Preprint at https://doi.org/10.1016/j.joule.2021.12.018 (2022).

88. Doi, T., Hashinokuchi, M. & Inaba, M. Solvation-controlled ester-based concentrated electrolyte solutions for high-voltage lithium-ion batteries. *Current Opinion in Electrochemistry* vol. 9 49–55 Preprint at https://doi.org/10.1016/j.coelec.2018.03.032 (2018).

89. Perez Beltran, S., Cao, X., Zhang, J. G., El-Khoury, P. Z. & Balbuena, P. B. Influence of diluent concentration in localized high concentration electrolytes: Elucidation of hidden diluent-Li+interactions and Li+transport mechanism. *J Mater Chem A Mater* **9**, 17459–17473 (2021).

90. Hawk, M. K. *et al.* Tetramethylammonium Fluoride Tetrahydrate for SNAr Fluorination of 4-Chlorothiazoles at a Production Scale. *Org Process Res Dev* **25**, 1167–1175 (2021).

91. Ha, Y. *et al.* Effect of Water Concentration in LiPF6-Based Electrolytes on the Formation, Evolution, and Properties of the Solid Electrolyte Interphase on Si Anodes. *ACS Appl Mater Interfaces* **12**, 49563–49573 (2020).

92. Ma, L. *et al.* Fundamental Understanding and Material Challenges in Rechargeable Nonaqueous Li–O2 Batteries: Recent Progress and Perspective. *Advanced Energy Materials* vol. 8 Preprint at https://doi.org/10.1002/aenm.201800348 (2018).

93. Christe, K. O., Wilson, W. W., Wilson, R. D., Bau, R. & Feng, J. Syntheses, Properties, and Structures of Anhydrous Tetramethylammonium Fluoride and Its 1:1 Adduct with trans-3-Amino-2-butenenitrile. *J. Am. Chem. Soc* **112**, 7619–7625 (1990).

94. Kolomeitsev, A. A., Seifert, F. U. & Roschenthaler, G.-V. Simple preparation of difluorophosphoranes using anhydrous zinc and tetramethylammonium fuorides. *J Fluor Chem* **71**, 47–49 (1995).

95. Forero-Saboya, J., Hosseini-Bab-Anari, E., Abdelhamid, M. E., Moth-Poulsen, K. & Johansson, P. Water-in-bisalt electrolyte with record salt concentration and widened electrochemical stability window. *Journal of Physical Chemistry Letters* **10**, 4942–4946 (2019).

96. Nguyen, H. V. T., Faheem, A. Bin, Kwak, K. & Lee, K. K. Propionitrile as a single organic solvent for high voltage electric double-layer capacitors. *J Power Sources* **463**, 228134 (2020).

97. Wohlfarth, C. Viscosity of propionitrile. in *Viscosity of Pure Organic Liquids and Binary Liquid Mixtures* 67–67 (Springer Berlin Heidelberg, 2017). doi:10.1007/978-3-662-49218-5_59.

98. Davis, V. K. *et al.* Fluoride-ion solvation in non-aqueous electrolyte solutions. *Mater Chem Front* **3**, 2721–2727 (2019).

99. Simon, C. & Klein, M. L. Ab initio molecular dynamics simulation of a water-hydrogen fluoride equimolar mixture. *ChemPhysChem* **6**, 148–153 (2005).

100. Nilsson, V., Bernin, D., Brandell, D., Edström, K. & Johansson, P. Interactions and Transport in Highly Concentrated LiTFSI-based Electrolytes. *ChemPhysChem* **21**, 1166–1176 (2020).

101. Anion Coordination Characteristics of Ion-pair Complexes in Highly Concentrated Aqueous Lithium Bis(trifluoromethanesulfonyl)amide Electrolytes.

102. Dalessandro, E. V. & Pliego, J. R. Reactivity and stability of ion pairs, dimers and tetramers versus solvent polarity: SNAr fluorination of 2-bromobenzonitrile with tetramethylammonium fluoride. *Theor Chem Acc* **139**, (2020).

103. Dixit, S., Crain, J., Poon, W. C. K., Finney, J. L. & Soper, A. K. Molecular segregation observed in a concentrated alcohol–water solution. *Nature* **416**, (2002).

104. Dougan, L. *et al.* Methanol-water solutions: A bi-percolating liquid mixture. *Journal of Chemical Physics* **121**, 6456–6462 (2004).

105. Konishi, H. *et al.* Low-Cost Fluoride Source for Organic Liquid Electrolyte-Based Fluoride Shuttle Battery. *J Electrochem Soc* **168**, (2021).

106. Konishi, H., Kucuk, A. C., Minato, T., Abe, T. & Ogumi, Z. Improved electrochemical performances in a bismuth fluoride electrode prepared using a high

energy ball mill with carbon for fluoride shuttle batteries. *Journal of Electroanalytical Chemistry* **839**, 173–176 (2019).

107. Mohammad, I. & Witter, R. Testing Mg as an anode against BiF3 and SnF2 cathodes for room temperature rechargeable fluoride ion batteries. *Mater Lett* **244**, 159–162 (2019).

108. Konishi, H., Minato, T., Abe, T. & Ogumi, Z. Improvement of cycling performance in bismuth fluoride electrodes by controlling electrolyte composition in fluoride shuttle batteries. *J Appl Electrochem* **48**, 1205–1211 (2018).

109. Konishi, H., Minato, T., Abe, T. & Ogumi, Z. Influence of Electrolyte Composition on the Electrochemical Reaction Mechanism of Bismuth Fluoride Electrode in Fluoride Shuttle Battery. *Journal of Physical Chemistry C* **123**, 10246–10252 (2019).

110. Avraamides, J., Baird-Trotter, R. & Hoecker, W. Leaching of silver with copper(II) ions in aqueous acetonitrile solutions: solubility of salts and equilibrium constant measurements in sulphate media. *Hydrometallurgy* 351--362 (1986).

111. Krossing, I. *et al.* Why are ionic liquids liquid? A simple explanation based on lattice and solvation energies. *J Am Chem Soc* **128**, 13427–13434 (2006).

112. IoLiTec. *TDS IL-0198 DiMIM BTA*. https://iolitec.de/sites/iolitec.de/files/2017-09/TDS%20IL-0198%20DiMIM%20BTA.pdf (2013).

113. IoLiTec. *TDS IL-0241 BenzMIM BTA*. https://iolitec.de/sites/iolitec.de/files/2017-09/TDS%20IL-0241%20BenzMIM%20BTA.pdf (2011).

114. Sun, X. G. *et al.* Bicyclic imidazolium ionic liquids as potential electrolytes for rechargeable lithium ion batteries. *J Power Sources* **237**, 5–12 (2013).

115. De Vos, N., Maton, C. & Stevens, C. V. Electrochemical Stability of Ionic Liquids: General Influences and Degradation Mechanisms. *ChemElectroChem* **1**, 1258–1270 (2014).

116. Huang, H. *et al.* New Insights into the Stability of Anhydrous 2H-Imidazolium Fluoride and its High Dissolution Capability toward a Strongly Hydrogen-Bonded Compound. *J. Am. Chem. Soc* **142**, 10314–10318 (2020).

117. Han, H. J., Oh, J. H., L. Sessler, J. & Kim, S. K. Small triiminopyrrolic molecular cage with high affinity and selectivity for fluoride. *ChemComm* **55**, 10876–10879 (2019).

118. Schaumburg, K. & Deverell, C. Fluorine-19 Nuclear Magnetic Resonance Chemical Shift of Hydrofluoric Acid in H20 and D20 Solutions. *J Am Chem Soc* **90**, 2495–2499 (1968).

119. Hudlicky, M. Chemical Shifts of Fluorine in Hydrogen Fluoride and Fluoride Ion. *J Fluor Chem* **28**, 461–472 (1985).

120. Chen, C., Martin, J. S. & Fujiwara, F. Y. High Resolution Nuclear Magnetic Resonance Spectra of Bifluoride Ion and its Homologues. *Can J Chem* **3071**, 157 (1967).

121. Okazaki, K. I. *et al.* Examination of Morphological Changes of Active Materials for Solution-Based Rechargeable Fluoride Shuttle Batteries Using in Situ Electrochemical Atomic Force Microscopy Measurements. *Chemistry of Materials* **34**, 8280–8288 (2022).

122. Frömling, T., Kunze, M., Schönhoff, M., Sundermeyer, J. & Roling, B. Enhanced Lithium Transference Numbers in Ionic Liquid Electrolytes. *J Phys Chem B* **112**, 12985–12990 (2008).

123. Riggle, J. & von Wandruszka, R. 31P NMR peak width in humate-phosphate complexes. *Talanta* **73**, 953–958 (2007).